The Dissertation Committee for Kyounghwan Kim Certifies that this is the approved version of the following dissertation:

Electronic Properties and Device Applications of Rotationally Controlled van der Waals Heterostructures

Committee:

Emanuel Tutuc, Supervisor

Sanjay K. Banerjee

Allan H. MacDonald

Leonard F. Register

Seth Bank

Electronic Properties and Device Applications of Rotationally Controlled van der Waals Heterostructures

by

Kyounghwan Kim

Dissertation

Presented to the Faculty of the Graduate School of

The University of Texas at Austin

in Partial Fulfillment

of the Requirements

for the Degree of

Doctor of Philosophy

The University of Texas at Austin

December, 2018

Dedication

To my parents and wife

Acknowledgements

I would like to first express my special appreciation to my advisor Dr. Emanuel Tutuc, a great mentor in my life as a graduate student. I am sincerely thankful for his knowledge and passion in research, which pushed me to excel. I would also like to thank all other committee members, Dr. Sanjay K. Banerjee, Dr. Allan MacDonald, Dr. Leonard F. Register, and Dr. Seth Bank for their supports.

I would like to extend my sincere appreciation to my colleagues, Hema C.P. Movva, Stefano Larentis, Feng Wang, Will Burg, and Yimeng Wang. My gratitude also goes to my former group members, Babak Fallahazad, Kayoung Lee, En-Shao Liu, David Dillen, Christopher Corbet, Micha Points, and Jiamin Xue. The experience and knowledge they shared with me were truly the source of my motivation to conduct highest-end research. I also greatly appreciate to close collaborators, Shengquiang Huang, Matthew Yankowitz, and Prof. Brain LeRoy from University of Arizona. I have experienced so many joyful, unforgettable moments with my friends I met at the Pickle Research center (PRC). I thank all former and current members of PRC.

The Microelectronic Research Center (MRC) is truly a great place to work with full of valuable people. I would like to give special thanks to all the staff members at MRC.

Finally, I would like to thank my family, especially my wife, Emaka Takashima for her endless love, devotion, and encouragement. I cannot imagine this long journey without her support. I am also very thankful to my parent Taehyun Kim and Kwangim Jung who taught me valuable lessons in my life. Their presence was a constant motivation for me to

keep going forward. I am also very thankful to my siblings, Shinho Kim and Eunyoung Kim for their thoughtful comments and support.

Electronic Properties and Device Applications of Rotationally Controlled van der Waals Heterostructures

Kyounghwan Kim, Ph. D.

The University of Texas at Austin, 2018

Supervisor: Emanuel Tutuc

Van der Waals heterostructure is a highly versatile platform to unveil two-dimensional (2D) electron physics and to explore new device functionalities. In this dissertation, we present comprehensive experimental studies of van der Waals heterostructures considering the rotational control between different 2D layers. A hemispherical handle polymer stamp is introduced to improve 2D layer transfer, which allows rotational control when stacking 2D layers. To verify the accuracy of rotational control, we demonstrate a rotationally aligned double monolayer graphene using a sequential pick-up of two graphene layers, which originate from a single crystal domain, and compare it with Bernal stacked bilayer graphene using Raman spectroscopy, scanning probe microscopy (SPM), and electrical transport measurements under an applied transverse electric-field. We also demonstrate resonant tunneling in double bilayer graphene heterostructures using hexagonal boron nitride (hBN) as an interlayer dielectric, in which rotational alignment between the two bilayer graphene is the key ingredient for the device functionality. To further highlight the significance of highly accurate rotational alignment between different layers, we demonstrate tunable moiré crystals in small-twist-angle bilayer graphene. A comprehensive electron transport study is conducted, and the

data are compared with SPM results. We observe transport gaps at ±8 electrons per moiré unit cell, along with a conductivity minimum at charge neutrality with twist angle less than 1°. In magnetic fields, we also observe the emergence of a Hofstadter butterfly in the energy spectrum, with four-fold degenerate Landau levels (LLs), and broken symmetry quantum Hall states at filling factors, $\nu = \pm 1, \pm 2, \pm 3$.

We demonstrate dual-gated tungsten diselenide (WSe_2) interlayer tunneling devices, consisting of two WSe_2 monolayers with controlled rotational alignment, and separated by a thin hBN tunnel barrier. In samples where the two WSe_2 have a 0° relative twist the tunneling current-voltage characteristics reveal resonant tunneling, manifested by negative differential resistance, which stem from energy and momentum conservation. Because WSe_2 possesses strong spin-orbit coupling which leads to coupled spin-valley degrees of freedom, controlling the angle between the two WSe_2 monolayers allows us to probe the conservation of spin-valley degree of freedom in tunneling.

Table of Contents

List of Tables

List of Figures

Chapter 1: Introduction

1.1 MOTIVATION

Two-dimensional (2D) van der Waals heterostructures [1] have been a great platform for investigating unique fundamental physics in 2D electronics, and emerging device applications, which possess functionalities that enable beyond CMOS low-power and high-speed logic [2-5]. In 2D layered materials, such as graphene, hexagonal boron nitride (hBN) and transition metal dichalcogenides (TMDs), each layer is weakly bound to neighboring layers with van der Waals interaction, which allows their isolation down to the monolayer limit by micro-mechanical exfoliation techniques. By employing newly developed layer transfer techniques [6, 7], the isolated 2D layers can be assembled into novel van der Waals heterostructures, which may have electronic properties markedly different from the individual layers, and possibly capable of providing a new material system by engineering the band structure.

Although previously developed 2D layer transfer techniques have made a remarkable progress, rotational control in van der Waals heterostructure has remained as a challenging aspect since accessing the information of each layer's crystal direction is not straightforward. This crystal alignment between the layers is ubiquitous in III-V heterostructures since the crystal direction is determined by the orientation of the seed and adjacent layers during epitaxial growth. Recent examples of progress in the precise control between the 2D layers include rotationally aligned two mono- and bi-layer graphene with hBN [8-10] or tungsten diselenide (WSe_2) [11] where they show interesting device functionality in the form of negative differential resistance (NDR) characteristics thanks to momentum-conserving tunneling.

By further improving the rotational control between the two adjacent 2D layers, a new emerging branch of 2D physics, so called moiré physics, can advance the understanding of these artificial heterostructures to a new, unprecedented level of depth. When nearly identical periodic layers are overlaid with a relative twist, a new periodic pattern, which is tunable by twist-angle forms, called moiré pattern. In the 2D system, because both graphene and hBN can be isolated down to perfect atomic crystal sheets, van der Waals heterostructures consisting of these materials are well suitable platforms to create moiré crystals, which can yield a complex electronic system.

The example of moiré crystal structures is rotationally aligned graphene-on-hBN [12-14] and twist-angle bilayer graphene [15-17] van der Waals heterostructures where they show graphene superlattices with van Hove singularities [18] and emergence of Hofstadter's butterfly in their energy spectrum in high magnetic fields [12-14].

Particularly, in the example of graphene-on-graphene van der Waals heterostructures, because the two graphene layers are identical, an extremely long moiré wavelength is accessible in the superlattice structure by controlling the small-twist-angle (STA) between the two layers. In the example of graphene superlattice on hBN substrate, the maximum moiré wavelength is limited to 14 nm due to 1.8% lattice mis-match between graphene and hBN [19]. Along with the full range moiré wavelength accessibility, twist-bilayer graphene system is a model platform to further explore the study of moiré physics in-depth, since graphene has been studied extensively both theoretically and experimentally. Various experimental and theoretical studies of graphene including electronic band structure [20], Landau level (LL) spectrum [21, 22], transport measurements [23, 24], as well as disorder and interactions [25] between the graphene layers are well studied. The latter example of layer interactions and disorder are particularly interesting in moiré physics, especially in the case of larger moiré wavelengths induced by

STA between the layers. Theory [26, 27] predicts that momentum mismatch at Dirac cones in each layer significantly suppresses the coherent interlayer motion at low energy by inducing STA. Additionally, angle dependent suppression of the Femi velocity, where it shows band flattening along with zero Fermi velocity at a series of angles at 1.05°, 0.5°, 0.35°, 0.24° and 0.2°, so-called magic angle, is expected in the system [27]. The realization of STA bilayer graphene [15-17] has recently been exhibited, and gate-tunable Mott insulators and superconductivity at zero magnetic fields [28, 29] have been observed at a magic angle of near 1.05°.

1.2 OUTLINE

This dissertation describes the dissertator's experimental explorations of various 2D van der Waal heterostructures consisting of graphene, TMDs, and hBN. The organization of the dissertation is as follows. Chapter 2 explains two distinct types of van der Waals heterostructures, using graphene and WSe_2. They experimentally probe a number of fundamental material properties of WSe_2, namely the dielectric constant and bandgap. In Chapter 3, a new method to realize the rotational alignment in van der Waals heterostructure is introduced and the accuracy of the alignment is verified by comparing the properties between rotationally aligned double monolayer graphene and Bernal stacked bilayer graphene obtained by exfoliation. Raman spectroscopy, scanning tunneling microscopy (STM), and electric-field induced measurements are used to verify that the obtained heterostructure is indeed bilayer graphene. To illustrate the applicability of the technique, double bilayer graphene heterostructures, using hBN as an interlayer dielectric, are fabricated to observe energy and momentum conserving tunneling. In Chapter 4, to extend the use of high accuracy in rotational alignment, tunable moiré crystals in STA bilayer graphene are fabricated, and comprehensive electron transport study is conducted

along with SPM measurements. In the same devices, by applying high magnetic fields, we observe the emergence of a Hofstadter butterfly in the energy spectrum with four-fold degenerate LLs, and broken symmetry quantum Hall state (QHS) at filling factors $\nu = \pm 1, \pm 2, \pm 3$. In Chapter 5, we investigate the interlayer tunneling properties of WSe_2-hBN-WSe_2 heterostructures, where the coupled spin-valley degrees of freedom in WSe_2 lead to interesting interlayer tunneling characteristics, which differ markedly in devices with a 0^o or 180^o rotational twist between the WSe_2 layers.

Chapter 2: Band Alignment in WSe_2-Graphene Heterostructures

We investigate the electrical properties of WSe_2 using two different van der Waals heterostructures consisting of WSe_2 and graphene using layer-by-layer transfer approach. In van der Waals heterostructures of WSe_2-on-graphen, we use WSe_2 as a top dielectric of dual-gated graphene field-effect transistors (FETs) to extract the WSe_2 dielectric constant along the c-axis (k_{WSe2}). In graphene-on-WSe_2 van der Waals heterostructures, we determine the energy band offset between the graphene charge neutrality and conduction and valence band edges of WSe_2. We observe ambipolar conduction in lateral transport, which is consistent with the characteristic of conventional graphene transport; however, the conductivity saturates at sufficiently high gate positive (negative) bias, due to carrier population of the conduction (valence) band edges in WSe_2. The electron (hole) population at the conduction (valence) band edges are further investigated using magneto-transport measurement where the carrier densities are extracted from Shubnikov-de Hass oscillations, which attribute to QHSs in the graphene layer.[1]

2.1 Introduction

WSe_2 is a layered TMD semiconductor material with a hexagonal crystal structure (a = 3.282 Å , c = 12.961 Å) [31] possessing a thickness dependent bandgap of 1.2 ~ 2.0 eV [32]. The WSe_2 band structure has been investigated theoretically [33-35] and shown to undergo an indirect-to-direct band-gap transition in the monolayer limit [36, 37]. Several proof-of-concept devices including FETs [38-40], solar cells [41, 42], light-emitting diodes [42, 43], photo-detectors [44], and light-emitting transistors [45] have been demonstrated using WSe_2. To further expand the use of WSe_2 in electronic and optoelectronic

[1] This work has been published as Ref.[30] K. Kim, S. Larentis, B. Fallahazad, K. Lee, J. Xue, D. C. Dillen, *et al.*, "Band Alignment in WSe2–Graphene Heterostructures," *ACS Nano,* vol. 9, pp. 4527-4532, 2015/04/28 2015. The dissertator, K. Kim, fabricated the heterostructures devices, performed the electrical characterization, and contributed to data analysis and writing the paper.

applications, and explore new device functionalities, understanding fundamental properties, such as intrinsic mobility, dielectric constant, and band alignment in heterostructures, is crucial. In this chapter, the intrinsic properties of dielectric constant and overall WSe_2 band information will be experimentally extracted by introducing van der Walls heterostructures using monolayer graphene as an adjacent layer to WSe_2.

2.2 DEVICE FABRICATION

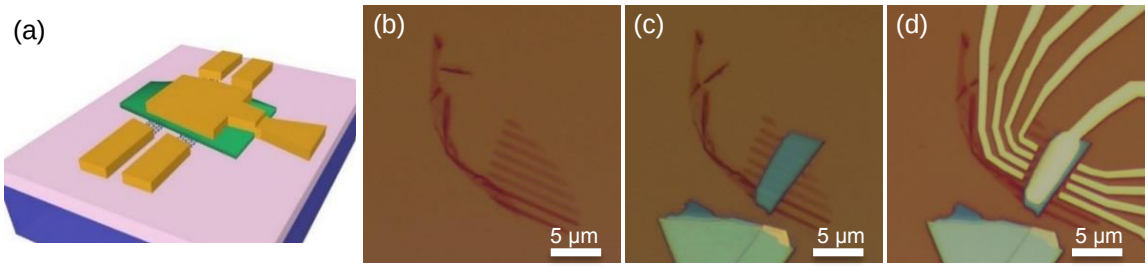

Figure 2.1 Device fabrication of WSe_2-on-graphene [Type #1] (a) Schematic view of WSe_2-on-graphene van der Waals heterostructures. (b) Optical micrograph of trimmed graphene on SiO_2. (c) WSe_2 layer transferred on graphene, and (d) completed device after metal deposition on WSe_2.

Figure 2.1(a-d) shows a device schematic and optical micrographs of sample fabrication steps involving WSe_2-on-graphene van der Waals heterostructures [Type #1]. To fabricate the Type#1 heterostructures, graphene flake is first mechanically exfoliated on 285 nm thick thermally grown silicon oxide (SiO_2) on highly doped silicon (Si) substrate. Raman spectroscopy and optical contrast are used to identify the monolayer graphene. Once we confirm that our exfoliated graphene layer is monolayer, electron-beam lithography (EBL) and oxygen (O_2) plasma etching are used to define a set of 1-2 μm-wide stripes as shown in the figure 2.1(b), followed by ultra-high-vacuum (UHV) anneal for 6 hours at 350°C to remove the poly-methyl-methacrylate (PMMA) residues. Separately, we

mechanically exfoliate WSe_2 flakes onto PMMA spun on water-soluble polyvinyl-alcohol (PVA) layer on a Si substrate. Once exfoliation of WSe_2 flakes is completed, the exfoliated WSe_2 on PMMA/PVA/Si sample is floated on water, which dissolves PVA from the side of the Si substrate, and leaves WSe_2/PMMA floating on water. Using a thin glass slide with 5 mm diameter hole, we fish-out the PMMA membrane carefully to locate the flake near the center of the hole. After drying the PMMA membrane in the air for several hours, we use mask aligner and heating stage to carefully align and transfer WSe_2 flake onto graphene on SiO_2/Si substrate at 90°C, then increase the temperature to 120°C. After the transfer, PMMA is removed in acetone bath for several hours followed by UHV anneal for 6 hours at 350°C. Figure 2.1(c) is the optical micrograph after transfer and UHV annealing processes are completed. To complete the fabrication, a second EBL followed by metal (Ni/Au) deposition is used to define the contacts to the graphene layer, as well as a top-gate onto the WSe_2 flake. The completed device optical micrograph is shown in figure 2.1(d).

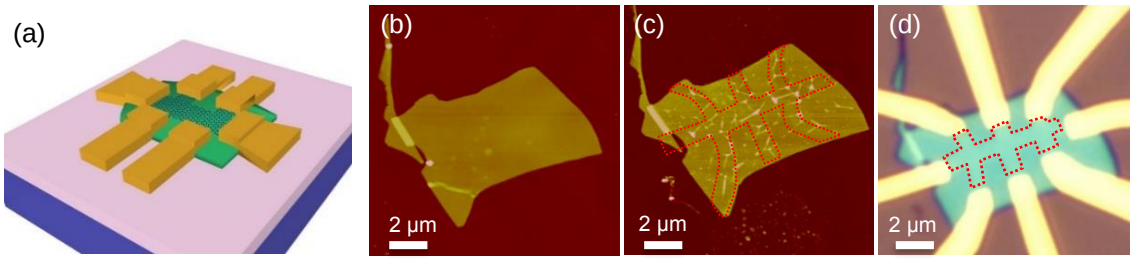

Figure 2.2 Device fabrication of graphene-on-WSe_2. (a) Schematic view of graphene-on-WSe_2 van der Waals heterostructures. (c) AFM topography of exfoliated WSe_2 after UHV anneal, and (c) transferred graphene on WSe_2. (d) Optical micrograph of completed device after metal deposition.

The fabrication of graphene-on-WSe_2 is similar, but the opposite order of stacking is used as described in figure 2.2(a) schematic. WSe_2 flakes are first mechanically exfoliated on 285 nm SiO_2/Si substrates, followed by 350°C UHV annealing to remove tape residues. The flake thickness and topography are probed by atomic force microscopy (AFM) as shown in figure 2.2(b). In a separate PMMA/PVA/Si substrate, monolayer graphene flake is exfoliated and confirmed by Raman spectroscopy. After accurately transferring graphene layer onto WSe_2 flake on SiO_2/Si substrate, EBL and O_2 plasma etching are used to define a Hall bar shape on the graphene monolayer as shown in figure 2.2(c), followed by a second UHV anneal at 350°C to remove the PMMA residues. Red dashed line in the figure 2.2(c) is the indication of the trimmed graphene layer. A second EBL and metal (Ni/Au) deposition are used to define contacts to the graphene layer. Optical micrograph of the final device is shown in figure 2.2(d).

Device ID	WSe_2 thickness (nm)	Graphene Mobility ($cm^2/V \cdot s$)	Heterostructure (Stacking type)	Reference
Device #1	4.6		Type #1 (WSe_2-on-graphene)	WK(1)
Device #2	11.0		Type #1 (WSe_2-on-graphene)	WK(2)
Device #3	14.7		Type #1 (WSe_2-on-graphene)	WK(3)
Device #4	9.8	~ 8,000	Type #2 (graphene-on-WSe_2)	W(36)
Device #5	7.7	~ 12,000	Type #2 (graphene-on-WSe_2)	W(50)
Device #6	10.5	~ 13,000	Type #2 (graphene-on-WSe_2)	W(51)

Table 2.1 Specifications of graphene and WSe_2 used van der Waals heterostructures. WSe_2 thicknesses are measured by AFM and mobility values are extracted from conductance plot at T = 1.4 K. Both types of heterostructures, WSe_2-on-graphene [Type #1] and graphene-on-WSe_2 [Type #2] are specified in the table.

2.3 WSe_2-ON-GRAPHENE VAN DER WAALS HETEROSTRUCTURES

2.3.1 Graphene resistance measurement in WSe_2-on-graphene dual-gated field-effect transistors

In WSe_2-on-graphene van der Waals heterostructures, we use WSe_2 flakes and thermally grown 285 nm SiO_2 as the top and bottom dielectrics of dual-gated FETs to extract the capacitance values of WSe_2 flakes.

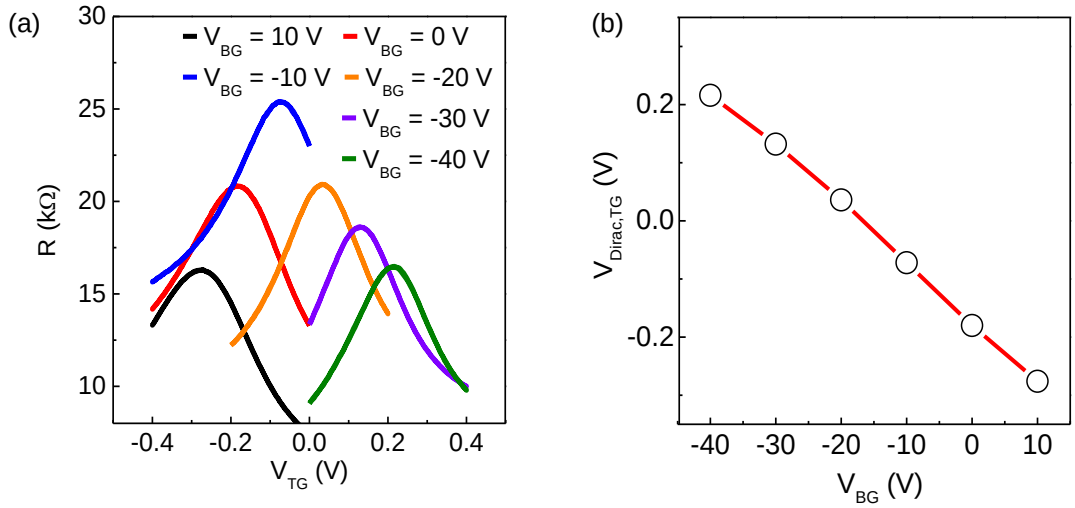

Figure 2.3 Electrical characteristics (a) R vs V_{TG} of dual-gated FETs, at V_{BG} ranging from -40 to 10 V. (b) $V_{Dirac,TG}$ as a function of V_{BG} from -40 to 10 V.

Figure 2.3(a) shows the graphene resistance (R) measured as a function of top-gate bias (V_{TG}), and at different fixed back-gate biases (V_{BG}) ranging from -40 V to 10 V. Each trace shows the typical ambipolar behavior of graphene FETs, with a neutrality point ($V_{TG,Dirac}$) which shifts as a function of V_{BG}. The linear dependence of $V_{TG,Dirac}$ vs V_{BG} data shown in figure 2.3(b) allows the extraction of the top WSe_2 capacitance (C_{TG}) using $\Delta V_{TG,Dirac}/\Delta V_{BG} = C_{BG}/C_{TG}$, where C_{BG} is the capacitance of 285 nm SiO_2, which is 12.5 nF/cm^2 measured at a separate 100 μm × 100 μm metal pad using capacitance-voltage

measurement between the metal pad to highly doped Si substrate as a back-gate. We note that since our analysis uses the gate bias values of the graphene charge neutrality, corresponding to zero chemical potential level, the graphene quantum capacitance does not play a role in this analysis.

2.3.2 Extraction of WSe_2 dielectric constant

To experimentally determine the value of WSe_2 dielectric constant (k_{WSe2}), we examine the top-gate capacitance dependence on WSe_2 thickness (t_{WSe2}) on three different devices with t_{WSe2} values of 5, 11, and 15 nm.

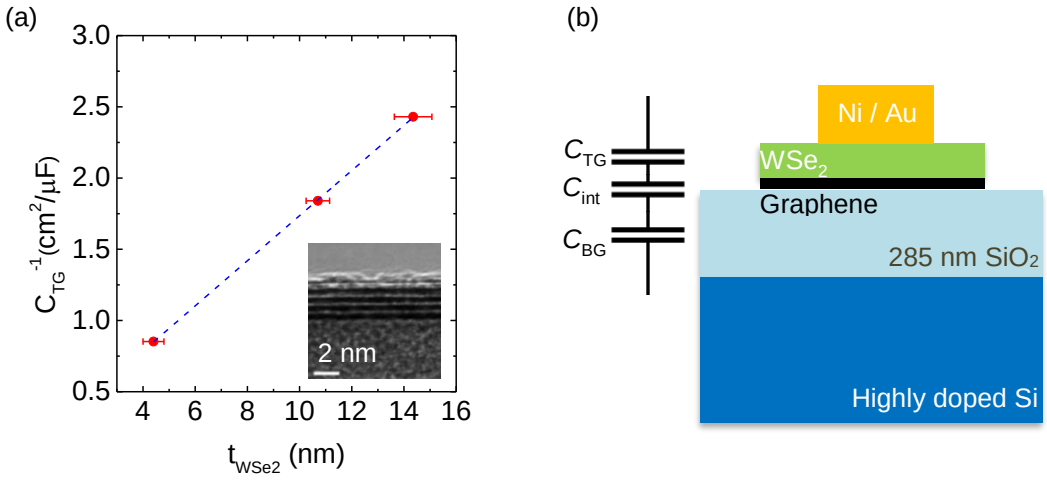

Figure 2.4 (a) Plot of C_{TG}^{-1} as a function of t_{WSe2}. (b) Schematic of series capacitance model.

Figure 2.4(a) shows the C_{TG}^{-1} as a function of t_{WSe2}. The t_{WSe2} values are determined by AFM and listed in Table 2.1. Since the measurement accuracy of t_{WSe2} is important for this analysis, cross-sectional transmission electron microscopy (TEM) of WSe_2 exfoliated on SiO_2 is used as a point of comparison for the AFM measurement of t_{WSe2} as shown in figure 2.4(a) inset. Based on comparison between the AFM data with TEM cross-section

result, we verify that the measured t_{WSe2} using AFM has an error of approximately one WSe_2 layer (~0.7 nm), which is reflected in error-bar in figure 2.4(a).

Figure 2.4(b) shows a simple series capacitance model which describes the WSe_2 capacitance in series with an interface capacitance (C_{int}). We can therefore write C_{TG} as:

$$C_{TG}{}^{-1} = C_{int}{}^{-1} + \frac{t_{wse2}}{k_{WSe_2} \times \varepsilon_0} \quad (2.1)$$

where ε_0 is the vacuum dielectric permittivity. Using a linear fit to figure 2.4(b) data, we extract $k_{WSe2} = 7.2 \pm 0.3$.

2.4 GRAPHENE-ON-WSe_2 VAN DER WAALS HETEROSTRUCTURES

2.4.1 Graphene conductance measurement in graphene-on-WSe_2

We now turn to the experimental investigation of graphene-on-WSe_2 [Type #2] samples, consisting of graphene Hall bars on exfoliated WSe_2 flakes. The following measurement data and analysis are based on the result from Device #4 from Table #1.

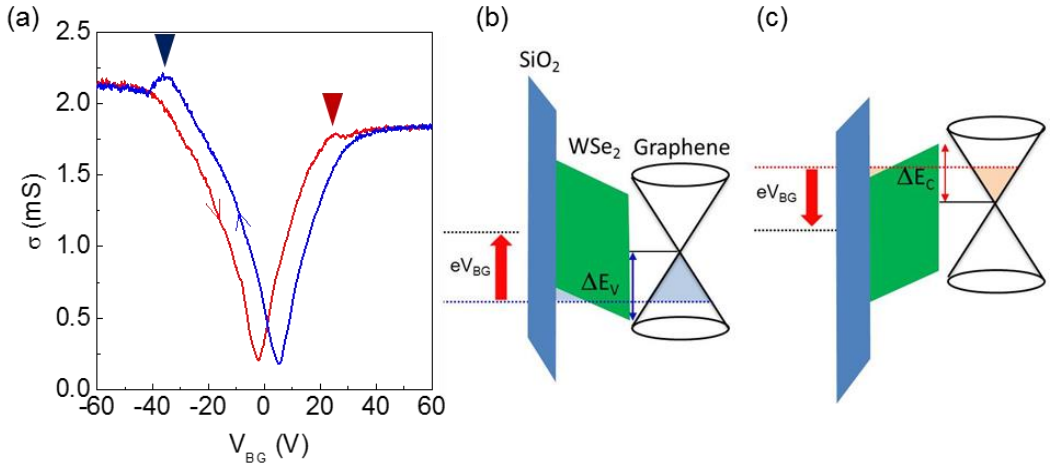

Figure 2.5 Electrical characteristics of Type #2 heterostructure samples. (a) σ vs V_{BG} measured at $T = 30$ K for both V_{BG} sweep directions with 9.8 nm WSe_2 flake. At high positive (negative) gate bias, the conductivity saturates, as marked in red (blue) in the figure, thanks to electrons (holes) populating the WSe_2. The finite hysteresis presents when the WSe_2 is depleted of mobile carriers, which is associated with traps at the SiO_2-WSe_2 interface. (b-c) Band diagram across the heterostructure at high negative [panel (b)] and positive [panel (c)] bias illustrating the WSe_2 valence, and conduction band population, respectively.

Figure 2.5(a) shows the four-point conductivity (σ) vs V_{BG} measured at a temperature $T = 30$ K for a sample with $t_{WSe2} = 9.8$ nm. The plot is similar to the graphene ambipolar conductance, except for a marked saturation at high positive and negative bias. The carrier mobility (μ) in graphene, extracted using $\mu = 1/C_{BG} \times d\sigma/dV_{BG}$ is 7,000 $cm^2/V{\cdot}s$. The figure 2.5(a) also shows a finite hysteresis depending on the V_{BG} sweep direction. We address both these findings in the following section.

The WSe_2 layer acts as a back-gate dielectric for graphene at V_{BG} values below a certain threshold, as marked in figure 2.5(a). While the V_{BG} induced electric-field (E-field) adds an electrostatic potential drop across the WSe_2, the chemical potential remains between the WSe_2 conduction and valence bands. At a positive (negative) V_{BG} threshold, the electrostatic potential drop across the WSe_2 is sufficiently large to bring the WSe_2 conduction (valence) band edge at the WSe_2-SiO_2 interface in coincidence with the

graphene chemical potential level [figure 2.5(b, c)]. Once the WSe_2 starts to become populated with electrons (holes), the carrier density in graphene remains largely insensitive to V_{BG} as the WSe_2 carriers screen the back-gate. The V_{BG} threshold depends on both the offset between the graphene neutrality point and the respective band edge, as well as on the t_{WSe2} and k_{WSe2}. This observation is similar to experimental data in graphene-molybdenum disulfide (MoS_2) heterostructures [46, 47], where conductivity saturation corresponding to the MoS_2 becoming populated with electrons is observed at positive V_{BG} values. In graphene-on-WSe_2 heterostructures, however, we observe signatures of both the WSe_2 conduction and valence band becoming populated with carriers since graphene charge neutrality located close to the middle of the conduction and valence bands edges while graphene-MoS_2 heterostructure possesses the graphene charge neutrality near conduction band edge of MoS_2. We attribute the hysteresis of σ vs V_{BG} of figure 2.5(a) to a finite trap density at WSe_2-SiO_2 interface. In a V_{BG} up-sweep (red trace) the traps become populated concomitantly with the population of the WSe_2 conduction band. During the V_{BG} back-sweep (blue trace), the delocalized electrons in the WSe_2 conduction band respond to the back-gate and are depleted, but the trap states remain charged down to the V_{BG} threshold corresponding to the WSe_2 valence band population with holes. Once the valence band becomes populated with holes, the delocalized holes render the traps charge neutral.

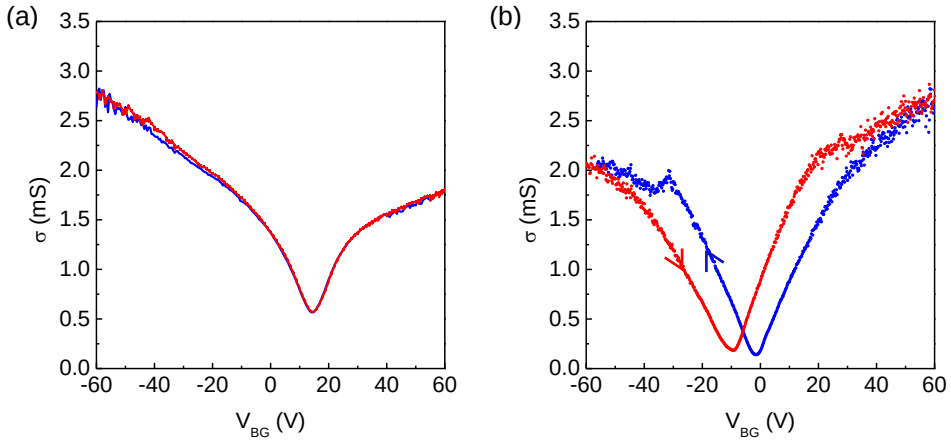

Figure 2.6. Evidence of trap-sites at the SiO_2–WSe_2 interface. (a) σ vs V_{BG} measured from -60 V to 60 V in both directions, for a heterostructure consisting of graphene-on-WSe_2 encapsulated in hBN. (b) σ vs V_{BG} measured for a WSe_2-on-graphene heterostructure using SiO_2 as substrate. Both heterostructures were fabricated using the same WSe_2 thickness of 7.7 nm and measured at 100 K.

To investigate the origin of the hysteresis observed in figure 2.5(a), we realize a WSe_2-on-graphene heterostructure encapsulated by hBN on both sides and measured σ as function of V_{BG} with the same scale from -60 V to 60 V as shown in figure 2.6(a). The plot does not display hysteresis in the σ vs V_{BG} data. This result implies that the hysteresis in σ vs V_{BG} in graphene-on-WSe_2 samples on SiO_2 is associated with the interface between SiO_2 and WSe_2.

2.4.2 Magneto transport measurement

To further substantiate the mechanism described in figure 2.5(b, c) of carrier population at each band edges, magnetotransport measurements are used to measure the carrier density in graphene as a function of V_{BG}. The following data and analysis are on Device #4.

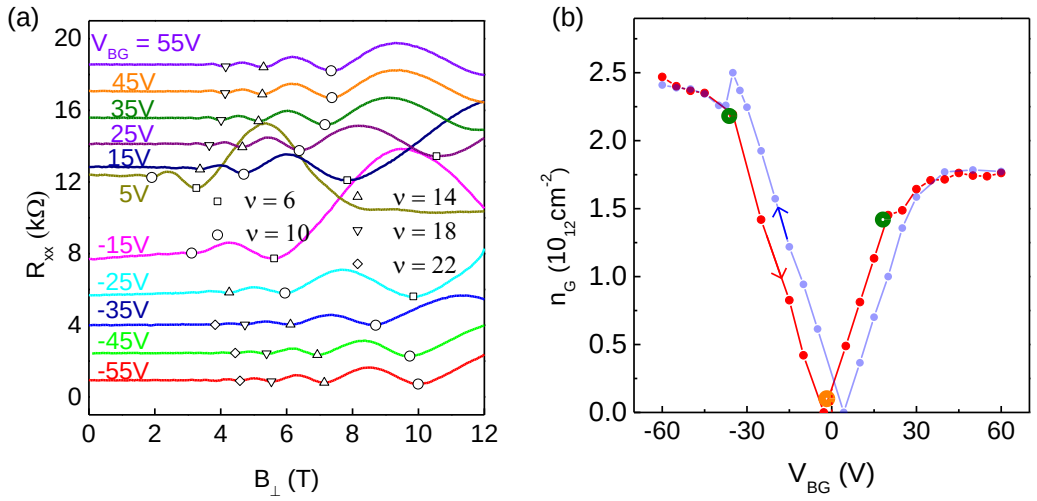

Figure 2.7. Magnetotransport properties of graphene-on-WSe_2 samples. (a) R_{xx} vs B measured at different V_{BG} values and at $T = 30$ K. The SdH oscillations stem from QHSs in the graphene layer. The QHS filling factors ν are indicated in the figure. (b) n_G vs V_{BG} are extracted from panel (a) data.

Figure 2.7(a) shows the longitudinal resistance (R_{xx}) of a graphene-on-WSe_2 heterostructure measured as a function of perpendicular magnetic field ($B_\perp$) at V_{BG} values ranging from -55 V to 55 V. The data displays Shubnikov-de Haas (ShH) oscillations, which we attribute to QHSs in the graphene layer. The QHS filling factors $\nu = \pm 6$, 10, 14, 18 and 22 are marked on each trace. From figure 2.7(a) data, we extract the graphene density (n_G) using $n_G = \frac{eB_\nu}{h}\nu$, where B_ν is the B-field value at filling factor ν, and e and h are electron charge and Plank constant, respectively. More specifically, at each V_{BG} value we determine n_G using a linear fit to the B_ν vs $1/\nu \times (h/e)$ data. Figure 2.7(b) shows the n_G vs V_{BG} extracted from figure 2.7(a) data for both the up-sweep and down-sweep V_{BG} directions. The data show a linear n_G vs V_{BG} dependence at small V_{BG} values, expected for a back-gated graphene layer. At sufficiently large positive (negative) V_{BG} values, n_G departs from the linear dependence, and eventually saturates due to WSe_2 becoming populated with electrons (holes).

2.4.3 Conduction and valence band offset between graphene and WSe_2

In order to determine the band alignment in the graphene-WSe_2 heterostructure, it is necessary to examine the equilibrium conditions including the chemical potentials of the graphene (μ_G) and WSe_2 layer (μ_{WSe_2}). The graphene chemical potential density dependence is $\mu_G(n_G) = sgn(n_G)\hbar v_F\sqrt{\pi|n_G|}$, where $v_F = 1.15 \times 10^8$ cm/s is the experimentally measured Fermi velocity [48]; the n_G values are positive (negative) for electrons (holes). If we reference μ_{WSe_2} with respect to the charge neutrality point of graphene, and define ΔE_C and ΔE_V as the offsets between the graphene neutrality point and the WSe_2 conduction and valence bands, respectively, it follows that $\mu_{WSe_2} = \Delta E_C$ when the WSe_2 chemical potential is at the conduction band edge, and $\mu_{WSe_2} = \Delta E_V$ when the WSe_2 chemical potential is at the valence band edge. The equilibrium condition between the graphene and WSe_2 writes:

$$\mu_G(n_G) + \frac{e^2 n_G}{\epsilon_{WSe2}\epsilon_0} t_{WSe_2} = \mu_{WSe_2} \tag{2.2}$$

We note here that equation (2.2) is valid for a heterostructure where the graphene is assumed undoped at $V_{BG} = 0$ V. If the graphene has a finite doping density (n_0) at $V_{BG} = 0$ V stemming from residues or adsorbates on top of the graphene layer, equation (2.2) rewrites as:

$$\mu_G(n_G) + \frac{e^2 (n_G - n_0)}{\epsilon_{WSe2}\epsilon_0} t_{WSe_2} = \mu_{WSe_2} \tag{2.3}$$

Therefore, by using the measured graphene carrier density at the onset of the WSe_2 conduction (n_{GC}), and valence (n_{GV}) band population, along with n_0, the band offsets ΔE_C and ΔE_V band offset can be calculated as following:

$$\Delta E_C = \mu_G(n_{GC}) + \frac{e^2 (n_{GC} - n_0)}{\epsilon_{WSe2}\epsilon_0} t_{WSe_2} \tag{2.4}$$

$$\Delta E_V = \mu_G(n_{GV}) + \frac{e^2 (n_{GV} - n_0)}{\epsilon_{WSe2}\epsilon_0} t_{WSe_2} \tag{2.5}$$

The green symbols in figure 2.7(b) mark the points at which the values of n_{GC} and n_{GV} are experimentally determined; the orange symbol marks the V_{BG} = 0 V point, where n_0 is extracted. Because of the finite hysteresis as a function of V_{BG}, we use the V_{BG} up-sweep, during which the traps at the SiO_2-WSe_2 interface remain unfilled up to WSe_2 conduction band population threshold for the purpose of calculating the band offsets. Using equations (2.4) and (2.5), and experimental data from two samples with WSe_2 thickness of 9.8 nm (14 layers) and 10.5 nm (15 layers) from Device #4 and #6, we obtain $\Delta E_C = 0.54 \pm 0.04$ eV and $\Delta E_V = -0.77 \pm 0.05$ eV, and a corresponding WSe_2 bandgap of $E_G = \Delta E_C + |\Delta E_V| = 1.31 \pm 0.09$ eV. Using the graphene work function of 4.56 eV [49, 50], we calculate an electron affinity for WSe_2 of 4.06 ± 0.09 eV.

2.5 RAMAN PHOTO-LUMINESCENT MEASUREMENT

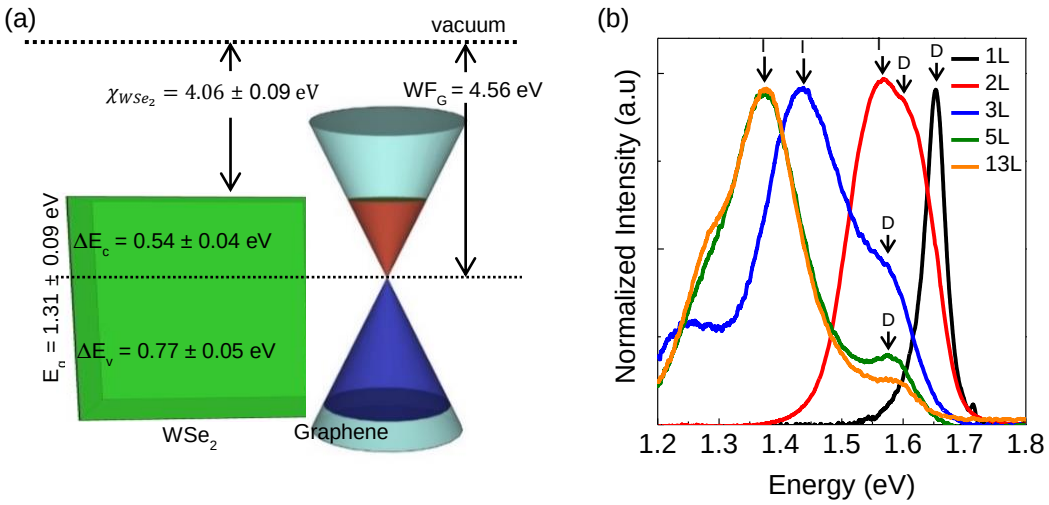

Figure 2.8 (a) PL measurements on WSe2 flakes from monolayer to bulk. Peaks associated with direct and indirect transitions are marked with 'D' and 'I', respectively. (b) Illustration of band alignment summary of graphene and WSe2.

Figure 2.8(a) shows photo-luminescence (PL) measurement on WSe_2 flakes with different thicknesses, ranging from monolayer to more than 10 layers, measured at room

temperature. The direct gap transition and indirect gap transitions are labeled as *D* and *I*, respectively. The indirect gap value determined from electrical characteristics of graphene-WSe_2 heterostructures with t_{WSe2} above 5 nm is relatively in good agreement with the PL measurement. Figure 2.8(b) summarizes the graphene-WSe_2 band alignment information, including the electron affinity values.

2.6 SUMMARY

In summary, we introduce two types of heterostructures using graphene and WSe_2. By investigating their electrical characteristics, we determine key heterostructure properties, such as WSe_2 dielectric constant and WSe_2-graphene band information. These properties are instrumental in designing new device applications, such as graphene-WSe_2-graphene interlayer tunneling FETs [11] similar to the graphene-hBN heterostructures [51-53].

Chapter 3: Van der Waals Heterostructures with High Accuracy Rotational Alignment

In this Chapter, we introduce various transfer techniques using a polymer pick-up stamp, called hemispherical handle substrate. These techniques benefit the realization of van der Waals heterostructures with an accurate rotational alignment between the 2D layers. To prove the accuracy of the transfer technique, we demonstrate a rotationally aligned double monolayer using a sequential pick-up of two monolayer-graphene flakes derived from a single crystalline flake. The accuracy is confirmed by various validations including Raman spectroscopy, STM measurements, and device measurement of transverse *E*-field induced dual-gated bilayer graphene. Finally, to illustrate the applicability of the technique, we fabricate resonant tunneling double bilayer graphene heterostructures using hBN as an interlayer dielectric. Thanks to rotational alignment of the two graphene bilayers in such heterostructures, the interlayer tunneling shows well defined resonances associated with energy and momentum conserving tunneling. The tunneling resonances dependence on dielectric thickness shows the interplay between the hBN interlayer capacitance, and the finite quantum capacitance of bilayer graphene.[2]

3.1 INTRODUCTION

To best explore the electronic properties of van der Waals heterostructures consisting of various 2D materials, such as graphene, hBN, and TMDs, a clean process of stacking layers that minimizes or eliminates the incorporation of residues at the interface is required; therefore, a layer-by-layer transfer technique needs to be developed further to

[2] This work has been published as Ref.[54] K. Kim, M. Yankowitz, B. Fallahazad, S. Kang, H. C. P. Movva, S. Q. Huang, *et al.*, "van der Waals Heterostructures with High Accuracy Rotational Alignment," *Nano Letters,* vol. 16, pp. 1989-1995, Mar 2016. The dissertator, K. Kim, fabricated the heterostructures devices, performed the electrical characterization, and contributed to data analysis and writing the paper.

fulfill this requirement and significantly improve the cleanness at the interface between the layer. Although we successfully achieve the first and the most important requirement for stacking van der Waals heterostructure, which is to produce a clean interface between them, another degree of freedom during stacking, which is to control the crystal axes rotational alignment and registration of successively transferred layers, has been challenging. The latter ingredient, while ubiquitous in epitaxially grown heterostructures, is arguably an important obstacle in realizing electronically coupled, crystallographically registered van der Waals heterostructures using a layer-by-layer transfer approach.

3.2 REALIZATION OF ROTATIONALLY ALIGNED DOUBLE MONOLAYER GRAPHENE

The rotational alignment of the crystal axes in van der Waals heterostructures realized by successive layer transfers has been achieved thus far by using the straight edges of the flakes as crystallographic references. For example, the straight edges of mechanically exfoliated graphene flakes are assumed to be parallel to the zigzag or armchair crystal orientations, and they can be differentiated from each other using polarized Raman spectroscopy [55]. Although this method may provide a straightforward and non-destructive way to determine the crystal orientation of the graphene flakes, the precision for accurate rotational alignments is limited because the edges are not always straight, nor purely zigzag or armchair, but often a mixture of both zigzag and armchair segments, complicating the crystal axes identification. In addition, the finite edge size combined with optical resolution challenges limits the angle determination accuracy to about 2° for typical flake sizes. Here, we introduce a transfer technique that provides a better control of the heterostructure fabrication, and, in particular, allows for accurate crystal axes alignment. The new technique does not impose any limits on the size or shape of the flakes as it relies solely on well-defined metallic alignment marks (200μm apart

Cr/Pt marks) on the substrate instead of the straight edges of the flakes for the accurate rotational alignment. We illustrate the technique by realizing Bernal stacked bilayer graphene using successive transfers of two monolayer graphene flakes with rotationally aligned crystal axes.

3.2.1 Hemispherical handle substrate

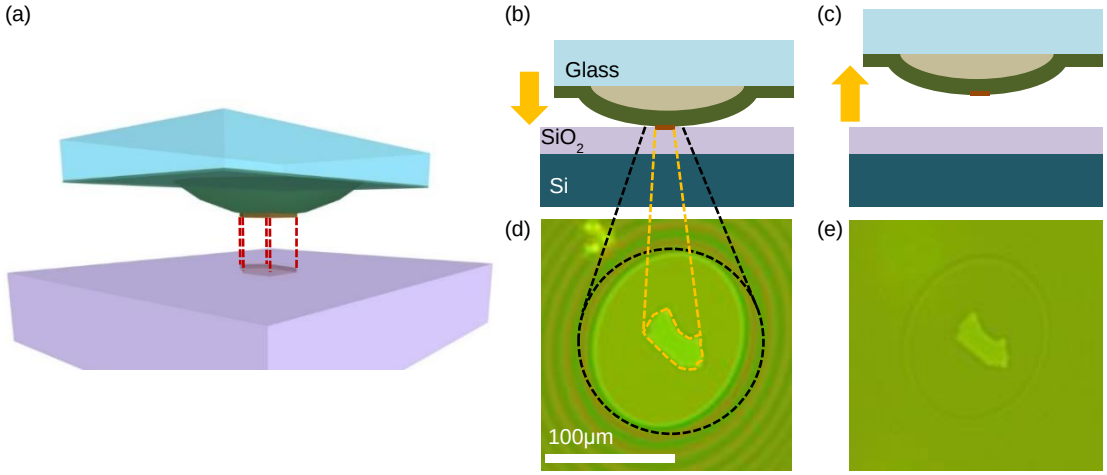

Figure 3.1 (a) Illustration of the hemispherical handle substrate used for selective flake pick-up and transfer. (b-e) Schematic [panel (b, c)], and corresponding optical micrographs [panel (d, e)] of the flake pick-up procedure. The handle substrate is brought into contact with an exfoliated hBN flake [panel (b, d)]. The contact area marked by black dashed line is approximately 100 μm^2. (c) Schematic, and (e) optical micrograph of the hBN transfer to a handle substrate.

Figure 3.1(a) illustrates the hemispherical, bulb-like handle substrate that can be fabricated from a small epoxy or polydimethylsiloxane (PDMS) droplet deposited onto a transparent base substrate, such as glass or a planar PDMS mold. The contact area between the handle substrate and the flake is determined by the hemisphere radius and contact force, and can be as small as 50 μm^2. The hemisphere can be coated with an adhesion-improving polymer, such as PMMA, PVA, or polypropylene carbonate (PPC). Figures 3.1(b, c)

schematically illustrates the selective flake pick-up using a hemispherical epoxy handle, along with an example of an hBN flake pick-up shown in figure 3.1(d, e)

To make a hemispherical handle substrate, we use commercially available epoxy (M-bond 610, SPI Supplies) to make a hemispherical shape on a glass substrate. We use a toothpick or a narrow-end pipette to create the hemispherical shape of the epoxy.

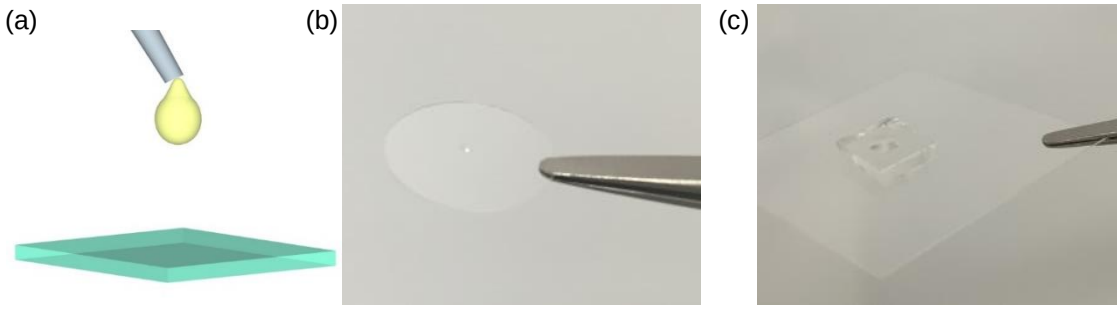

Figure 3.2 Preparation of hemispherical handle substrates. (a) Schematic describing a creation of hemispherical shaped epoxy on a glass substrate using a pipette. (b) Picture of the epoxy on 1 cm diameter glass substrate after curing. (c) Picture of the hemispherical PDMS on the planar PDMS mold that is attached on 1 inch square glass substrate.

Figure 3.2(a) is a schematic of an example placing an epoxy droplet using a narrow-end pipette. After placing the epoxy droplet on a glass substrate, it requires at least 24 hours to cure it completely. For the second type of hemispherical handle substrate, we use a hemispherical PDMS droplet on a pre-made planar PDMS mold. The PDMS solution is made by a mixture of Sylgard 184 prepolymer and curing agent in a 10:1 molar % ratio. To form a hemispherical PDMS, a sharp tip is coated with the PDMS solution, followed by a soft contact with the pre-made planar PDMS as shown in figure 3.2(c). Since PDMS and M-bond 610 epoxy have different hardness after curing is done, the use of these two types of handle substrates can also vary. We find that a handle substrate that used PDMS is softer than the one that used epoxy when we make a contact during pick-up. As a result, the PDMS hemispherical handle substrate has a wider contact area with a less contact force,

compared to the one that used epoxy, which results in a smaller contact area a with stronger contact force. The right handle substrate is chosen to optimize the pick-up and transfer processes based on the pick-up flakes and the conditions of the exfoliated/transferred substrate.

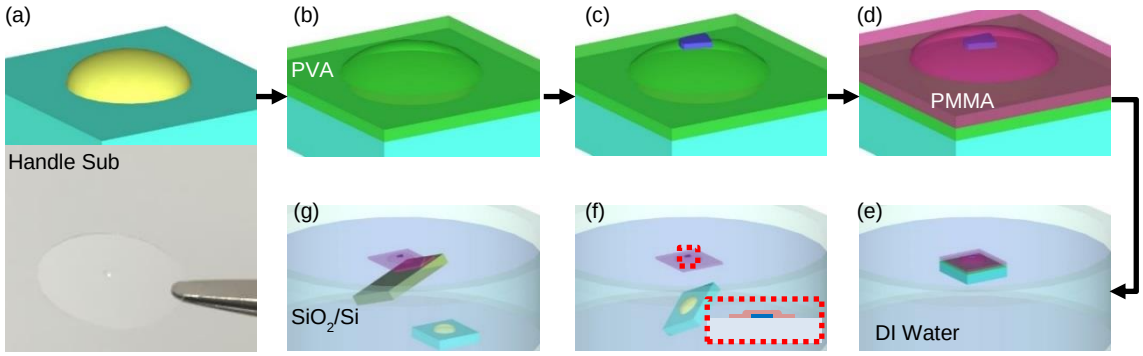

Figure 3.3 Process flow schematics of heterostructure transfer from the handle to a secondary substrate. The last layer picked-up becomes the top-most on the secondary substrate (stacking order reversed). (a) Handle substrate with m-bond epoxy. (b) Spin-coat PVA on handle substrate (c) PVA, a water-soluble polymer is used as an adhesive polymer for individual layer pick-up. (d) Spin-coat PMMA on PVA-coated handle substrate. (e) Handle substrate placed on DI water bath. (f) PMMA membrane floated on the DI water surface. Inset schematic: Cross-sectional view of PMMA/heterostructure on DI water. (g) PMMA membrane is fished out using a SiO_2/Si substrate.

Figure 3.3(a-e) shows detail illustrations of the transfer technique process using hemispherical handle substrate with water soluble PVA as an adhesive pick-up polymer. The key concept in this process is that the last layer picked-up becomes the top-most layer (reverse stacking) on the secondary substrate as a result, which allows to prove the top surface of the layer, such as in i.e. STM measurement.

After preparing the hemispherical handle substrate [figure 3.3(a)], PVA is spun on handle substrate followed by 2 minutes bake at 90°C. After sequential layer pick-up is completed using PVA as an adhesive polymer at 70°C, PMMA is spun on heterostructure/PVA followed by 2 minutes bake at 90°C. Because PVA is water soluble,

by placing the handle substrate on distilled (DI) water bath, only PMMA membrane with heterostructure underneath floats on water [figure 3.3(f)]; inset shows cross-sectional schematic of heterostructure underneath the PMMA membrane. We note here that during layer pick-up processes, we start the pick-up sequence with hBN flake, which can protect the active channel layers from DI water. Above sequence allows active layers to be sandwiched between hBN and PMMA. To complete the heterostructure fabrication, we fish-out the PMMA membrane using secondary SiO_2/Si substrate, then let it dry until DI water is completely removed from underneath the PMMA. Finally, we place the substrate in the acetone bath to remove PMMA followed by 350°C UHV annealing to remove PMMA residues.

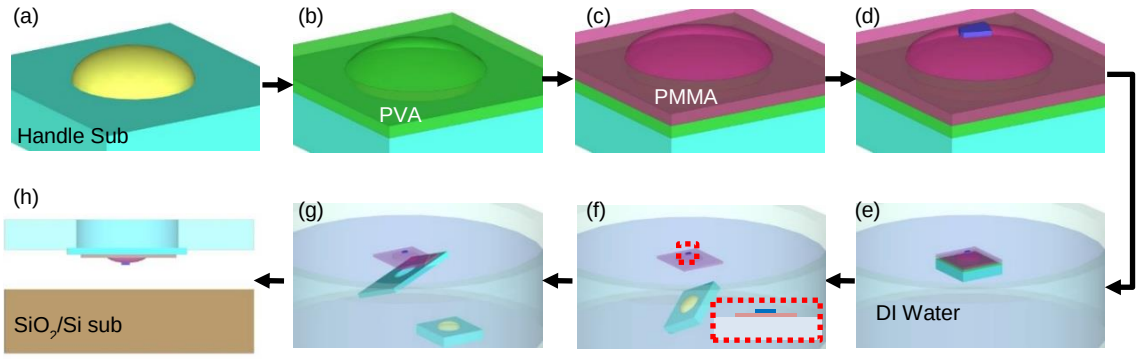

Figure 3.4 Process flow schematics of heterostructure transfer from the handle to a secondary substrate. The first layer becomes the top-most on the secondary substrate (stacking order maintained). (a) Handle substrate with m-bond epoxy on (b) Spin-coat PVA on handle substrate (c) Spin-coat PMMA on PVA/handle substrate. (d) PMMA is used as an adhesive polymer for the layer pick-up. (e) Handle substrate placed on DI water bath. (f) PMMA membrane floated on the DI water surface. Inset schematic: Cross-sectional view of heterostructure/PMMA on DI water. (g) PMMA membrane fished out using glass substrate with a 3 mm hole. (h) Transfer heterostructure on a SiO2/Si substrate using mask-aligner.

Following two figures [figure 3.4 and 3.5] are examples of transfer processes, which allow the layer picked up last to become the bottom most layer (maintaining the

stacking order) in the heterostructure. These methods are widely used for the 2D devices containing hBN encapsulated active layer in the heterostructures. Figure 3.4(a-e) is schematics describing the transfer technique using PMMA as an adhesive polymer during heterostructure fabrication. After PMMA, the hemispherical handle substrate, is ready [figure 3.4(a)], PVA is spun (2000 rpm for 2 mins) on the handle substrate followed by 2 minutes bake on a hop-plate at 90^{o}C. After the cool-down, the handle substrate is spun again (2000 rpm for 2 minutes) on PVA followed by hot-plate bake for 2 minutes at 90^{o}C. Now, the handle substrate is ready for the layer pick-up using PMMA as an adhesive polymer [figure 3.4(c)]. After sequential layer pick-up processes are completed using mask-aligner, it is placed on water bath to dissolve PVA. The difference here compared to a process illustrated in figure 3.3 is seen in the inset figure 3.4(f); now the heterostructure is on top of the PMMA, while in the figure 3.3(f) inset, the heterostructure is underneath the PMMA. To complete the heterostructure fabrication, we fish-out the PMMA membrane using a glass with a 5 mm hole, then place the heterostructure with PMMA on a new secondary SiO_2/Si substrate. After heterostructure is transferred to a new substrate, the sample is placed in the acetone bath to remove the PMMA followed by 350°C UHV annealing to remove PMMA residues.

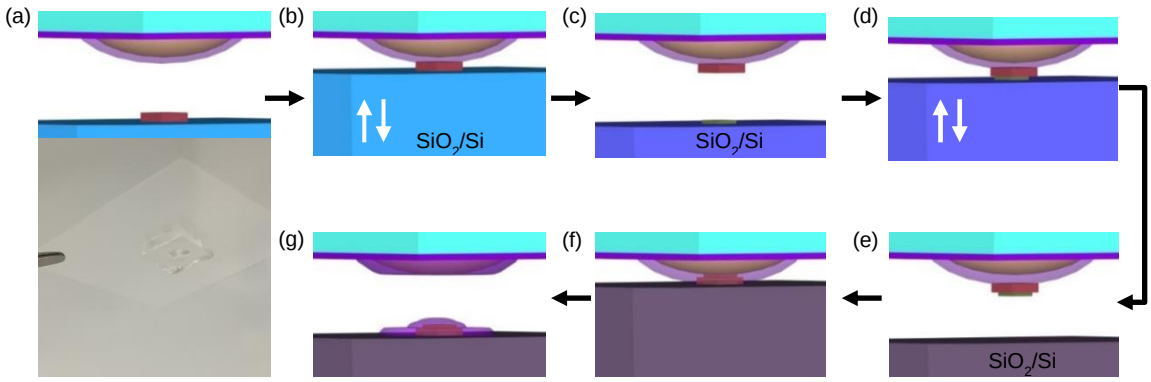

Figure 3.5 Process flow schematics of heterostructure transfer from the handle to a secondary substrate (Heterostructure transfer process #3). The first layer becomes the top-most on the secondary substrate (stacking order maintained). (a) Handle substrate with hemispherical PDMS on planar PDMS. (a-d) Schematics describing two sequential layers pick-up using PPC as an adhesive polymer. (e) Place a new secondary substrate for a transfer (f, g) PPC and heterostructure detached from handle substrate and transferred to a new substrate.

Similarly to figure 3.4 process, where the stacking order of heterostructure on a new secondary SiO_2/Si substrate is maintained, figure 3.5(a-g) describes the same purpose transfer technique but with reduced numbers of steps, thanks to PPC adhesion property, in which polymer adhesion dramatically changes with temperature. Here, we use PDMS hemispherical ball as a base handle substrate. During the pick-up process, we park the temperature at 40~50^{o}C, which is the a proper temperature for pick-up with a strong PPC adhesion. After entire pick-up sequences is complete, we raise the temperature above 90^{o}C, where adhesion of the PPC gets weaker, and eventually PPC (with stacked layers) detaches from PDMS so it can transfer to a new substrate. Using the method in figure 3.5, we are able to skip the processes described in figure 3.4(e-g).

3.2.2 Device fabrication

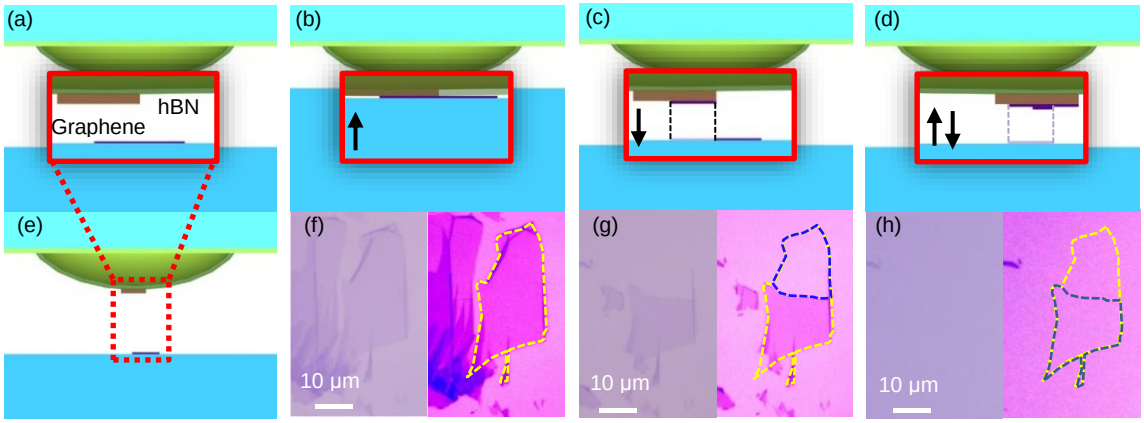

Figure 3.6 Rotationally aligned graphene double layer realized by successive transfers from a monolayer graphene using a hemispherical handle substrate. (a, e) Schematic of layer pick-up. The red box represents a zoom-in view of the hemispherical handle substrate bottom most point. (b-d) Schematics, and (f-h) corresponding optical micrographs of successive stacking steps. Panel (b, f) illustrate a partial contact of the handle with the bottom graphene. Panel (c, g) show the handle substrate release with one graphene section detached. Panel (d, h) illustrate the second contact with the handle translated laterally to create an overlap region of the two graphene layers. Because the two graphene layers are obtained from a single grain, their principal crystal axes remain aligned if the handle is not rotated with respect to the bottom substrate.

Figure 3.6(a-d) describes the process flow of a van der Waals heterostructure consisting of two rotationally aligned monolayer graphene flakes, along with the corresponding optical micrographs [Figure 3.6(f-h)]. This heterostructure is chosen because the rotational alignment between the two layers can be probed post fabrication by Raman spectroscopy, or STM. To create a rotationally aligned double monolayer graphene, we first exfoliate monolayer graphene and hBN on separate SiO_2/Si substrates. The monolayer graphene is confirmed by optical contrast and Raman spectroscopy. A hemispherical handle consisting of PVA coated epoxy is used to first pick-up the hBN flake, which serves as a substrate of the van der Waals heterostructure. The hBN is then aligned partially with a graphene monolayer on SiO_2/Si under an optical microscope, the

hemispherical handle is brought in contact with the substrate, and subsequently detached. Thanks to a stronger van der Waals bonding between graphene and hBN on one hand, and graphene and polymer on the other, the monolayer graphene flake is sectioned, and the area making contact with the hBN is selectively detached as shown in the illustration of figure 3.7(a, b).

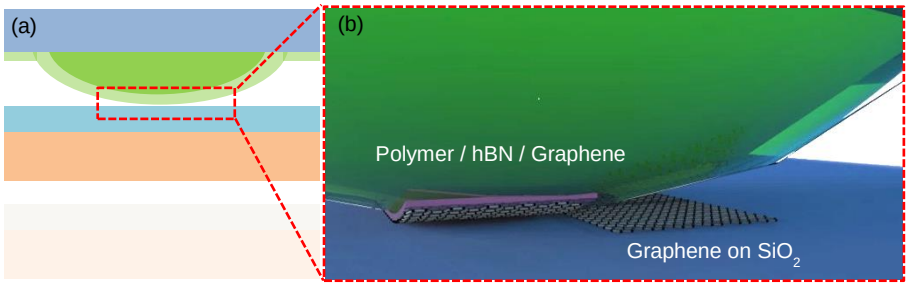

Figure 3.7 Selective graphene pick-up from monolayer graphene using a hemispherical handle substrate; a key process of fabricating rotationally aligned graphene double layer. (a) Schematic of cross-section view of hemispherical handle substrate. Red dashed line indicates contact area between hemispherical handle substrate and flake exfoliated substrate. (b) Schematic of selective graphene pick-up using different van der Waals force between hBN-graphene and adhesive polymer-graphene.

Next, the hemispherical handle is translated laterally, brought in contact with the substrate and detached, in order to pick-up the remaining graphene section [figure 3.6(d)]. Thanks to the single crystal nature of the monolayer graphene, combined with spatial translation of the transfer process, the two graphene monolayers are expected to have rotationally aligned crystal axes.

3.3 CHARACTERISTICS OF ROTATIONALLY ALIGNED DOUBLE MONOLAYER GRAPHENE

To validate the rotational alignment accuracy of the technique, we perform three different methods of Raman spectroscopy, STM, and *E*-field induced resistance measurement and see whether rotationally aligned two monolayer graphene behaves similarly to the natural AB stacked bilayer graphene or not.

3.3.1 Raman spectroscopy measurement

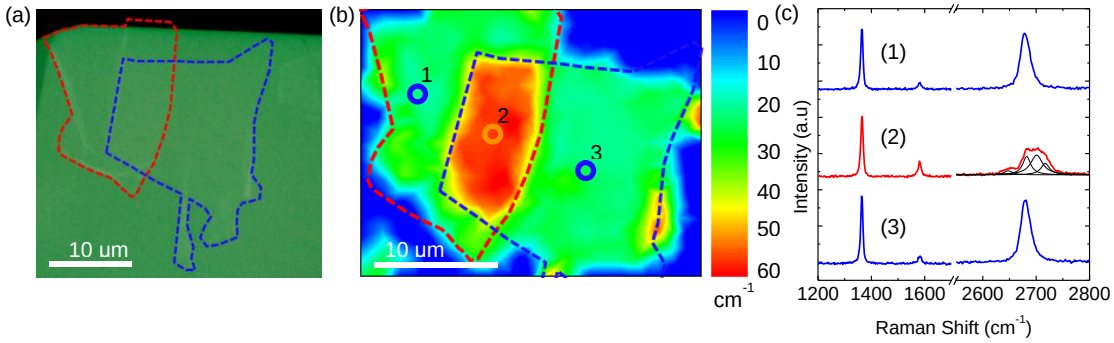

Figure 3.8 Raman spectroscopy characterization (a) Optical micrograph of rotationally aligned double monolayer graphene on hBN heterostructure. The blue and red dashed lines mark the boundaries of two monolayer graphene flakes. (b) Contour plot of the Raman 2D band FWHM corresponding to the optical micrograph of panel (a). The data show a significantly wider 2D band in the overlap region in comparison to the non-overlapped regions. (c) Example of Raman spectra acquired at the locations marked in panel (b). The spectra at locations (1) and (3) show a 2D band FWHM of 25 cm^{-1}, while the spectrum at location (2), in the overlap region has a 2D band FWHM of ~50 cm^{-1}. The 2D band spectra at locations (1) and (3) can be fit with a single Lorentzian, while the spectrum at location (2) is best fit by four Lorentzians, consistent with Bernal stacked bilayer graphene.

Figure 3.8 describes the results of the Raman spectroscopy measurements on the rotationally aligned double monolayer graphene heterostructure shown in the figure 3.6, after it is transferred onto a SiO_2/Si substrate with the graphene layers facing up using the PVA as an adhesive polymer following the steps described in figure 3.3. Figure 3.8(a) shows the optical micrograph of the two rotationally aligned graphene layers on hBN, where the edges of individual graphene flakes are marked with dashed lines. We use the graphene 2D band with full width at half maximum (FWHM) in the overlapping region for an initial assessment of the rotational alignment between the two monolayer graphene flakes. For monolayer graphene, the 2D band FWHM is 24 cm^{-1}, while for a Bernal stacked

bilayer graphene, the 2D band FWHM is approximately twice as large (50 cm^{-1}) [56]. Furthermore, because Bernal stacked bilayer graphene has two electronic energy bands near the neutrality point, four distinct scattering processes contribute to the Raman 2D band, which is best fit by a superposition of four Lorentzians and is blue shifted in comparison to monolayer graphene. The Raman 2D band FWHM of a twisted bilayer graphene is expected to be close to the nominal value of a Bernal stacked bilayer for STAs, and decrease with an increasing twist angle, albeit not monotonically [57]. Figure 3.8(b) shows the Raman 2D band FWHM map of panel (a) sample, measured using a 532-nm excitation wavelength with a spot size of 1 μm and a power of 5 mW. Figure 3.8(b) data show two distinct regions in the area covered by graphene flakes: One region characterized by a 2D band FWHM of ~25 cm^{-1}, corresponding to the non-overlapping sections of the monolayer graphene flakes, and one region characterized by a FWHM of ~50 cm^{-1}, corresponding to the overlapping section. The 2D band FWHM in the overlapping region is consistent with that of Bernal stacked bilayer graphene, suggesting that the rotational misalignment between the two graphene layers is small.

Figure 3.8(c) shows sample representative Raman spectra of the three regions as indicated in figure 3.8(b). Each Raman spectrum shows three distinct peaks at ~1364 cm^{-1}, corresponding to the hBN E_{2g} band, at ~1580 cm^{-1}, corresponding to graphene G band, and at ~2700 cm^{-1}, corresponding to graphene 2D band. The 2D band at spots (1) and (3) can be fit with a single Lorentzian peak, as expected for monolayer graphene, while the 2D band probed in the overlapping region cannot be fit with a single Lorentzian peak. The best fit to the 2D band in the overlapping region is achieved with four Lorentzians, each with

FWHM of ~24 cm^{-1} consistent with the 2D band of Bernal stacked bilayer graphene. We note that in spite of the good agreement between the Raman spectra in the overlapping region, and that of Bernal stacked bilayer graphene, Raman spectroscopy cannot clearly differentiate Bernal stacked bilayer graphene from twisted bilayer with rotational misalignment angles smaller than 3° [57].

3.3.2 Scanning tunneling microscopy measurements

In order to better quantify the rotational alignment of our van der Waals heterostructures, the rotationally aligned double monolayer graphene is investigated using SPM. Metal contacts are patterned in order to allow a bias to be applied between the sample and the substrate, which serve as a back-gate. We characterize this sample on the atomic scale using STM and spectroscopy. All the STM measurements are performed in UHV at a temperature of 4.5 K.

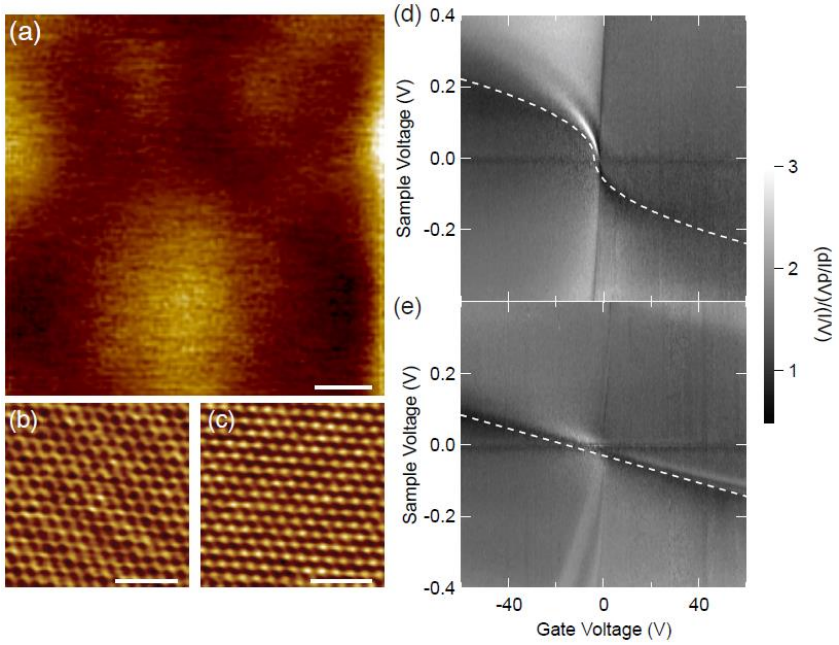

Figure 3.9 Atomic-scale topographic and electronic characterization. (a) STM topography of the bilayer region of the sample. No moiré pattern is observed, indicating that the two graphene layers are perfectly aligned. The scale bar is 30 nm. Atomically resolved topography of the (b) monolayer and (c) bilayer regions of the sample. The appearance of the atomic lattice is easily distinguishable and appears hexagonal in the monolayer region and triangular in the bilayer region. The scale bar is 1 nm for both. The sample voltage is +300 mV, and tunnel current is 150 pA for all images. Normalized (dI/dV)/(I/V) spectroscopy as a function of gate voltage acquired on the (d) monolayer and (e) bilayer regions of the sample. The white dotted lines roughly mark the position of the (d) Dirac point and (e) charge neutrality point.

Figure 3.9(a) shows a 200 nm by 200 nm topographic map taken on the overlapping bilayer region of the sample. No moiré pattern is observed, indicating the two layers of graphene are in essentially perfect rotational alignment. We acquired atomically resolved topography to further characterize the difference between the monolayer and bilayer regions in figures 3.9(b, c), respectively. The topography is easily distinguishable between the two, with the monolayer region appearing hexagonal and the overlapped, bilayer region appearing roughly triangular as anticipated for Bernal-stacked bilayer graphene [58].

Finally, we examine the spectroscopic signatures of both the monolayer and bilayer regions. Differential conductance (dI/dV) spectroscopy measurements were acquired by turning off the feedback circuit and measuring the tunneling current (I) while adding a small 5 mV signal to the sample voltage (V) at a 563 Hz frequency. Figure 3.9(d) and 4(e) show the normalized (dI/dV)/(I/V) spectroscopy as a function of gate voltage in the monolayer and bilayer regions of the sample. The white dotted lines roughly mark the sample voltage of the minimum signal in the normalized dI/dV plot, representing the position of the charge neutrality point. In monolayer graphene, the charge neutrality (or equivalently Dirac point) disperses as the square root of gate voltage due to the linear band structure of graphene. [59] However, the band structure of Bernal-stacked bilayer graphene is quadratic at low energy, so the charge neutrality point is instead expected to disperse linearly with gate voltage. Indeed, this is exactly what we observe in the experimental gate bias maps. Assuming a back-gate capacitance of 9.5 nF·cm^{-2}, corresponding to the 280 nm SiO_2 dielectric in series with a 52 nm thick hBN substrate, we extract a Fermi velocity in the monolayer region of $v_F = 1.05 \times 10^6$ m/s. For the bilayer region, the charge neutrality point shifts roughly linearly in sample voltage by -1.9 mV per volt on the back-gate. This is in reasonably good agreement with prior studies of bilayer graphene [60-62], and corresponds to a Fermi velocity of $v_F = 0.95 \times 10^6$ m/s (assuming an interlayer hopping energy $\gamma_1 = 0.38$ eV). Taken together, the topographic and electronic signatures of the bilayer region strongly suggest it is in a perfectly aligned, Bernal-stacked configuration.

3.3.3 Field induced gap-opening in bilayer graphene

To further verify the realization of Bernal stacked bilayer graphene by successive transfers of rotationally aligned graphene monolayers, we fabricate and characterize dual-gated device consisting of hBN encapsulated double monolayer graphene van der Waals heterostructures. The heterostructures are fabricated with a similar process described in figure 3.6 except that we use transfer process described in figure 3.4 instead of figure 3.3, so that heterostructures we make maintain the pick-up sequence on a new SiO_2/Si substrate.

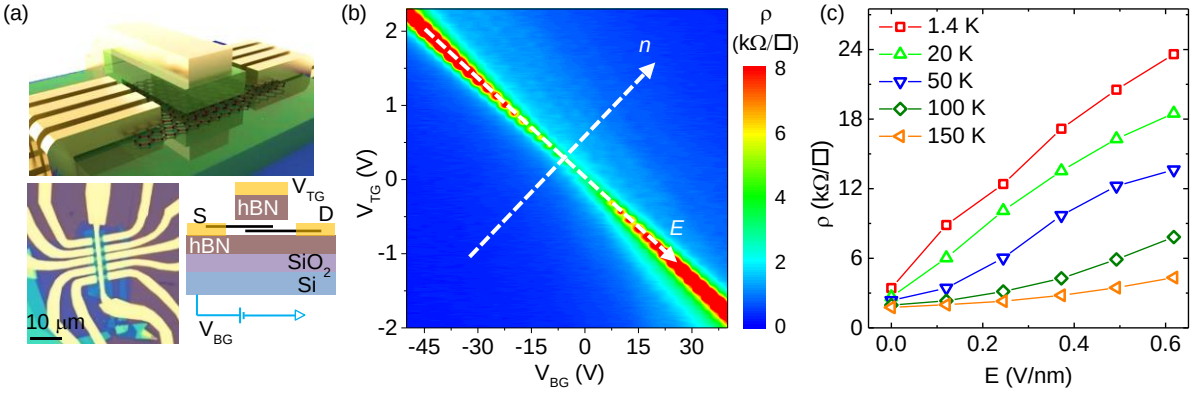

Figure 3.10 *E*-field induced band-gap opening of rotationally aligned double monolayer graphene. (a) Schematic, optical micrograph, and cross-section view of dual-gated FET using rotationally aligned double monolayer graphene as a channel. (b) Contour plot of ρ as function of V_{BG} and V_{TG} at $T = 1.5$K. n and E-field axes are indicated with dashed lines. (c) ρ vs E measured at charge neutrality and at various temperatures from $T = 1.4$ K to 150 K.

Figure 3.10(a) shows completed device illustration, optical micrograph, and cross-section view of its biasing scheme. As shown in the figure 3.10(a), a top-gate electrode is defined on the overlap region by EBL followed by metallization of Cr (4nm) / Au (40nm). Using the top-gate electrode and PMMA as etch mask, a Hall bar is defined by fluoroform

(CHF_3) plasma etching. A sequence of EBL, metal deposition, and lift off is used to create metal contacts to the graphene bilayer.

The dual-gated bilayer device allows independent control of the carrier density (n) and transverse E-field using V_{TG} and V_{BG}, which in turn provides further insight into the bilayer graphene stacking because the resistivity (ρ) dependence on total carrier density and E-field is distinctly different for a Bernal stacked bilayer graphene compared to a twisted bilayer graphene. Indeed, a Bernal stacked bilayer graphene has a parabolic energy-momentum dispersion with a tunable band-gap as a function of the applied E-field, while a twisted bilayer graphene behaves largely as two decoupled graphene monolayers, in which the applied E-field displaces the charge neutrality points of the two monolayers. Figure 3.10(b) shows the contour plot of ρ as function of V_{BG} and V_{TG} measured at 1.5 K. When measured as a function of charge density, the resistivity has one maximum, evincing a single charge neutrality point, which depends linearly on V_{BG} and V_{TG}. Along the charge neutrality line the resistivity increases markedly with the transverse E-field, and shows an insulating temperature dependence as illustrated in figure 3.10(c) consistent with the band-gap opening in Bernal stacked bilayer graphene [63-65]. In contrast, a twisted bilayer graphene does not exhibit a bandgap opening as a function of transverse E-field,[66] and the resistivity at charge neutrality decreases as a function of an applied a transverse E-field [67]. We note here that while the layers are rotationally aligned during transfer, their translation respect to each other is controlled to within 1 μm accuracy, a value much larger than inter atomic spacing. Therefore, a natural question here is why the bilayers obtained by successive, rotationally aligned transfers are Bernal (A-B) stacked, as opposed to e.g.

A-A stacking. We surmise that if the layers are rotationally aligned they will stack vertically in the most energetically favorable, Bernal stacking [68] configuration, as opposed to A-A stacking.

3.4 DOUBLE-BILAYER GRAPHENE WITH HBN IN BETWEEN

To further illustrate the potential of the experimental technique described above, we apply it to a double graphene bilayer resonant tunneling field-effect transistor, an electronic device in which the rotational alignment of the crystal axes is essential for the device functionality. Such devices exhibit a gate-tunable NDR in their inter-layer tunneling characteristics, thanks to energy and momentum conservation. However, because the energy band minima in graphene, and other 2D semiconductors are located away from $\boldsymbol{k} = 0$, to preserve the translation invariance required for momentum conservation in resonant tunneling a high degree of rotational alignment of the two layers is necessary. Indeed, STA between the crystal axes of the two layers can yield a large momentum separation of the band minima at the corners of the Brillion zones, and consequently suppress resonant tunneling between the two layers [10, 69]. In the following, we demonstrate a resonant tunneling device using rotationally aligned double bilayer graphene separated by hBN.

3.4.1 Realization of graphene-hBN interlayer tunneling field effect transistors

To realize the rotationally aligned double bilayer graphene heterostructure with interlayer hBN (IL hBN) in between, we first section a bilayer graphene flake using either an AFM tip as shown in the figure 3.11(a) or by EBL trimming followed by O_2 plasma etching.

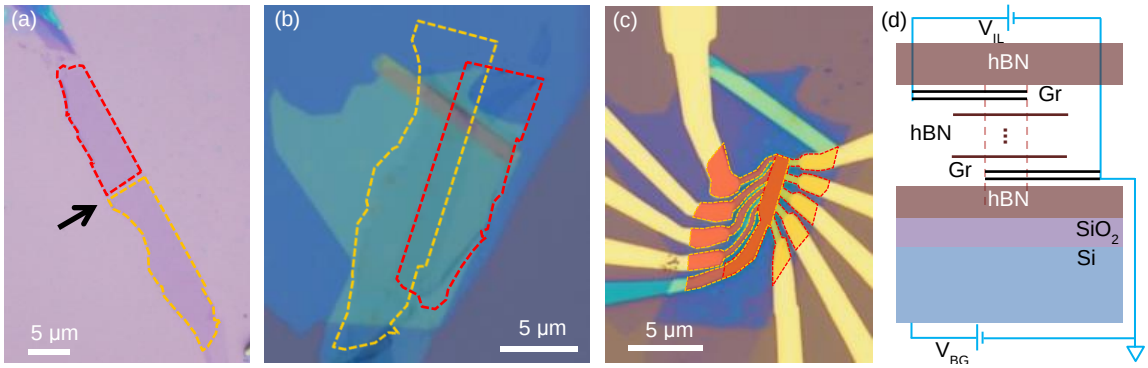

Figure 3.11 (a) Optical micrograph of a bilayer graphene flake sectioned using AFM tip as indicated. (b) Optical micrograph of the rotationally aligned double bilayer graphene separated by IL hBN, after the pick-up and transfer sequence. (c) Optical micrograph of the device after metal contact deposition. (d) Device schematic and biasing scheme.

After sectioning the bilayer, we pick-up one section of the bilayer graphene, followed by a thin hBN flake, and the other section of the bilayer successively. Because the two graphene bilayers are obtained from the same single crystal, their crystallographic directions remain rotationally aligned as long as the handle substrate is only translated during the pick-up sequence. Furthermore, if a substrate rotation is performed at any point during the layer pick-up sequence, its accuracy is mainly determined by the aligner capabilities, and not the flake size. The entire stack is then transferred onto an hBN flake on a SiO_2/Si substrate as shown in the figure 3.11(b). Finally, a sequence of EBL, CHF_3+O_2 plasma etching, electron-beam evaporation of metal, and lift-off is used to complete the device fabrication. An optical micrograph of the rotationally aligned double bilayer graphene heterostructure is shown in the figure 3.11(c). Figure 3.11(d) describes the schematic of device configuration including biasing scheme.

3.4.2 Interlayer tunneling current-voltage characteristics

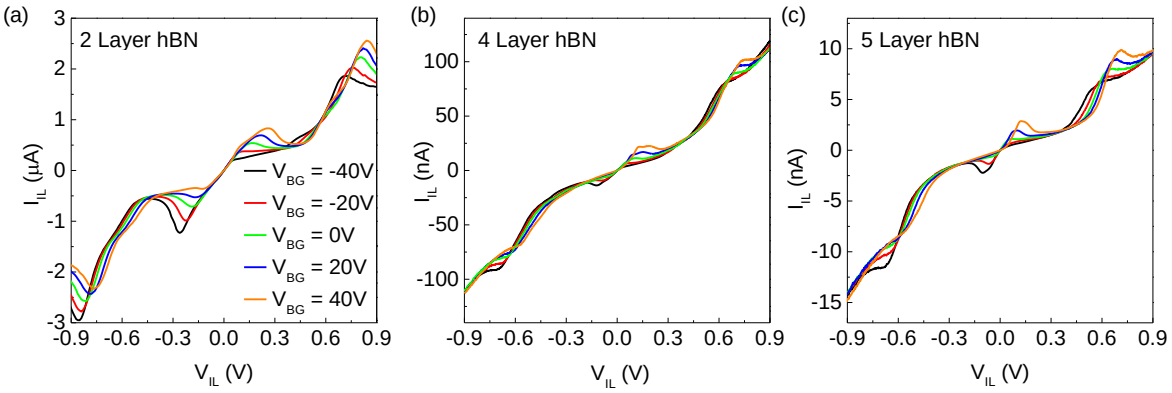

Figure 3.12 (a) I_{IL} vs V_{IL} at different V_{BG} for rotationally aligned double bilayer graphene with two [panel (a)], four [panel (b)], and five [panel (c)] layer-thick IL hBN dielectric. Data show distinct tunneling resonance with negative differential resistance

Figures 3.12(a-c) show the interlayer current (I_{IL}) vs interlayer voltage (V_{IL}) tunneling characteristics for double bilayer graphene heterostructure, with two, four, and five layer-thick IL hBN dielectric, respectively, measured at various V_{BG}, and at a temperature T = 300 K. We determine the IL hBN thickness using a combination of AFM, interlayer capacitance data, and a comparison of the interlayer resistance (R_C) near zero bias normalized by area, with previously reported R_C as a function of number of hBN layers measured in double bilayer graphene devices. [69, 70] The interlayer bias is applied to the top bilayer graphene while the bottom bilayer graphene is grounded.

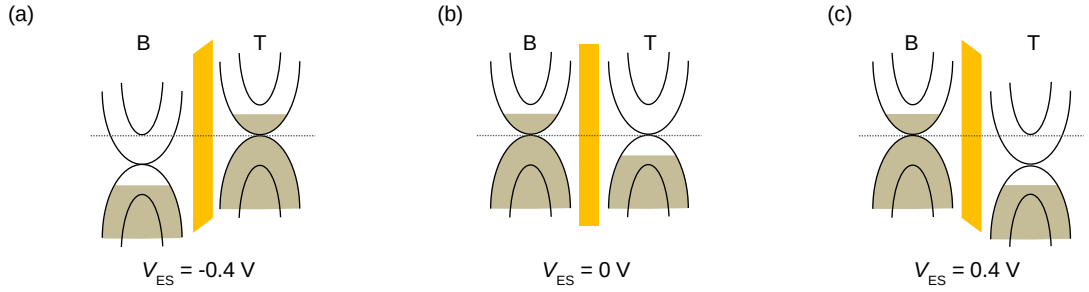

Figure 3.13 (a-c) Energy band diagrams corresponding to the primary and secondary tunneling resonances at V_{ES} = -0.4, 0 , and 0.4 V in panel (a-c), respectively.

We note the I_{IL} vs V_{IL} traces show two sets of resonance with NDR at $|V_{IL}| \cong 0.1$ V – 0.2 V and $|V_{IL}| \cong 0.7$ V - 0.9 V, with a position that shifts as a function of the applied V_{BG}. These resonances stem from momentum-conserving tunneling between the two bilayer graphene flakes, and are explained by examining the bilayer graphene band structure, which possess two conduction (valence) bands: a lower energy band with a minimum (maximum) at the charge neutrality point, and an upper band located at ~0.4 eV from the charge neutrality point as described in figure 3.13(a-c) [71]. The primary resonances at $|V_{IL}| \cong 0.1$ V – 0.2 V are associated with tunneling between the lower energy bands of bilayer graphene, [figure 3.13(b)] [69] while the secondary resonances at $|V_{IL}| \cong$ 0.7 V - 0.9 V are associated with tunneling between the lower energy band of one bilayer and the upper energy band of the opposite bilayer graphene [figure 3.13(a, c)].

3.4.3 Quantum capacitance and interlayer tunneling capacitance

A comparison of figure 3.12 (a-c) data reveal an interesting and counterintuitive dependence of the tunneling resonance on as inter layer dielectric thickness, where the secondary resonances occur at a larger V_{IL} in the device with a thinner interlayer dielectric.

Moreover, the primary resonances are broader in the device with thinner interlayer dielectric. These observations can be explained by considering the interplay between the larger interlayer capacitance at reduced dielectric thickness, and the finite quantum capacitance of bilayer graphene. Indeed, the secondary resonances occur when the lower energy band in one bilayer is energetically aligned with the upper energy band of the opposite bilayer, and therefore the electrostatic potential drop across the interlayer dielectric (V_{ES}) is equal to the separation between the lower and upper subbands (0.4 eV). Reducing the interlayer dielectric thickness at a fixed V_{ES} leads to an increase in the charge density in the two layers, accompanied by a corresponding increase of the layer chemical potential. Because the applied V_{IL} is the sum of the electrostatic potential drop and the layer chemical potentials, a thinner dielectric requires a larger V_{IL} to observe the secondary resonances.

To quantify the above argument, we write $V_{ES} = V_{IL} - (\mu_B - \mu_T)/e$, [10, 69] where μ_T, and μ_B are the top and bottom layer chemical potential, respectively, measured with respect to their charge neutrality point. The primary and secondary tunneling resonances occur when $V_{ES} = 0$ V, and $V_{ES} = \pm 0.4$ V, respectively.

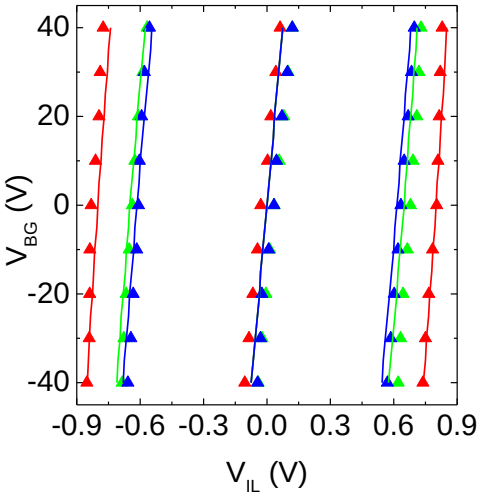

Figure 3.14. Primary and secondary tunneling resonances as a function of V_{IL} and V_{BG}, at for a two layer (blue), four layer (green), and five layer (red)-thick interlayer hBN dielectric. The symbols (lines) are experimental (calculated) values.

Using a band structure model for double layers, and experimentally measured chemical potential layer density dependence [10, 69]in Fig. 5(g), we show the calculated (lines) and experimental (symbols) V_{IL} values for the primary and secondary resonances as a function of V_{BG}, for different interlayer dielectric thicknesses. A C_{BG} of 10.5 nF/cm^2, and C_{IL} values of 3.10 μF/cm^2, 1.80 μF/cm^2, and 1.55 μF/cm^2, from the device with two, four, and five layer-thick IL hBN were used in the calculations.

3.5 SUMMARY

In summary, we describe a novel technique to realize rotationally aligned van der Waals heterostructures, and illustrate it by creating a Bernal stacked bilayer graphene by successive transfers of two monolayers, and also demonstrate gate tunable resonant tunneling FETs in double bilayer graphene. The technique has the potential to be scaled up

using large area graphene single crystals, [72] or TMDs, and can enable various functional van der Waals heterostructures.

Chapter 4: Tunable Moiré Band and Strong Correlations in Small-Twist-Angle Bilayer Graphene

In this Chapter, we realize bilayer graphene moiré crystals with accurately controlled twist-angles smaller than 2° and studied their properties using SPM and electric and magnetic field induced transport measurement. Bilayer graphene is expected to have anomalous electronic properties when it has long-period moiré patterns produced by small misalignments between its individual layer honeycomb lattices. As a result of electron transport, we observe conductivity minima at charge neutrality and satellite gaps that appear at anomalous carrier densities. These features are robust up to large transverse electric fields. In perpendicular magnetic fields, we observe the emergence of a Hofstadter butterfly in the energy spectrum, with four-fold degenerate LLs, and broken symmetry QHSs at filling factors $\nu = \pm 1, 2, 3$. Additionally, we measure a non-local resistance measurement to observe topological current in STA bilayer graphene caused by broken inversion symmetry in moiré crystal structures.[3]

4.1 INTRODUCTION

Moiré patterns form when nearly identical 2D crystals are overlaid with a small rotation [12-14, 74]. The electronic properties of moiré crystals depend sensitively on the ratio of the interlayer hybridization strength, which is independent of twist angle, to the band energy shifts produced by momentum space rotation [19, 66, 75-80]. In bilayer graphene, this ratio is small when twist angles exceed about 2° [78, 81], allowing moiré

[3] This work has been published as Ref.[73] K. Kim, A. DaSilva, S. Huang, B. Fallahazad, S. Larentis, T. Taniguchi, *et al.*, "Tunable moiré bands and strong correlations in small-twist-angle bilayer graphene," *Proceedings of the National Academy of Sciences,* vol. 114, pp. 3364-3369, 2017. The dissertator, K. Kim, fabricated the heterostructures devices, performed the electrical characterization, and contributed to data analysis and writing the paper.

crystal electronic structure to be easily understood using perturbation theory [66]. At smaller twist angles, electronic properties become increasingly complex.

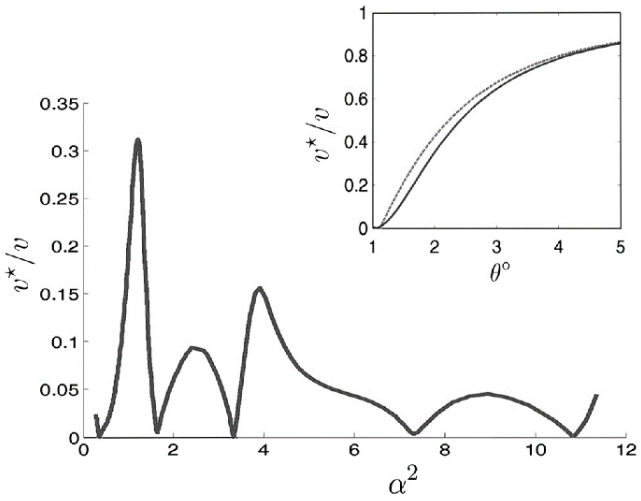

Figure 4.1 (Figure adopted from Ref. [27]) Twisted bilayer band velocity at the Dirac point v^* plotted as function of α^2, where $\alpha = w/vk_0$ for θ from 0.18° to 1.2°. The velocity vanishes at θ = 1.05°, 0.5°, 0.35°, 0.24° and 0.2°.

Figure 4.1 explains extremely flat bands, which appear in twisted bilayer graphene at a series of magic angles with the largest degree of 1.05° followed by 0.5° and 0.35°. Flat bands in 2D electron systems, for example the LL bands that appear in the presence of external magnetic fields, allow for physical properties that are dominated by electron-electron interactions, and have been a friendly territory for the discovery of fundamentally new states of matter. In this chapter, we realize the bilayer graphene moiré crystals with a carefully controlled STA.

4.2 MOIRÉ BLOCH BANDS IN TWIST BILAYER GRAPHENE

The first Brillouin zone (BZ) of monolayer graphene is hexagon in reciprocal space. When a second layer is added on top of the first layer with a twist angle (θ), the two BZs corners are displaced from each other by a wave-vector $\Delta K = 2Ksin\,(\theta/2)$.

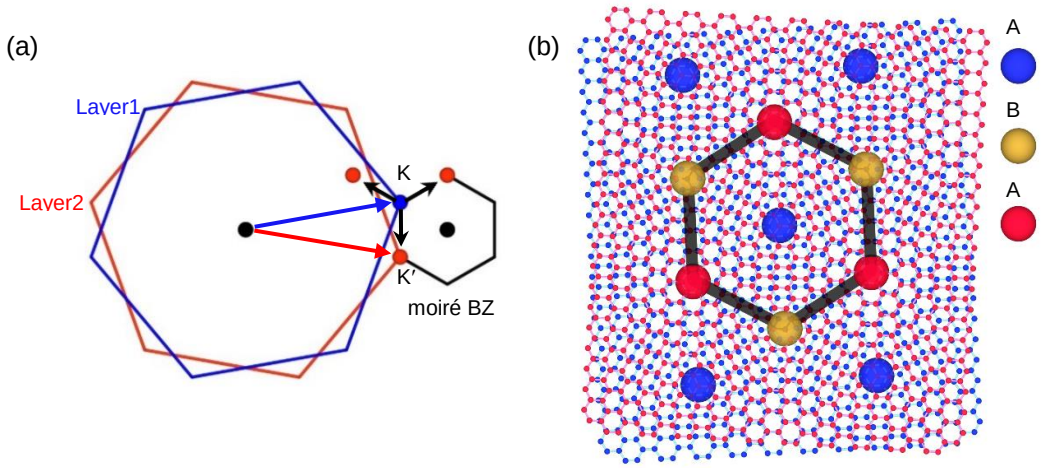

Figure 4.2 (a) Schematic of the first BZ of each graphene layer and of the moiré BZ by twist angle between the two graphene layers in reciprocal space. (b) Illustration of the local stacking in twisted bilayer graphene in real space. AB, BA, and AA stacking configurations are marked by blue, orange, and red circle.

In the figure 4.2(a), K is the magnitude of the reciprocal lattice vector at the BZ corner at which the gap between conduction and valence bands closes in graphene. This relative rotation between the layers leads to a new BZ called moiré BZ with reciprocal lattice vectors that are proportional to the twist angle. In real space, the rotation between the two graphene layers is manifested by a long wavelength moiré pattern with, $\lambda = \frac{a}{2sin(\theta/2)}$ where a is the graphene lattice constant. Within the moiré pattern unit cell, the local bilayer stacking configuration varies by AB, BA, and AA-like stackings marked by blue, orange, and red respectively in the figure 4.2(b). Gradual changes between AA-like regions where the real space hexagons lie nearly on top of each other, and alternating AB and BA, which are the Bernal stacking configured regions where half the lattice points of one layer are in the middle of the hexagonal plaquettes of the other are readily recognized in the generically non-crystalline structure.

A good starting point for thinking about the electronic properties of STA bilayer graphene in the non-perturbative regime is to employ the electronic structure that adds

interlayer tunneling to individual layer Dirac models, and accounts for the structural moiré pattern illustrated in the figure 4.2(b) through a corresponding spatial pattern in the sublattice dependence of tunneling. This model does not account for atomic relaxations in the individual layer honeycomb lattices, which are certainly present, or for electron-electron interactions. Because it has the periodicity of the moiré pattern, this model is relatively easily solved numerically by taking an advantage of translational symmetry, and yields (moiré) bands in a momentum space BZ defined by the moiré pattern. In theory, each band in the moiré BZ accommodates 4 electrons per moiré period when spin-valley degrees of freedom are included.

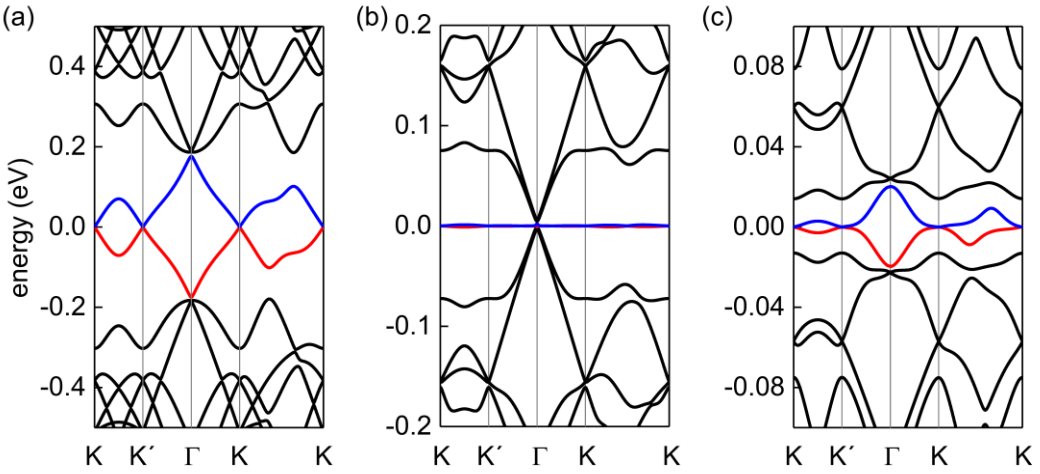

Figure 4.3 Calculated moiré energy band diagram at twist-angle $\theta = 2^{\circ}$, 1°, and 0.7° for (a-c), respectively. The lowest energy bands above and below charge neutrality are shown in blue and red, respectively.

Figure 4.3(a-c) show the model's predictions for different twist angles where we see that even for twist angles as small as $\cong 2°$ (5, 10, 13), the Dirac cones (linear band crossings) of the isolated layers, centered at K and K′ respectively, are still recognizable. The van Hove singularity that appears at the mid-point between K and K′ is an important feature of twisted bilayer graphene's electronic structure in the perturbative regime and

produces observable features in the tunneling density of states (TDOS). The gap between conduction and valence bands is largest at the moiré BZ center (Γ). For twist angles smaller than ≅ 2° however, the low-energy band structure begins to depart qualitatively from the perturbative limit, becoming highly sensitive to twist angle. The moiré bands at the first magic twist angle (≈1°) are illustrated in figure 4.3(b), where we see that the lowest conduction and valence bands are extremely flat, and nearly degenerate at the Γ point, where some higher energy bands are also present at low energy. For twist angles below the first magic angle, the low-energy bands seem to partially recover their perturbative regime form, except that a second pair of flat bands appears at low energy as shown in figure 4.3(c).

4.3 SAMPLE PREPARATION

Two types of sample fabrication processes are introduced here to experimentally investigate the electrical properties of STA bilayer graphene. They are hBN encapsulated and channel exposed STA bilayer graphene devices for electron-transport and SPM measurements, respectively. The key difference between the two fabrication processes is to reverse (use transfer process described in Chapter 3, figure 3.3) or to maintain (use transfer process described in Chapter 3, figure 3.4 and 3.5) the stacking order after sequential pick-up steps of hBN and graphene flakes. For all of the samples, we use hemispherical handle substrate, which allows an individual flake to be partially detached from a substrate while leaving flakes in its immediate proximity intact.

4.3.1 Device fabrication of STA bilayer graphene

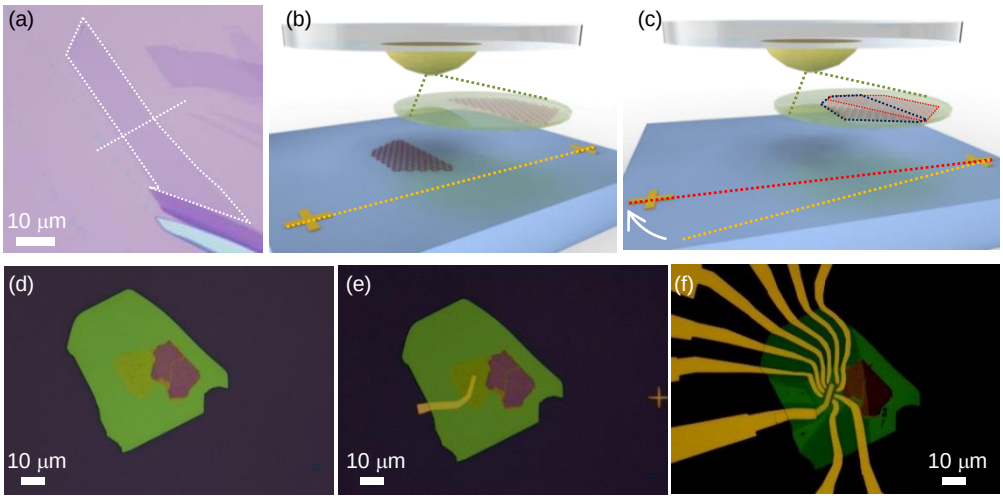

Figure 4.4 (a) Optical micrograph showing a single graphene flake, subsequently split into two sections along the dotted line. (b, c) Schematic illustrations of the first section detaching from the substrate using a hemispherical handle followed by the second section pick-up from the substrate. The substrate is rotated by a small angle between the two steps. Because the two flakes stem from the same graphene domain, STA is introduced between the crystal axes of the individual layers. (d) Optical micrograph of an hBN encapsulated STA bilayer graphene van der Waals heterostructure. (e) Optical micrograph after top-gate (Cr/Au) deposition is completed. (f) Optical micrograph of completed device after side-contact metallization (Cr/Pd/Au).

Figure 4.4(a-f) shows schematic illustrations and optical micrographs describing hBN encapsulated device fabrication processes. The sample fabrication begins with micro-mechanical exfoliation of graphene and hBN flakes on separate SiO_2/Si substrates. Monolayer graphene is then identified using optical contrast and Raman spectroscopy measurement of 2D band with FWHM, while atomic force microscope is used to determine the hBN thickness and to probe the surface topography. Once exfoliated flakes are ready, we start with a single graphene flake and split it into two separate sections as indicated in figure 4.4(a). Sectioning the graphene flakes can be done by either AFM tip or EBL + O_2 plasma etching. Once two graphene flakes are ready from single crystalline flake, we need

to prepare the hemispherical handle substrate. The handle substrate is first coated with an adhesive polymer of PMMA or PPC. After its adhesive polymer is spun on the handle substrate, the STA bilayer graphene heterostructure is fabricated using a series of angle resolved transfers, as illustrated in figure 4.4(b, c). The separated flakes are sequentially picked-up by an hBN flake attached to the hemispherical handle.

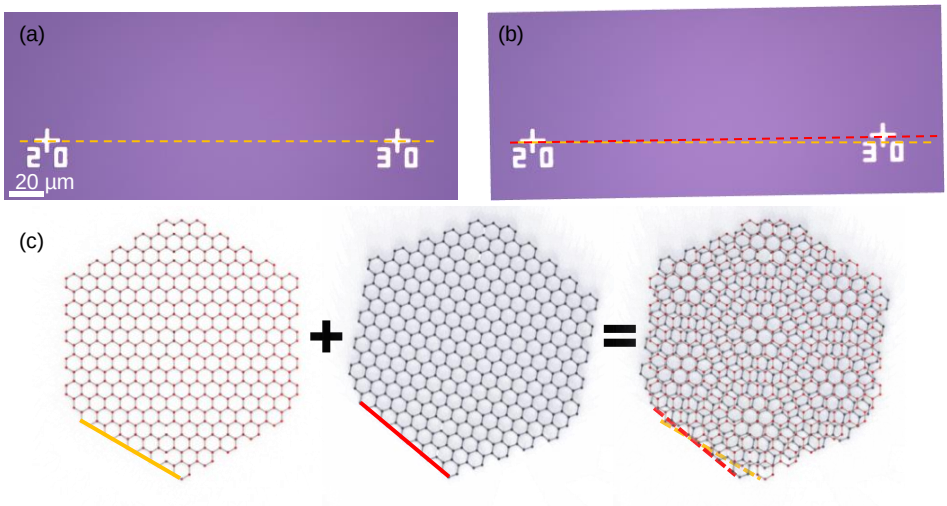

Figure 4.5 (a, b) The example of a 1° rotation control using two alignment marks. The separation between the metal alignment marks is 200 µm. After a section of the flake is picked-up, the bottom substrate is rotated by a desired angle, while the transfer handle remains stationary. (c) Schematic illustration of the moiré pattern formation as a result of the twist angle between the two layers.

During the sequential pick-up of the two graphene flakes, the substrate is rotated by a small angle that can be controlled to 0.1° accuracy between the first and the second graphene flake pick-up. The 0.1° accuracy is achieved by the precise rotational control of the mask aligner (MJB4) and by referencing the two graphene layers using relatively large distance (200 µm), which separates metal (Cr/Pt) alignment marks as shown optical micrograph images in the figure 4.5(a, b). Because the two graphene sections stem from the same crystal grain, they have crystal axes that are aligned at the onset. The substrate rotation yields a controlled twist between the two graphene layers and forms a moiré crystal

as described in figure 4.5(c). After the flake pick-up sequence and transfer is completed, UHV annealing at 350 °C was performed to remove polymer residues [figure 4.4(d)]. Because STA bilayer graphene is encapsulated by two hBN flakes, the twist angle between the STA bilayer graphene is largely displaced instead of reconstructing as Bernal stacking configuration. To complete the device, EBL followed by Cr (5nm) / Au (40nm) electron-beam evaporation is performed to define the top-gate of the device [figure 4.4(e)]. Then, a 2^{nd} EBL and CHF_3 + O_2 plasma etching step is used to define a multi contact hall-bar shaped device. To contact the STA bilayer graphene device, we use Cr (2nm) / Pd (20nm) / Au (40nm) edge metal contacts [figure 4.4(g)].

The samples used for the SPM measurements are fabricated similarly to the method described above with a main difference that the STA bilayer graphene does not have a top-gate stack. We use PVA as an adhesive polymer on hemispherical handle substrate during the fabrication steps, and as a result, we can reverse the stacking order, in a way so that it allows to probe the channel by STM tip. In the process, because the two layers of STA bilayer graphene have a tendency to rotate and form a Bernal stacked bilayer graphene during annealing [54], EBL followed by Cr (5nm) / Au (50nm) metal deposition are performed prior to the UHV anneal to secure the flakes onto the bottom substrate and to define the metal contacts for a measurement.

4.4 CHARACTERIZATION

4.4.1 Conductance measurement in STA bilayer graphene

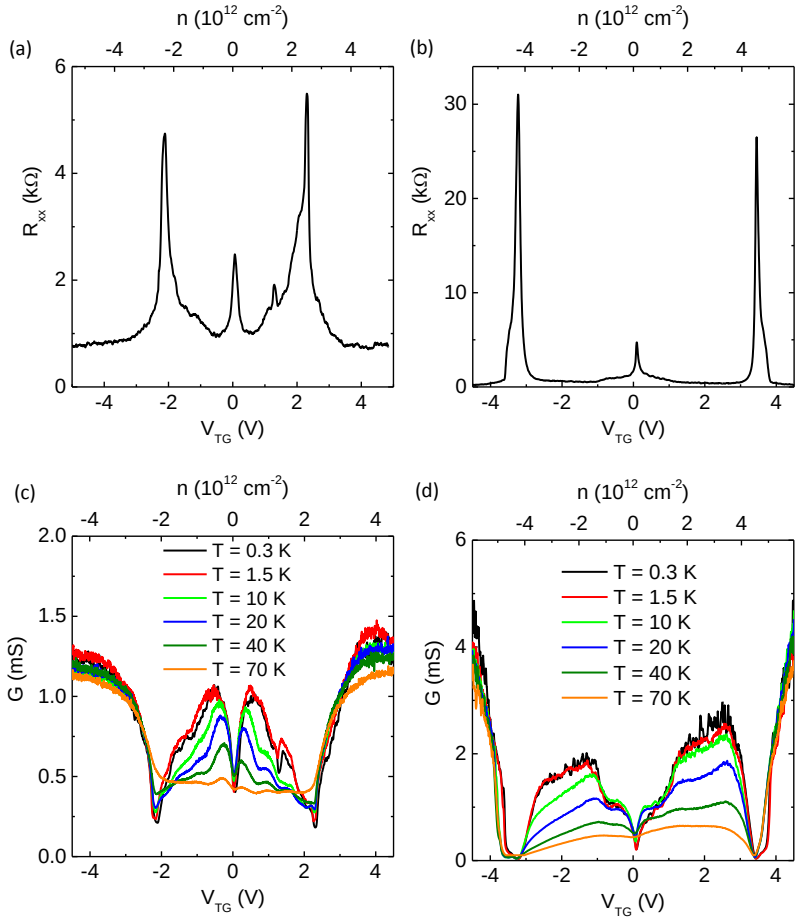

Figure 4.6 (a, b) R_{xx} vs V_{TG} (bottom axis) and n (top axis) at T = 0.3 K for STA bilayer graphene with angles of 0.72º and 0.97º. (c, b) G vs V_{TG} (bottom axis) and n (top axis) measured in 0.72º and 0.97º STA bilayer graphene samples at different temperatures T = 1.6 K to 70 K.

Figure 4.6(a, b) are two samples shown longitudinal resistance (R_{xx}) as function of V_{TG} (bottom axis) and n (top axis) at base temperature of 0.3 K, and figure 4.6(c, d) show the four-point conductance (G) vs V_{TG} data measured in an STA bilayer graphene device at different temperatures (T) with twist angle at 0.7º and 0.97º, respectively. The data show a local conductance minimum when the carrier density (n) approaches zero (charge

neutrality) that is similar to the top-gated monolayer graphene samples. Additionally, two pronounced satellite conductance minima are observed at V_{TG} = ± 2.2 V (± 3.4 V), corresponding to $n = \pm 2.5\times10^{12}$ cm^{-2}($n = \pm 4.45\times10^{12}$ cm^{-2}) for 0.72 (0.97) STA bilayer graphene. As temperature increases, conductance minima of neutrality and satellite are weaken, and no sharp conductance peaks are visible above 80 K. This observation is quite different from the density dependence plot of the conductance expected in either Bernal stacked bilayer graphene [24, 82-84] or large angle twisted bilayer graphene [67]. Surprisingly, the plot is rather similar to the conductance of graphene closely aligned with an hBN substrate [12-14, 74]. We associate the two satellite conductance minima with filling the first two bands of states produced by the moiré crystal with electrons or holes. Unexpectedly, the satellite conductance minima are more pronounced than for graphene on hBN, occur at different carrier densities per moiré period, and have a temperature dependence that suggests a gap opened for charged excitations.

4.4.2 SPM in STA bilayer graphene

Because we expect a strong dependence of electronic properties on twist angles, it is critically important that the angle achieved by the rotation process be directly measured. To this end, we employ STM and SPM measurement to examine the topography of the long wavelength moiré patterns and their local electronic properties [18, 79, 85-87].

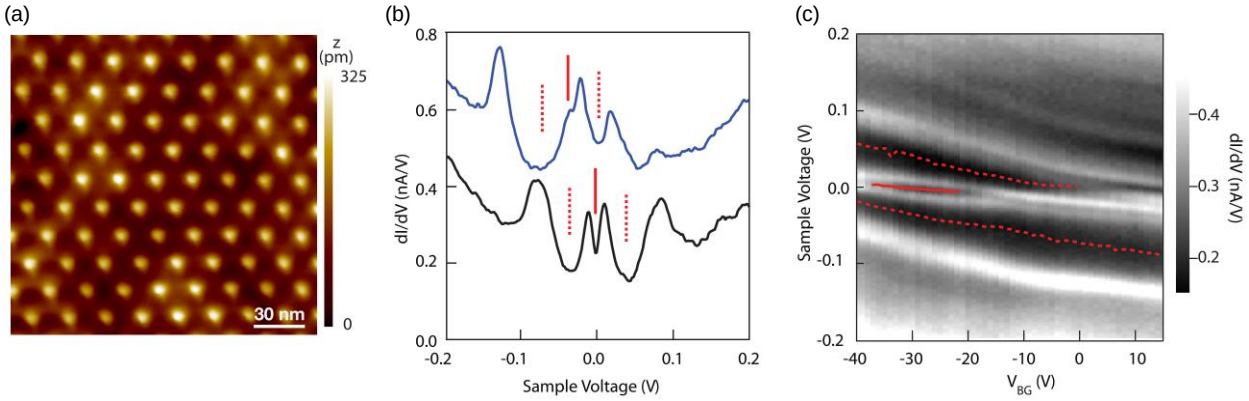

Figure 4.7 (a) STM topography image showing λ= 20.1 nm moiré pattern. The sample voltage is 0.3 V and the tunnel current is 100 pA. (b) TDOS at two different gate voltages -31 V (black) and +2 V (blue). The features corresponding to the charge neutrality point, and the secondary dips in the TDOS curves are marked by solid, and dashed lines, respectively. (c) TDOS as a function of sample voltage and gate voltage. The solid and dashed lines trace the movement of the charge neutrality point and the secondary dip in the TDOS. The data of panel (a-c) were collected at T = 4.5 K.

Figure 4.7 (a) shows an STM topography image of a moiré pattern with $\lambda = 20.1 \pm 0.6$ nm, corresponding to a twist angle of $\theta = 0.7 \pm 0.03°$. The AA stacked regions appear as bright spots, demonstrating that the low-energy TDOS is enhanced at these sites, consistent with theoretical studies [26]. To understand the electronic properties more deeply, we perform TDOS spectroscopy measurements as a function of position. The spatially averaged results measured at V_{BG} = -31 V applied on the doped Si substrate, such that the sample is undoped are shown in figure 4.7(b) (black trace). We observe two low-energy TDOS peaks flanking the charge neutrality point (red solid line at the Fermi level), followed by two dips in the TDOS marked by red dashed lines. Two additional TDOS peaks occur at higher energies. Using the V_{TG}, we tune the carrier density and find that at V_{BG} = 2 V the first conduction band TDOS dip aligns with the Fermi level, while the dip associated with the charge neutrality point weakens (figure 4.8(c), blue trace). Using the measured moiré unit cell area $A = \frac{\sqrt{3}}{2}\lambda^2$ and the C_{BG} of 10.8 nF/cm^2, we find that the

conduction band TDOS dip corresponds to a bilayer density of 7.8 ± 0.6 electrons per moiré unit cell, corresponding to two electrons for each spin-valley degree of freedom.

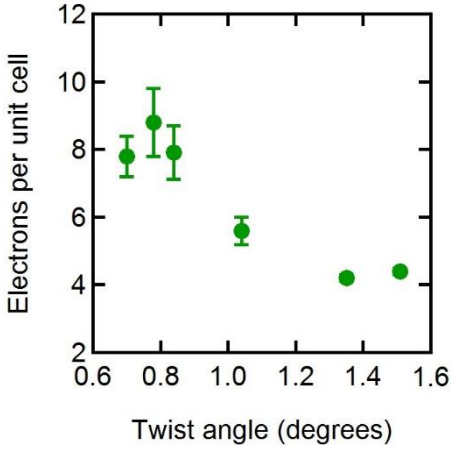

Figure 4.8 Number of electrons per moiré unit cell as function of twist angle between the two graphene layer. Angle extracted from moiré wavelength from STM measurement and number of electrons per moiré unit cell is derived from the density in TDOS measurement.

Figure 4.8 is the summary plot of number of electrons per moiré unit cell as a function of twist angle measured by SPM, and we verify our observation from four more moiré patterns with twist angles ranging between 0.7° - 1° and contrast with observations made in the larger twist angle perturbative regime (above 1.2°), which show dips near 4 electrons per moiré unit cell. The complete evolution of the TDOS with V_{TG} is plotted in figure 4.7(c). The data show a central peak, which remains near the Fermi level for all gate voltages, splits when the sample is at charge neutral (V_{BG} = -31 V), and moves upward in energy relative to a more rigid background as the central peak states are occupied. The movement of the two dips associated with filling 8 electrons per moiré period are shown by the dashed lines for both the conduction and valence bands. These qualitative changes

in TDOS shape with carrier density do not occur in isolated graphene sheets or at larger twist angles and can be explained only by electron-electron interaction effects.

4.5 ELECTRON TRANSPORT IN STA BILAYER GRAPHENE.

Device	C_{TG} (nF/cm^2)	C_{BG} (nF/cm^2)	mobility ($cm^2/V \cdot s$)	Aimed Angle (°)	moiré wavelength (nm)	# of electrons per moiré unit cell	Actual Angle (°)	Reference (Sample ID)
#1	152	9.0	22.7 K	0.6	32.6	8	0.43	GG (9)
#2	174	8.6	7.2 K	0.8	20.1	8	0.72	GG (7)
#3	147	9.4	37.2 K	1.1	16.5	8	0.86	GG (10)
#4	211	9.4	20.2 K	1.2	14.5	8	0.97	GG (12)
#5	282.4	85.7	18.3 K	1.5	9.5	4	1.49	GG (18)

Table 4.1 Specifications of STA bilayer graphene samples.

Table 4.1 summarizes the hBN encapsulated STA bilayer graphene samples which are used for electron transport measurements. A total of 5 samples are listed here. In all of the samples, there is a tendency that the actual angle is 0.1° to 0.2° lower than the aimed angle during fabrication steps. During annealing, although samples are hBN encapsulated,

STA bilayer graphene layers tends to form Bernal stacking (θ = 0°), which is the lowest energy state.

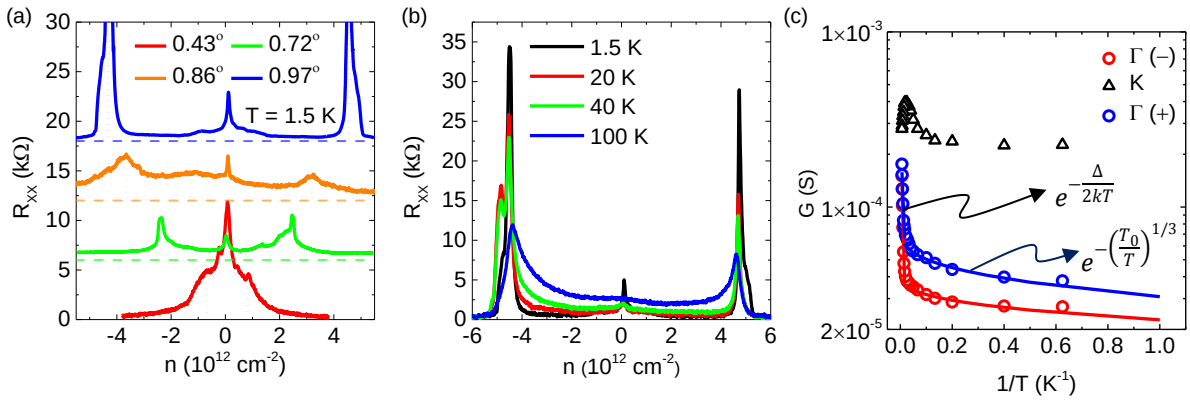

Figure 4.9 (a) R_{xx} vs n measured at T = 1.5 K in STA bilayer graphene with different twist angles at θ = 0.43°, 0.72°, 0.86°, and 0.97°. (b) R_{xx} vs n at different temperatures measured in an STA bilayer graphene sample with a moiré wavelength λ = 14.1 nm corresponding to θ = 0.97°. (c) Arrhenius plot of G measured at the K and Γ points in the sample of panel (b). The data show an activated dependence at elevated temperatures consistent with an energy gap, coupled with variable range hopping at low temperatures.

In figure 4.9(a), we present the four-point longitudinal resistance (R_{xx}) vs n measured in a series of bilayer graphene samples with twist angles θ < 1°. The data show R_{xx} local maxima at neutrality, along with pronounced satellite R_{xx} maxima at finite n values. Based on the observation in figure 4.8 summary plot of STM measurement data, the θ values are assigned assuming a carrier density of ± 8 electrons per moiré unit cell at the satellite R_{xx}. We note that the θ values determined using this assumption are smaller by 0.1° - 0.2° with respect to the relative rotation angle used during the graphene layers transfer. We attribute this reduction to a tendency of the two graphene monolayers to rotate toward Bernal stacking (θ = 0°) during the annealing steps that follow the layer transfer as shown in summary Table 4.1. This observation is also verified by STM measurements.

Figure 4.9(b) shows R_{xx} vs n in an STA bilayer graphene with $\theta = 0.97°$, measured at different temperatures. The data show insulating temperature dependence at $n = \pm 4.5\times10^{12}$ cm^{-2}, suggesting a gap opening at ± 8 electrons per moiré unit cell and weaker temperature dependence at charge neutrality. Figure 4.9(c) summarizes the G vs T^{-1} values at charge neutrality (K), and at $n = \pm 4.5\times10^{12}$ cm^{-2} (Γ(+) and Γ(-)). The Γ(+) and Γ(-) data can be fit by assuming the combination of activated $\left(G \propto e^{-\frac{\Delta}{2kT}} \right)$, and variable range hopping $\left(G \propto e^{-\left(\frac{T_0}{T}\right)^{1/3}} \right)$ conduction processes, with an energy gap $\Delta = 15$ meV, where k is the Boltzmann constant and T_0 is the fitting parameter. The presence of the transport gap is qualitatively consistent with figure 4.7(c) data, and the gap value is comparable with the estimated interaction scale for electrons localized in one period of the moiré pattern.

A potential energy difference between the layers can dramatically change bilayer graphene electronic properties, for example, by giving rise to a tunable band gap in Bernal stacked bilayer graphene. To reveal the role of a potential energy difference induced by a transverse E-field on the transport properties of STA bilayer graphene, in figure 4.10(a-d), we show contour plots of R_{xx} vs V_{TG} and V_{BG} in the θ = 0.43°, 0.72°, 0.97°, and 1.49° samples at $T = 1.5$ K. In the plot, R_{xx} maxima are continuously present at charge neutrality and satellite at 0, and ±4, ±8, electrons per moiré unit cell, over a wide range of transverse E-fields. Figure 4.11(a-d) replot the same data as a function of the density per moiré unit cell (n/n_0), and $E = (C_{TG} \cdot C_{BG} - C_{BG} \cdot V_{BG})/2\varepsilon_0$.

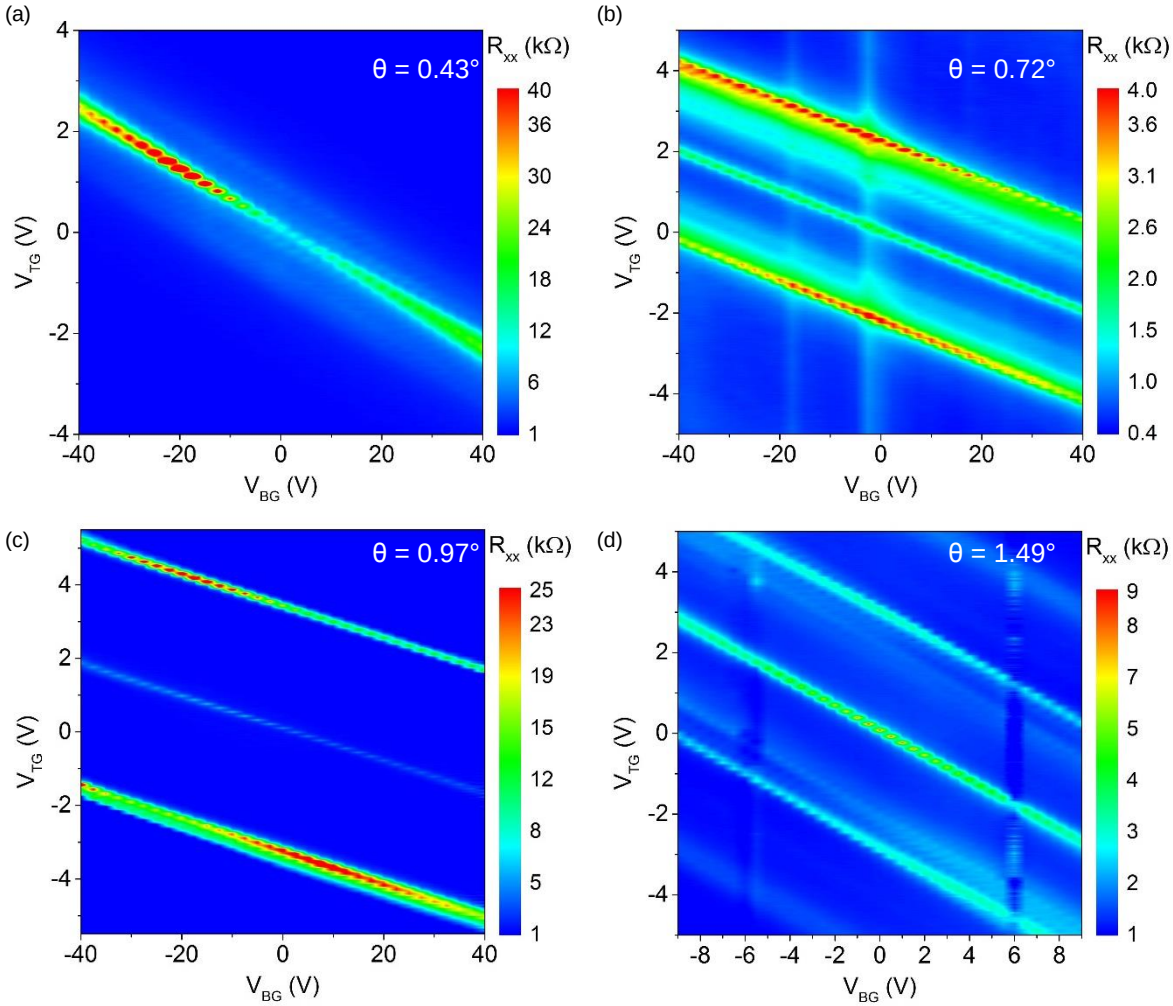

Figure 4.10 (a-d) Contour plots of R_{xx} vs V_{TG} and V_{BG} measured at $T = 1.5$ K in the STA bilayer graphene sample with $\theta = 0.43°$, $0.72°$, $0.97°$, and $1.49°$. We assume 8 electrons per moiré unit cell in panel (a-c) and 4 electrons per moiré unit cell in panel (d).

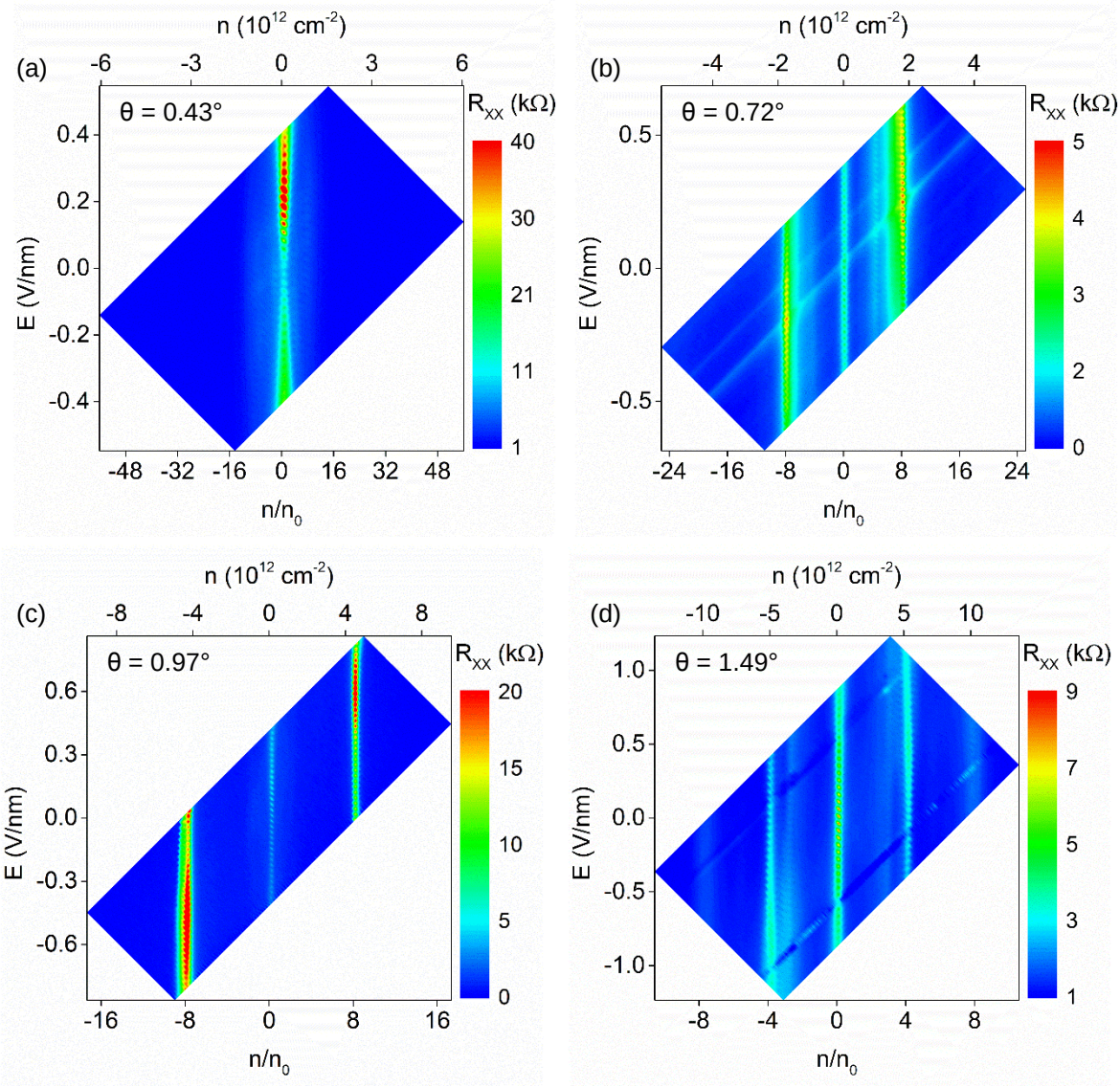

Figure 4.11 (a-d) Contour plots energy (E) as function of n (top axis), n/n_0 (bottom axis), and transverse E-field at $T = 1.5$ K in the STA bilayer graphene sample with $\theta = 0.43°$, 0.72°, 0.97°, and 1.49°.

We associate the appearance of satellite resistance peaks with ± 8 electrons per moiré period for twist angles below the first magic angle of 1.05°, instead of ± 4 electron density expected in the perturbative regime [16, 17] of larger angle above magic angle, This also align well with our observation from SPM study in figure 4.8. The appearance of

an electron-electron interaction induced pseudo-gap at neutrality can be understood in terms of the expected instability of linear band crossings (Dirac bands) in 2D at small Fermi velocities. Its insensitivity to a displacement field between the layers can be understood in terms of the strong hybridization between layers in low-energy bands at STAs (15, 30).

4.6 MAGNETOTRANSPORT AND HOFSTADTER BUTTERFLY.

To better understand the physics in STA bilayer graphene, we measure magnetotransport properties of STA bilayer graphene. An example of R_{xx} and Hall resistance (R_{xy}) vs V_{TG} measured at perpendicular magnetic field ($B_{\perp}$) of 10 T in an STA bilayer graphene sample with $\theta = 0.97°$ is shown in figure 4.12(a). Figure 4.12(b) shows the evolution of the QHSs as a function of E-field examined in the same sample by sweeping V_{TG} and V_{BG} at $B_{\perp} = 12$ T. The data show that R_{xx} at neutrality is reduced in an applied E-field, suggesting a weakening of the (ν, s) = (0, 0) state. While the observation is similar to the evolution of the lowest orbital LL QHSs in Bernal stacked bilayer graphene, which is associated with the spin-to-valley polarized transition.

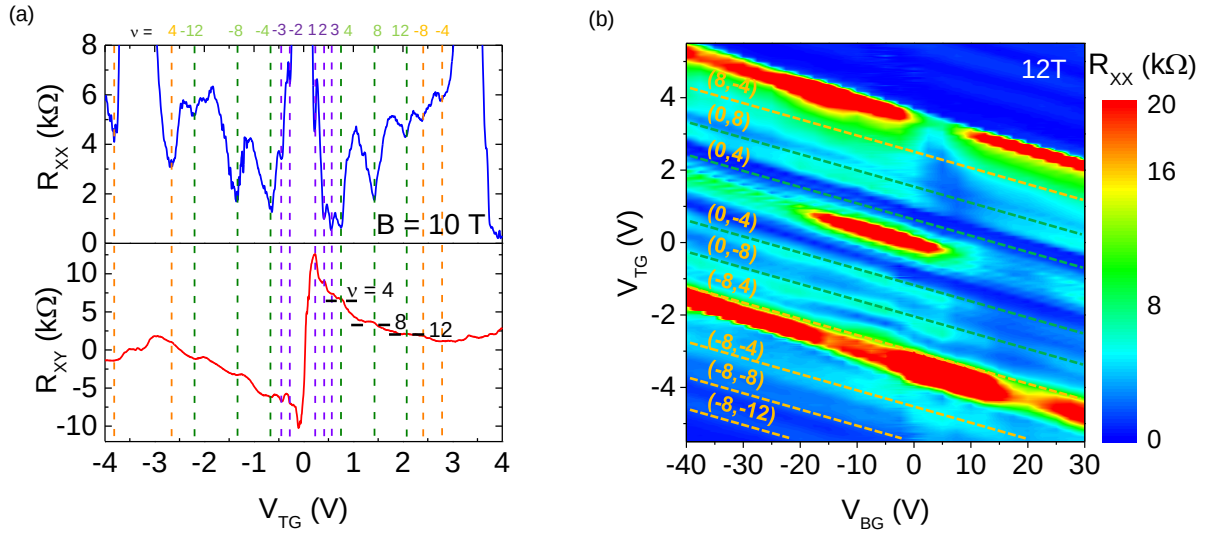

Figure 4.12 (a) R_{xx} (top panel) and R_{xy} (bottom panel) vs V_{TG} measured at B = 12 T, and T = 1.5 K in an STA bilayer graphene with θ = 0.97°. The n values are marked for each QHS. The QHSs with n = ± 4, 8, 12 and s = 0 (s = ± 8) are marked in green (orange). The QHSs with n = ± 1, 2, 3 are marked in purple. (b) Contour plot of R_{xx} as function of V_{BG} and V_{TG} at $B_\perp$ = 12 T, and T = 1.5 K. The QHSs with n = ± 4, 8, 12 and s = 0 (s = ± 8) are marked in green (orange).

The energy spectrum of a 2D electron system subject to a spatially periodic potential and $B_\perp$ have a fractal structure known as the Hofstadter butterfly, characterized by two topological integers: ν, representing the Hall conductivity in units of e^2/h, and s, the index of sub-band filling [88-91]. Gaps in the energy spectrum are observed when the density n/n_0 and the magnetic flux per moiré unit cell ($\phi \equiv BA$) satisfy the following Diophantine equation, where $\phi_0 = h/e$ is the quantum of magnetic flux:

$$\frac{n}{n_0} = \nu\frac{\phi}{\phi_0} + s \tag{4.1}$$

For s = 0, the integer ν reverts to the number of electrons per flux quanta, or LL filling factor. Conversely, with the limitation of small $B_\perp$, the integer s is the moiré band filling factor.

Figure 4.13 and 4.14 are the examples of Hofstadter butterfly energy spectrum at twist angle of 0.7° and 0.97°. In both figures, we measure R_{xx} as a function of V_{TG} and $B_{\perp}$ and convert V_{TG} and $B_{\perp}$ into n/n_0 and ϕ/ϕ_0.

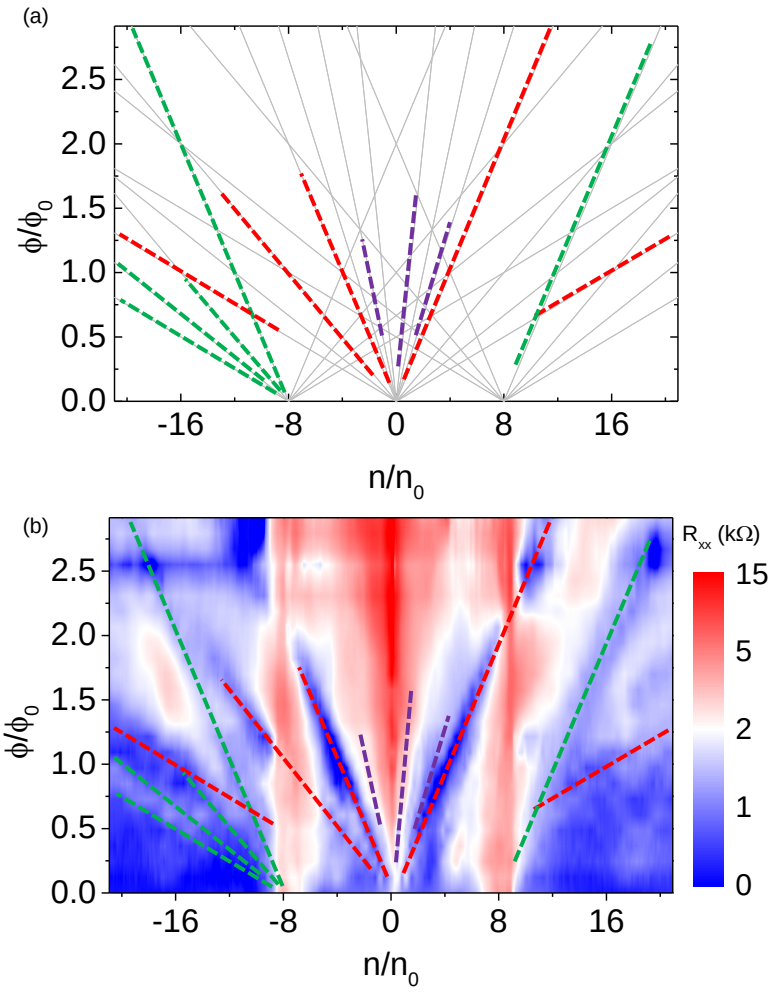

Figure 4.13 (a) LL fan diagram constructed using the Diophantine equation. The red (green) lines represent QHSs observed experimentally in panel (b) at n = ± 4, 8, 12 and $s = 0$ ($s = \pm 8$). The purple lines represent broken-symmetry QHSs at n = ± 1, 2, 3 and $s = 0$ (b) Contour plot of R_{xx} as a function of ϕ/ϕ_0 and n/n_0 in the sample with $\theta = 0.7°$. Dashed-lines emphasize the development of QHSs. The data are measured at $T = 1.5$ K up to $B = 14$ T, and at $T = 5$ K for B-fields from 15 T to 34.5 T.

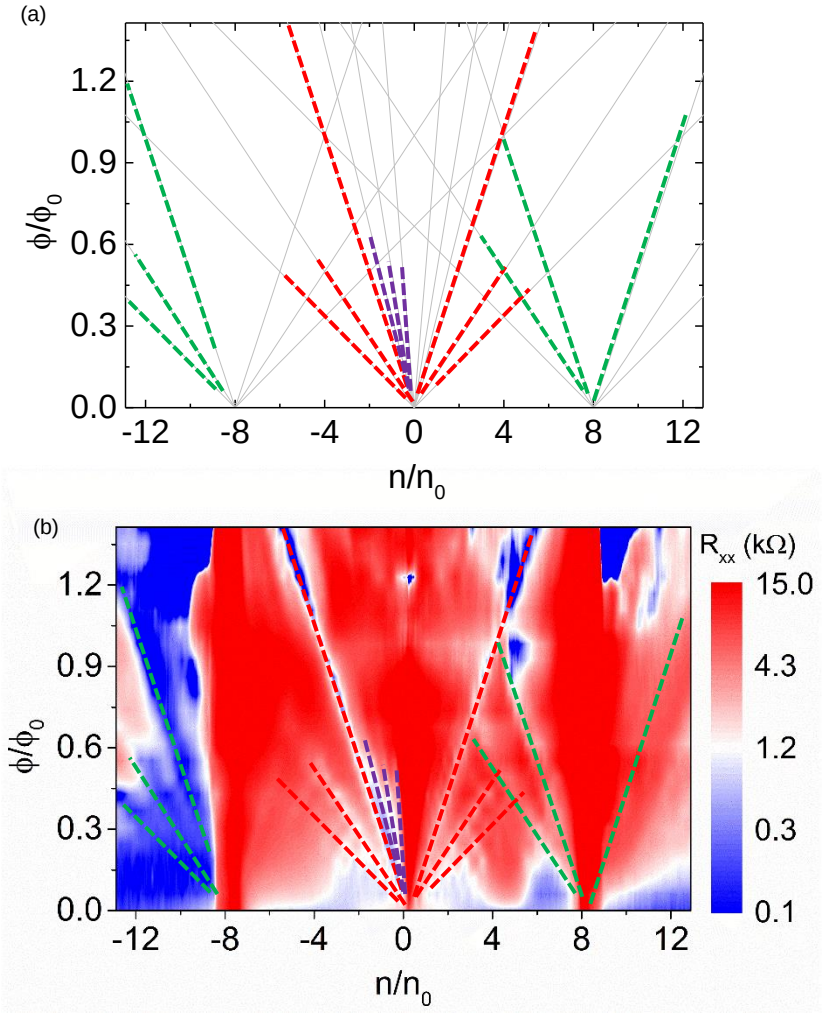

Figure 4.14 (a) LL fan diagram constructed using the Diophantine equation. The red (green) lines represent QHSs observed experimentally in panel (b) at n = ± 4, 8, 12 and $s = 0$ ($s = \pm 8$). The purple lines represent broken-symmetry QHSs at n = ± 1, 2, 3 and $s = 0$. (b) Contour plot of R_{xx} as a function of ϕ/ϕ_0 and n/n_0 in the sample with $\theta = 0.97°$. Dashed lines emphasize the development of QHSs. The data are measured at $T = 1.5$ K up to $B = 14$ T, and at $T = 5$ K for B-fields from 15 T to 34.5 T.

A representative subset of the QHSs that satisfy equation (4.1) are shown in the figure 4.13(a) and 4.14(a) for samples with 0.7° and 0.97°, respectively, and corresponding contour plots of R_{xx} vs normalized density n/n_0 and flux ϕ/ϕ_0 are shown in figure 4.13(b) and 4.14(b). The set of topological indices (ν, s) matching the experimental data is the following. For $s = 0$ and $s = \pm 8$, QHSs are observed at $\nu = \pm 4$. For $s = 0$, developing QHSs are observed at $\nu = \pm 1, \pm 2$, and ± 3. The observation of QHSs at ν values that are multiples of four is very similar to the QHSs sequence of Bernal stacked bilayer graphene, in which orbital LLs have a four-fold, spin and valley degeneracy. On the other hand, the developing QHSs at ν = 1-3 break the spin and valley degeneracy, and these QHSs can only be stabilized by interactions. This observation is consistent with electron-electron interactions dominating the transport properties of STA bilayer graphene at $B = 0$ T.

4.7 NON-LOCAL RESISTANCE MEASUREMENT IN STA BILAYER GRAPHENE

In STA bilayer graphene devices, the moiré crystal can produce a topological current since its moiré crystal structure breaks the inversion symmetry of the graphene, similarly to the graphene on hBN heterostructure devices [92]. To extend our knowledge in the STA bilayer, we measure a non-local resistance measurement in the STA bilayer graphene devices.

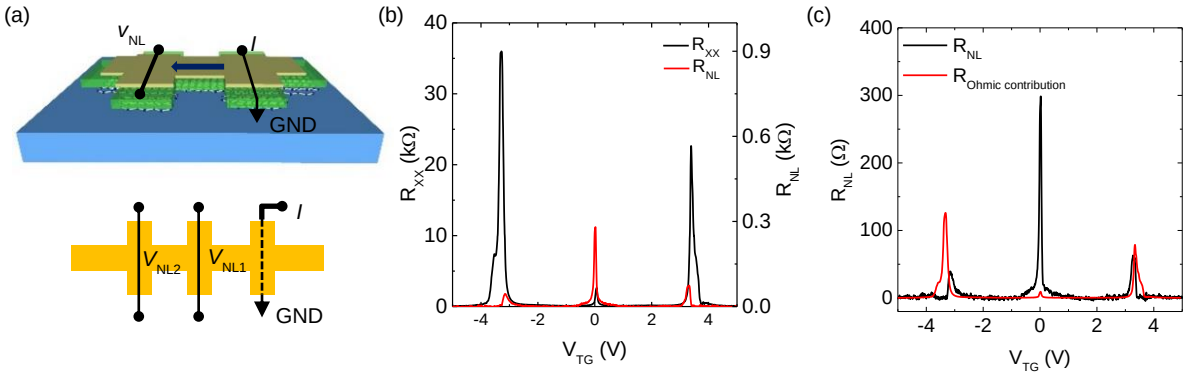

Figure 4.15 (a) Schematic and biasing scheme of STA bilayer graphene heterostructure. The biasing scheme expresses the set-up for a non-local resistance measurement. (b) R_{xx} (black line) and R_{NL} (red line) measured as a function of V_{TG} at 1.5 K. (c) R_{NL} and R_{Ohmic} as a function of V_{TG} at the neighboring voltage probes of V_{NL1}.

Figure 4.15(a) shows a device schematic and biasing scheme of the non-local measurement in STA bilayer graphene device. As shown in the figure, a charge current (I) flows in a parallel direction to the voltage probe and detects voltage drop across the pair (V_{NL}) of contacts. The non-local resistance (R_{NL}) is defined as $R_{NL} = V_{NL}/I$. Figure 4.15(b) shows a non-local measurement data in 0.97° twist angle bilayer graphene sample. In the figure, four-point resistance (left axis) is measured as a function of V_{TG} and compared to the non-local resistance (right axis) as a function of V_{TG} at 1.5 K. As shown in figure 4.15(c), we observe a significant non-local Dirac resistance (black trace) where the resistance shows orders of magnitude higher than the Ohmic contribution (R_{Ohmic}) derived by van der Pauw relation, $R_{NL} \sim \rho_{xx} \exp(-\pi L/w)$, where L is the distance between current path and voltage probes, and w is width of the device. Significantly high R_{NL} without the magnetic field applied in the device can be a result of topological current from moiré crystal structures.

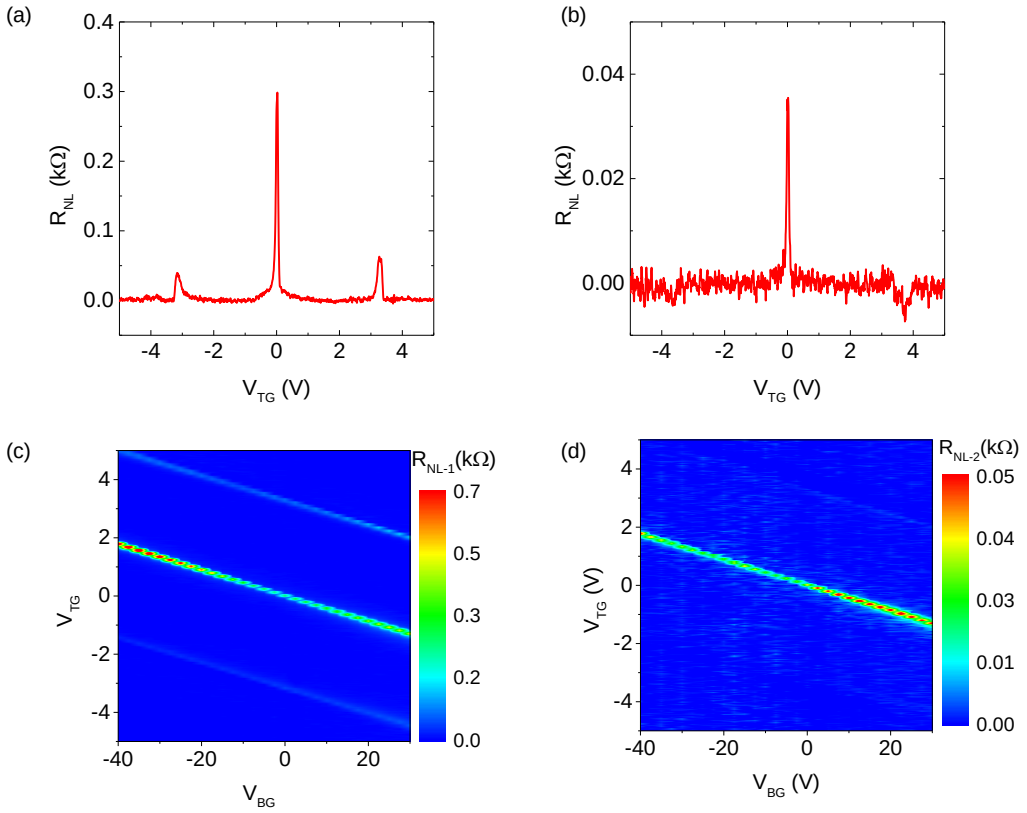

Figure 4.16 Non-local resistance measurement in an STA bilayer graphene with θ = 0.97°. (a, b) R_{NL} vs V_{TG} while V_{BG} is grounded at T = 1.5 K. (c, d) contour plot of R_{NL} as a function of V_{TG} and V_{BG}. Panel (a, c) are resistance and contour plot measured at the nearest neighboring voltage probes, and panel (b, d) are the next neighboring voltage probes.

To further validate the evidence of the topological current in our system, we investigate the device and measure R_{NL} by inducing E-filed in dual-gated system. As shown in the figure 4.15(a, b), two R_{NL} peak resistances at charge neutralities show a clear channel length dependence, where we can derive the relaxation length (ξ) based on relation, $R_{NL} \propto \exp(-L/\xi)$. As a result, we derive ξ~1 μm. Using equation 4.2, we find hall conductivity of $\sigma_{xy} = 0.6$ mS.

$$R_{NL} = \left(\frac{w}{2\xi}\right)(\sigma_{xy}{}^{\nu})^2(\rho_{xx})^3\exp\left(-\frac{L}{\xi}\right) \quad (4.2)$$

4.8 SUMMARY

In summary, we demonstrate controlled moiré crystals with long wavelengths in STA bilayer graphene and probe the electronic properties by SPM and magneto-transport. The data reveal pseudo-gaps that open at neutrality and ± 8 electrons per moiré BZ, which are robust with respect to an applied transverse electric field and are likely stabilized by electron-electron interaction. In high magnetic fields, we observe a Hofstadter butterfly in the energy spectrum and broken symmetry states in the lowest LL. Additionally, we observe topological current in STA bilayer graphene by breaking inversion symmetry in moiré crystal structure.

Chapter 5: Twist-Dependent Resonant Tunneling in WSe_2-hBN-WSe_2 Heterostructures

We investigate interlayer tunneling in heterostructures consisting of two WSe_2 monolayers with controlled rotational alignment, separated by hBN. In samples where two WSe_2 monolayers are rotationally aligned, we observe resonant tunneling, manifested by a large conductance and NDR in the vicinity of zero interlayer bias, which stem from energy and momentum conserving tunneling. Because the strong spin-orbit coupling splits the valence band and leads to coupled spin-valley degrees of freedom, the relative twist between the two WSe_2 monolayers allows us to probe the role of spin-valley conservation in tunneling. In heterostructures where the two WSe_2 monolayers have a relative 180°-twist, such that the BZ of one layer is aligned with the time-reversed BZ of the opposite layer, the resonant tunneling between the layers is suppressed. These findings suggest that in addition to energy and momentum, the spin-valley degree of freedom is also conserved in vertical transport. [4]

[4] This work has been submitted and just accepted as: K. Kim, N. Prasad, H.C.P. Movva, G.W. Burg, Y. Wang, S. Larentis, T. Taniguchi, K. Watanabe, L.F. Register, and E. Tutuc, "Spin-conserving resonant tunneling in twist-controlled WSe_2-hBN-WSe_2 heterostructures," *Nano Letters*, doi:10.1021/acs.nanolett.8b02770. The dissertator, K. Kim, fabricated heterostructures devices, performed the electrical characterization, and contributed to data analysis and writing the paper.

5.1 INTRODUCTION

An attribute essential to semiconductor heterostructures' device functionality, but which remains largely unexplored for most van der Waals heterostructures, is the coupling and transport along the vertical axis. Interlayer, momentum-conserving tunneling in rotationally aligned van der Waals heterostructures may enable novel device functionality for beyond CMOS low-power, high-speed logic [4, 5], while resonant tunneling in double layers separated by a tunnel barrier provides a direct measurement of interlayer coupling and the quantum state life-time [93]. Recent progress in realization of twist-controlled van der Waals heterostructures [12-15, 17] with precise rotational alignment between 2D layers opens interesting avenues to probe new physics and device functionalities. NDR characteristics associated with momentum conserving tunneling have been reported in graphene-based double layers, such as rotationally aligned double monolayer [8, 94], and double bilayer graphene [10, 69] separated by hBN, or double bilayer graphene separated by WSe_2 tunnel barrier [11]. Theoretical considerations dictate that TMD double layers can exhibit gate-tunable NDR with very narrow resonances due to the increase in TDOS [95].

WSe_2 is a prototypical TMD with a honeycomb lattice, which can be isolated down to monolayer using micro-mechanical exfoliation and has high intrinsic mobility at low temperatures [96]. In the monolayer limit, the band extrema are located at the corners (*K* point) of the hexagonal BZ with a band-gap of approximately 2.0 eV [97, 98]. The strong spin-orbit coupling leads to a large valence band splitting of approximately 0.5 eV, with each of the valence band at one band extremum possessing the opposite spin [99, 100]. We demonstrate resonant tunneling in dual-gated, rotationally aligned double monolayer WSe_2

heterostructures separated by an IL hBN dielectric, which reveals narrow tunneling resonances with intrinsic broadening of 1-3 meV at low temperatures. Remarkably, the resonant tunneling is present (absent) in samples where the relative twist between the two WSe_2 monolayers is an even (odd) multiple of 60°, a finding which can only be explained by the conservation of the spin-valley degree of freedom in tunneling.

5.2 DEVICE FABRICATION

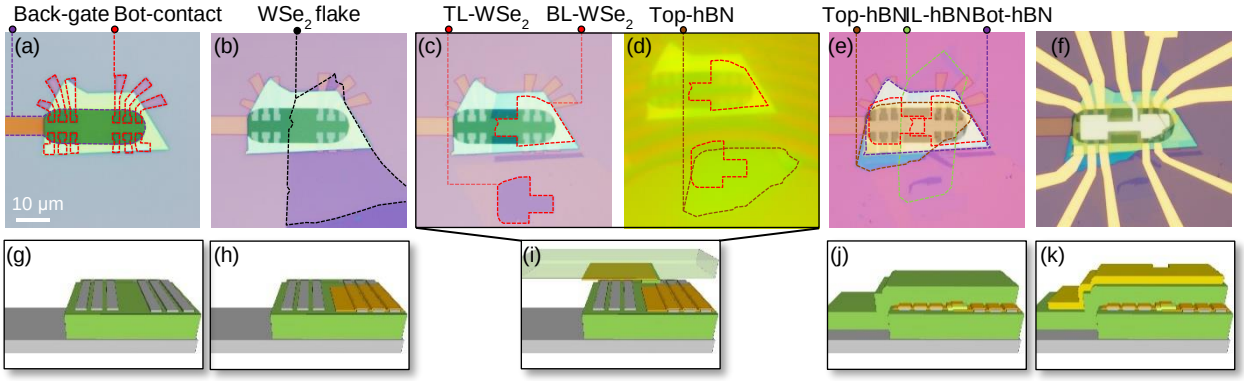

Figure 5.1 Optical micrographs (a-f) and schematics (g-k) of the detailed fabrication process of a typical WSe_2-hBN-WSe_2 heterostructure sample. Panel (a-f) are at the same magnification.

Figure 5.1 describes the fabrication process flow of a dual-gated WSe_2-hBN-WSe_2 heterostructure comprising two rotationally aligned monolayer WSe_2 electrodes, separated by an IL hBN tunnel barrier. Figure 5.1(a-f) shows the optical micrographs and Figure 5.1(g-k) the corresponding schematics during the fabrication process. Using a layer transfer method [54, 101], we first transfer a bottom-gate hBN (B hBN) flake, which serves as the bottom-gate dielectric, onto a pre-defined metal local back-gate patterns using EBL, electron-beam metal evaporation of Cr/Pt (2 nm/8 nm), and lift-off. After the B hBN is transferred, bottom electrodes of Cr/Pt (3 nm/12 nm) are patterned using EBL and electron-

beam metal evaporation [Figure 5.2(a, g)], which serve as *p*-type contacts to the WSe_2 layers [102]. On a separate SiO_2/Si substrate, monolayer WSe_2 flakes are exfoliated and confirmed using Raman and PL spectroscopy. A suitable monolayer WSe_2 flake is chosen and transferred onto the Pt contacts meant for the bottom WSe_2 electrode in such a way that only a partial region of the flake is on the contacts, as shown in figure 5.1(b, h). We note here that a relatively large area monolayer WSe_2 flake is chosen for the ease of trimming in order to obtain both the bottom (BL) and top layer (TL) WSe_2 electrodes from a single crystal grain. The monolayer WSe_2 flake is then sectioned into the individual TL and BL WSe_2 electrodes using EBL followed by etching in a CHF_3 plasma [figure 5.1(c)]. Subsequently, we first pick-up a top-gate hBN (T hBN) flake from a separate SiO_2/Si substrate using a modified half hemispherical PDMS stamp, coated with an adhesive PPC layer, and then selectively pick-up only the TL WSe_2 [Figure 5.1(d)], followed by a thin IL hBN flake, and place the resulting T hBN-TL WSe_2-IL hBN stack on the BL WSe_2-B hBN substrate after precisely controlling the rotational alignment between the TL and BL WSe_2 at either 0° or 180° [Figure 5.1(e, j)]. A Pd top-gate is finally patterned to cover both the top and bottom WSe_2 flakes. To complete the device fabrication, we perform two final EBL, electron-beam evaporation, and lift-off steps to pattern the Cr/Pd/Au (3 nm/25 nm/40 nm) metal contacts and bond pads [Figure 5.1(f, k)]. To remove polymer residues introduced during the transfer process, we perform the UHV (1×10^{-9} Torr) anneal at 350°C for 2 hours after each transfer step.

5.2.1 Half-cut hemispherical handle substrate

To improve the accuracy of an angle alignment during fabrication, a transfer technique, which involves a simple refinement of the hemispherical handle stamp into a half-cut hemispherical stamp, is further developed. The modification shows a significant improvement of the selective pick-up accuracy of the two sectioned WSe_2 flakes, which can advance the control of the rotational alignment between the two monolayer WSe_2 flakes when obtaining two flakes from a large single crystal grain.

In view of the typical monolayer flake size being only 10-50 μm long along an edge, selectively picking-up only a portion of this moderately sized flake becomes cumbersome with conventional pick-and-place techniques [101]. While the hemispherical handle stamp improves the spatial resolution of pick-up by controlling the contact area, manipulating the radius of the contact area is limited laterally to ±10 μm due to the PPC heat release polymer being prone to deformation and wrinkling at the contact edge, apparent in the form of Newton's rings at the edges in Figure 5.2(a).

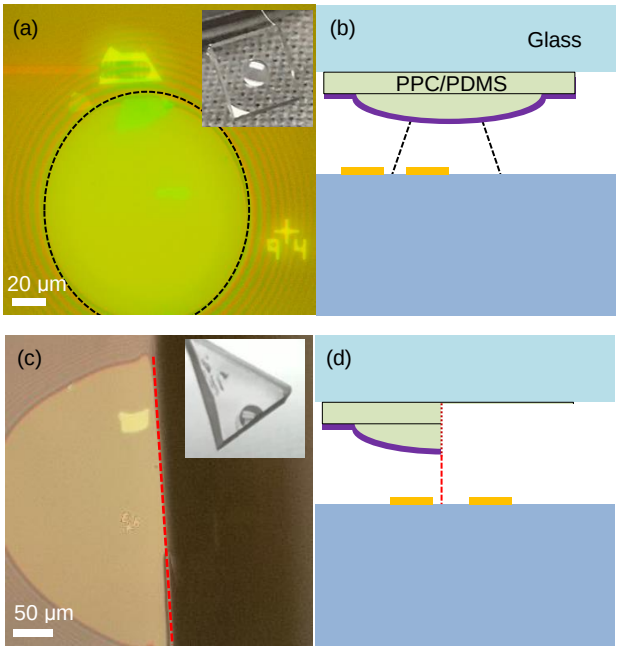

Figure 5.2. (a) Optical micrograph and (b) cross section schematic of a typical hBN and WSe_2 layer pick-up using a hemispherical handle stamp. The black dashed line in panel (a) indicates the border of the contact area during pick-up. (c) Optical micrograph and (b) cross section schematic of a half-cut hemispherical handle stamp during the pick-up process. The red dashed line in panel (c) indicates the contact area during pick-up. The insets of panels (a) and (c) are optical micrographs of the stamps showing the hemispherical portions. The edge of the PDMS stamp is ~ 5 mm long.

Figure 5.2(c-d) show the optical micrograph and cross section schematic of the half-cut hemispherical handle stamp, respectively, shown for an example selective flake (hBN) pick-up process. By creating a sharp, straight edge midway through the hemisphere, the lateral resolution of the contact can be controlled to a much higher accuracy. This is evident in figure 5.2(c), where Newton's rings are absent along the straight edge. The selective WSe_2 pick-up is done by aligning the straight edge with the separation between the two etched WSe_2 flakes and picking-up only one without having to worry about the PPC

deforming onto the adjacent second flake. Selective pick-up of flakes separated by as little as 10 μm is possible due to the half-cut hemispherical handle stamp.

5.2.2 Accessing large area WSe_2 monolayer using Au-mediated exfoliation

Another way of improving rotationally aligned heterostructure fabrication process is simply to obtain a large area single crystalline grain flake. A large single grain monolayer WSe_2 flake simplifies the selective pick-up process by easing constraints on the lateral pick-up spatial resolution. Typical monolayer WSe_2 flakes obtained from conventional scotch-tape micro-mechanical exfoliation techniques range between 10-50 μm in size. A recent Au-mediated exfoliation technique introduced by Desai *et al.* [103] provides a way to obtain much larger flakes. The following discusses the influence of Au deposition rate on the quality of flakes obtained using this method.

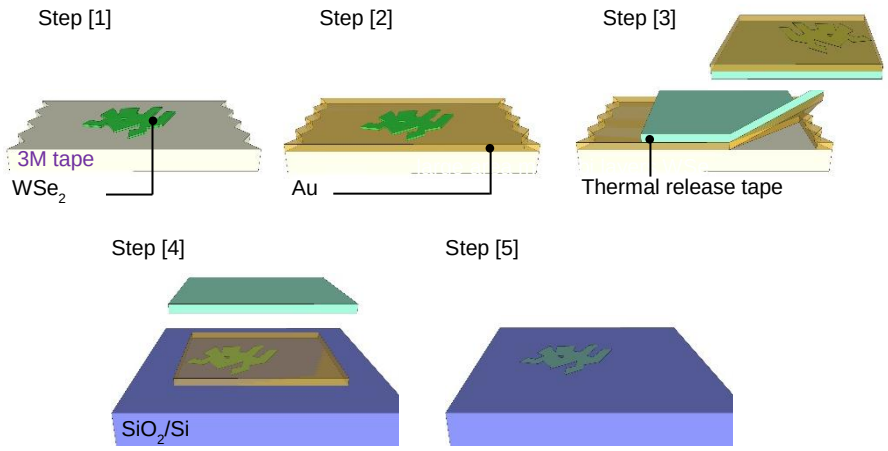

Figure 5.3. Schematic of Au-mediated exfoliation processes.

Figure 5.3 shows a schematic process flow of the Au-mediated exfoliation technique. In step [1], a bulk WSe_2 crystal is exfoliated on a tape with strong adhesion. In step [2], Au is deposited on the WSe_2 crystals on the tape using electron-beam evaporation

and in step [3], the Au layer is peeled off using a thermal release tape. The strong affinity between Au and the top layer of WSe_2 causes large monolayer flakes to attach themselves to Au and detach from the bulk WSe_2 crystals on the tape. In step [4], the Au/monolayer WSe_2 film is released on an SiO_2/Si substrate by heating the thermal release tape to 90°C. Finally, in step [5], the top Au is removed in an Au-etchant of potassium iodide and iodine.

Figure 5.4 Optical micrographs of the monolayer and bilayer WSe_2 flakes obtained by Au-mediated exfoliation.

	Initial Au deposition rate	Average Au deposition rate
Trial #1	0.1 Å/s	0.5Å/s
Trial #2	0.5 Å/s	1 Å/s
Trial #3	0.5 ~ 0.8 Å/s	1.5 Å/s

Table 5.1 Table showing three different trials of Au-deposition rates using electron-beam evaporation on the bulk WSe_2 crystal in figure 5.3 step [2].

Figure 5.4 shows the optical micrographs of the monolayer WSe_2 flakes on an SiO_2/Si substrate obtained using the steps described in figure 5.3. The Au deposition rate was found to affect the quality of the monolayer WSe_2 flakes. Table 5.1 shows three trials of Au deposition at different rates in electron-beam evaporation. The Au is deposited at a

base pressure of 5.5×10^{-6} Torr and the initial deposition rate is controlled by soaking the Au at different electron-beam powers prior to opening the shutter for deposition. All the other steps outlined in figure 5.3 remain the same for the three trials except for the Au deposition rate.

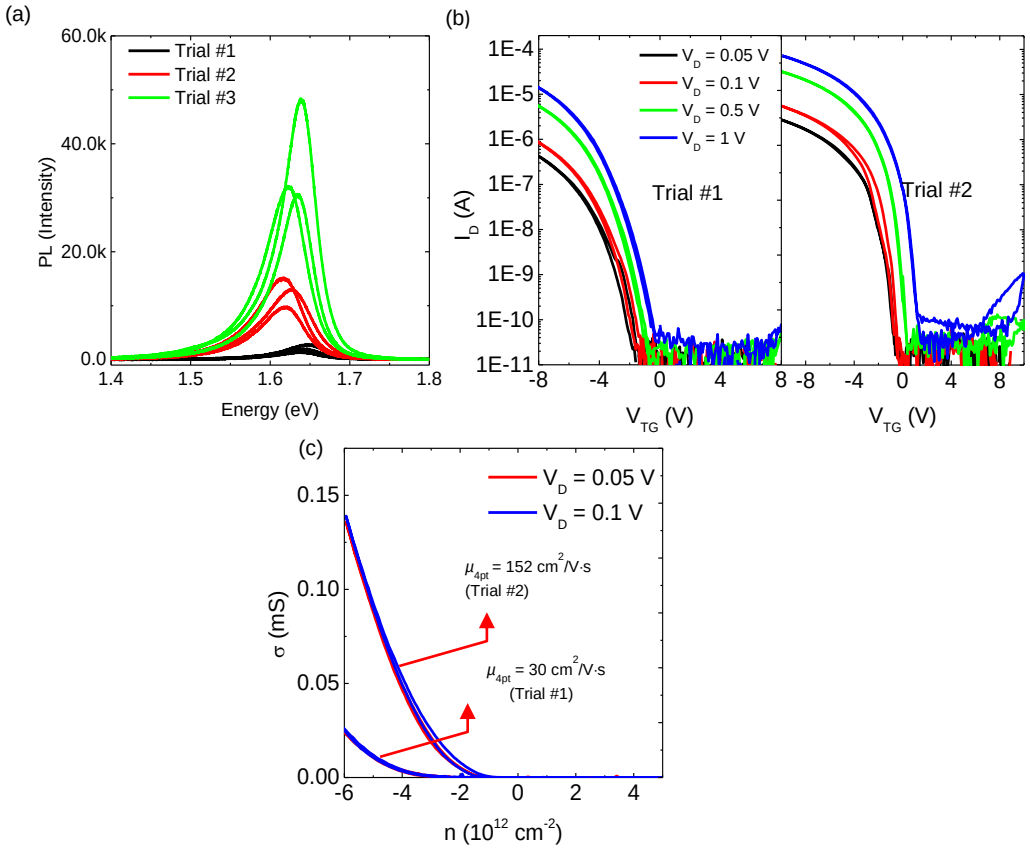

Figure 5.5 (a) PL spectra of the exfoliated large area monolayer WSe_2 flakes obtained from the trials of figure 5.3 panel (b). (b) ID vs VTG of two hBN encapsulated WSe_2 FETs, using WSe_2 monolayers from Trial #1 and #2. (c) Four-point conductance and µ4pt corresponding to panel (b) data.

Figure 5.5(a) shows the PL spectra for monolayer flakes from the three trials. A clear difference in the PL counts is observed for the three trials with the higher deposition rate trials showing higher PL intensities. Monolayer WSe_2 flakes obtained with an Au

evaporation rate of 0.5 to 0.8 Å/s show an order of magnitude higher PL intensity than when Au is deposited at 0.1 Å/s. To further investigate the quality of WSe_2 layers, we fabricate two sets of hBN encapsulated FETs using WSe_2 flakes from Trial #1 and #2. Figure 5.5(b) shows the drain current (I_D) vs V_{TG} for the WSe_2 flakes from the two trials. Both the data show *p*-type conduction. In both panels, we use Cr/Pt (3 nm/12 nm) electrodes on hBN as bottom contacts, and 19 nm and 28 nm thick hBN flakes as top-gate dielectrics, which correspond to top-gate capacitances of 140 nF/cm^2 and 95 nF/cm^2, respectively. Figure 5.5(c) shows the normalized four-point conductance vs density for the two devices in figure 5.5(b). We extract the corresponding four-point field effect mobility (μ_{4pt}) values of μ_{4pt} = 152 cm^2/Vs for Trial #2 in comparison to μ_{4pt} = 30 cm^2/Vs for Trial #1. Approximately five times higher value of μ_{4pt} for Trial #2 vs Trial #1 confirms the higher quality of WSe_2 with a higher Au deposition rate. In conclusion, the Au deposition rate during deposition on bulk WSe_2 can significantly affect the quality of the resulting monolayer WSe_2.

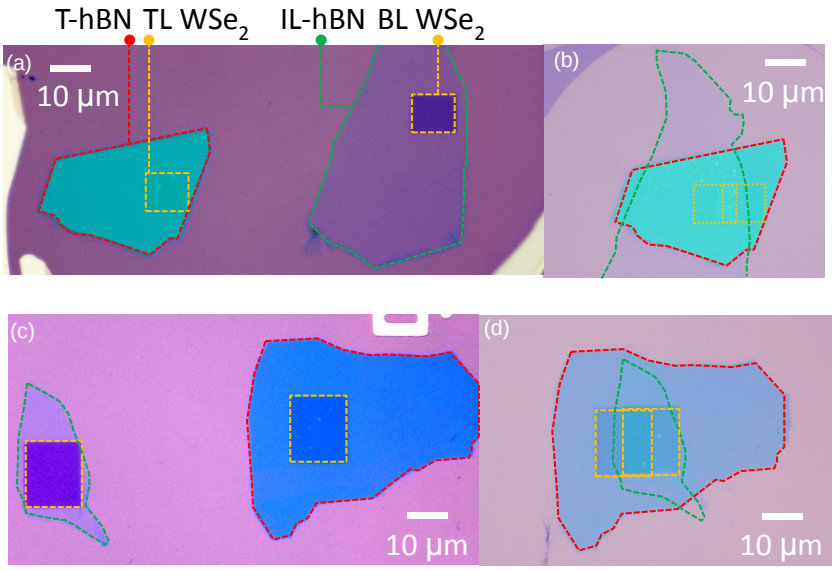

Figure 5.6 Optical micrographs of layer stack-up process in WSe_2-hBN-WSe_2 heterostructure using half-hemispherical handle substrate and Au-mediated exfoliation.

Figure 5.6(a, c) show optical micrographs describing fabrication of WSe_2-hBN-WSe_2 heterostructure using half-hemispherical handle substrate and large area WSe_2 obtained by Au-mediated exfoliation. Figure 5.6(a, c) are optical micrographs after landing T and IL hBN on pre-trimmed WSe_2 layers by EBL followed by CHF_3+O_2 plasma, and figure 5.6(b, d) are the optical micrographs of completed WSe_2-hBN-WSe_2 heterostructures. Panel (a, b) and panel (c, d) are the heterostructures of Device #2 and #4 in table 5.2, respectively.

5.3 Realization of rotationally aligned WSe_2-hBN-WSe_2 van der Waals heterostructures

Because monolayer WSe_2 band extrema are located at the *K* point, momentum-conserving tunneling occurs if the relative twist between the two WSe_2 monolayers is a

multiple of 60°. If the relative twist is an even multiple of 60° (e.g. 0°), the *K* point and its time-reversed partner (*K'*) of the two monolayers are aligned in momentum space. Conversely, if the relative twist is an odd multiple of 60° (e.g. 180°), the *K* (*K'*) point of one layer is aligned with the time reversed partner *K'* (*K*) of the opposite layer. We employ temperature dependent, four-point current-voltage measurements to probe the intrinsic tunneling characteristics at zero and high magnetic fields, and investigate the impact of energy, momentum, and spin conservation.

Samples	Twist Angle	T hBN Thickness (nm)	B hBN Thickness (nm)	IL hBN # of layers	C_{TG} (nF/cm^2)	C_{BG} (nF/cm^2)	C_{IL} (μF/cm^2)	Reference
Device #1	0°	23.3	60.3	3	114	44	2.30	WW (3) [Tape-exfoliated]
Device #2	0°	23.0	13.0	4	115	204	1.80	WW (23) [Au-exfoliated]
Device #3	0°	10.4	8.2	6	255	324	1.31	WW (24) [Au-exfoliated]
Device #4	0°	28	27	5	95	98	1.53	WW (18) [Au-exfoliated]
Device #5	180°	23.8	29.7	7	112	89	1.15	WW (9) [Tape-exfoliated]
Device #6	180°	10.5	20	6	253	133	1.31	WW (12) [Tape-exfoliated]

Table 5.2 Specifications of rotationally aligned WSe_2-hBN-WSe_2 devices.

Table 5.2 presents the detailed information of all devices that are fabricated and analyzed in this Chapter.

5.3.1 Interlayer tunneling current-voltage characteristics

The devices are characterized at negative V_{TG} and V_{BG} in order to populate both the WSe_2 layers with holes. The bottom Pt contacts in combination with negative V_{TG} and V_{BG} ensure Ohmic *p*-type contacts to WSe_2 [102]. The intrinsic tunneling characteristics, free of contact resistance effects can be studied, thanks to multiple contacts on each layer.

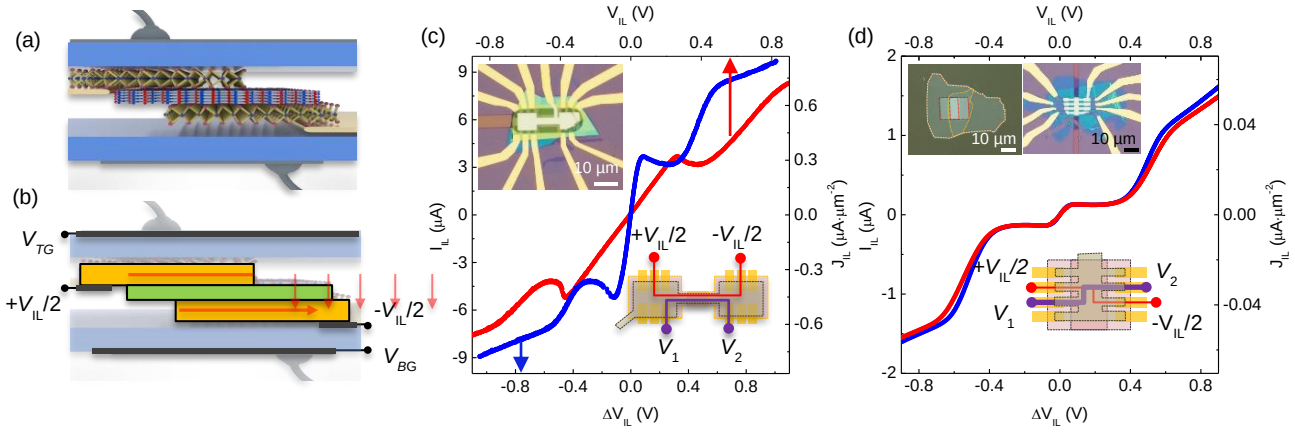

Figure 5.7 (a) Cross sectional schematic of the final device, and (b) biasing scheme used for the two-point interlayer tunneling current measurement. Two-point I_{IL} vs V_{IL} (top axis), and four-point I_{IL} vs ΔV_{IL} (bottom axis) for (c) Device #1 and (d) Device #2 at room temperature. The right axes in panels (c, d) show I_{IL} normalized to the TL and BL WSe_2 overlap area. Insets of (c, e): Biasing scheme used for the four-point measurements of (c) Device #1 and (d) Device #2. The four-point interlayer bias is $\Delta V_{IL} = V_1 - V_2$.

Figure 5.7(a, b) show cross sectional schematic of the device and its biasing scheme. The devices are biased by applying an interlayer voltage (V_{IL}) split symmetrically across the two layers, i.e. $+V_{IL}/2$ on the top-layer and $-V_{IL}/2$ on the bottom layer, and the interlayer bias (ΔV_{IL}) is measured using additional contacts on each layer. Figure 5.7(c)

shows the room temperature two-point (four-point) interlayer tunneling current, I_{IL} vs V_{IL} (ΔV_{IL}), with three layer IL hBN, where the two WSe_2 layers are aligned with respect to each other, i.e. 0º twist. A salient feature of figure 5.7(c) data is the NDR characteristic on either side of $V_{IL} = 0$, or $\Delta V_{IL} = 0$, the telltale sign of resonant tunneling between two 2D carrier systems.

An evident difference between the two-point and four-point data in figure 5.7(d) is the apparent stretching of the two-point I_{IL} vs V_{IL} along the V_{IL} axis in comparison to the four-point I_{IL} vs ΔV_{IL}. This is due to the effect of contacts, which drop a substantial portion of the applied V_{IL}, resulting in an effectively reduced ΔV_{IL}. Figure 5.7(d) shows a similar set of data for four atomic layers of IL hBN with a different device geometry described in the inset schematic, which shows a reduced NDR around $V_{IL} = 0$, as expected for a thicker IL hBN. The difference between the two-point and the four-point data is smaller in figure 5.7(c), owing to a larger interlayer tunneling resistance compared to the contact resistance. The data in figure 5.7(c, d) also show an inflexion in I_{IL} at $\Delta V_{IL} \sim \pm 0.5$ V. We attribute this to the tunneling contribution from the second valence band of WSe_2.

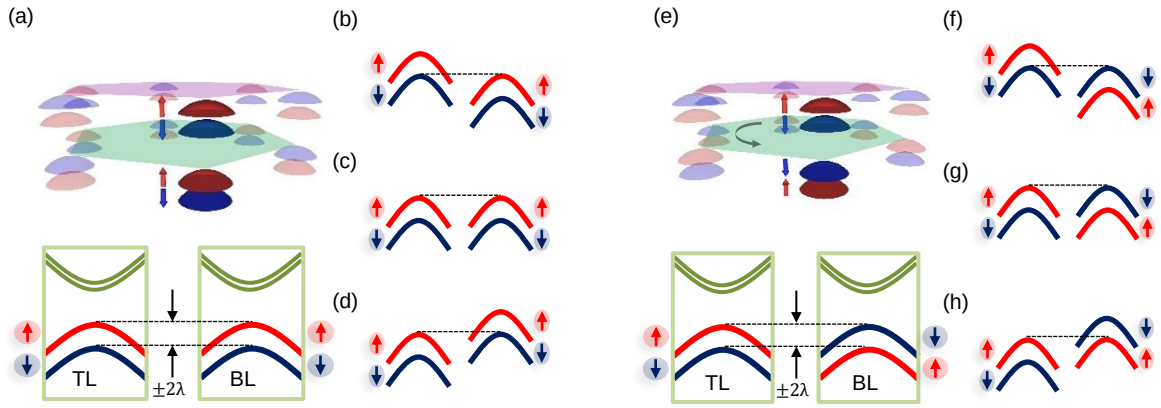

Figure 5.8 (a, e) are band alignment schematics of the two WSe_2 layers with 0º and 180º twist, respectively. (b-d) and (f-h) are corresponding band alignments under an applied $\Delta V_{IL} = -2\lambda, 0, 2\lambda$.

Figure 5.8(a) shows a schematic of the valence bands in the two WSe_2 layers at 0º twist. The *K* and *K'* valleys in both layers are aligned in momentum space at $\Delta V_{IL} = 0$. Figure 5.8(b-d) show the band alignments under an applied $\Delta V_{IL} = 0, \pm 2\lambda$, where $2\lambda \approx 0.5$ V is the spin-orbit coupling induced band splitting at *K* point [99, 100]. It can be seen that at $\Delta V_{IL} \sim \pm 0.5$ V, the spin-up and spin-down valleys of opposite layers are aligned in momentum space at both *K* and *K'*, hinting at tunneling between the unlike spin bands as a possible origin for the I_{IL} vs ΔV_{IL} inflexion. Figure 5.8(e) shows a schematic of the valence bands in the two WSe_2 layers at 180º twist and Figures 5.8(f-h) show the band alignments under application of $\Delta V_{IL} = 0, \pm 2\lambda$. Here, in contrast to figures 5.8(a-d), the *K* and *K'* valleys in both layers are aligned in momentum space at $\Delta V_{IL} = \pm 0.5$ V, and the unlike spin bands in the opposite layers are aligned at $\Delta V_{IL} = 0$.

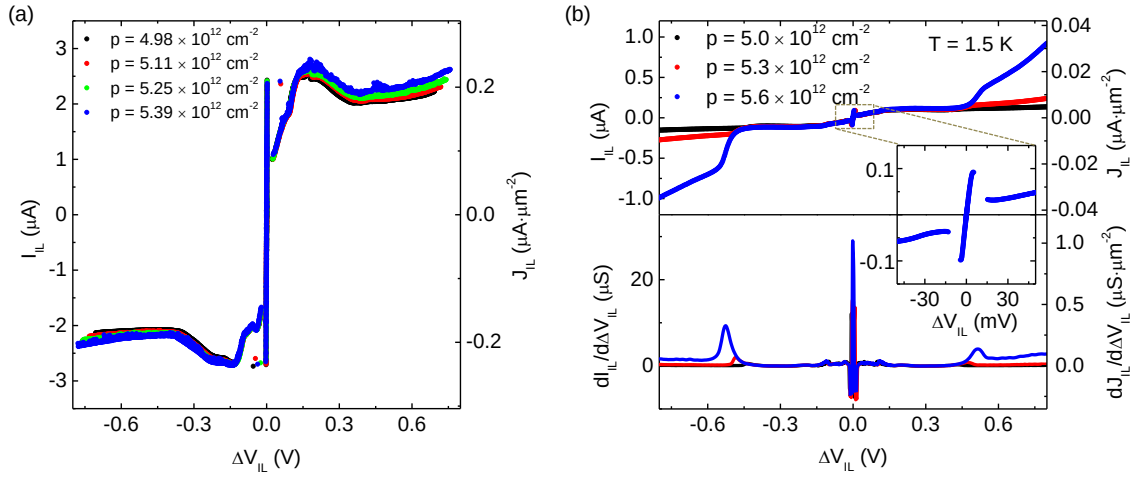

Figure 5.9 (a) I_{IL} vs ΔV_{IL} for Device #1 at $T = 1.5$ K measured at equal layer density values, from $p = 4.98\times10^{12}$ cm^{-2} to $p = 5.39\times10^{12}$ cm^{-2}. (b) I_{IL} vs ΔV_{IL} (top panel) and $dI_{IL}/d\Delta V_{IL}$ vs ΔV_{IL} (bottom panel) for Device#2 at $T = 1.5$ K measured at equal layer density values, from $p = 5.0\times10^{12}$ cm^{-2} to $p = 5.6\times10^{12}$ cm^{-2}. Inset: close-up of I_{IL} vs ΔV_{IL} at $p = 5.6\times10^{12}$ cm^{-2} near $\Delta V_{IL} = 0$ V.

Figure 5.9(a) shows I_{IL} vs ΔV_{IL} for Device #1 at $T = 1.5$ K and at four different biasing conditions chosen such that the hole densities (p) in the two WSe_2 layers are equal and range from $p = 4.98\times10^{12}$ cm^{-2} to $p = 5.39\times10^{12}$ cm^{-2}. All traces show clear NDR. Similarly to the figure 5.9(a), Figure 5.9(b) shows I_{IL} vs ΔV_{IL} and the corresponding differential conductance, $dI_{IL}/d\Delta V_{IL}$ vs ΔV_{IL} for Device #2 at $T = 1.5$ K and at three different biasing conditions chosen such that the p in the two WSe_2 layers are equal and range from $p = 5.0\times10^{12}$ cm^{-2} to $p = 5.6\times10^{12}$ cm^{-2}. All three traces also show a steep NDR and a corresponding sharp differential conductance peak with a narrow FWHM of 7 mV close to $\Delta V_{IL} = 0$; a close-up view of the I_{IL} vs ΔV_{IL} data at $p = 5.6\times10^{12}$ cm^{-2} is shown in the inset of figure 5.9(b). The discontinuity in the plot near $\Delta V_{IL} = 0$ can be explained by

the circuit instability caused by the larger external (contact and non-overlapped WSe_2 layer) resistance in series with a lower negative differential tunneling resistance, which prevents a measurement of I_{IL} in this regime. Further, all three traces in figure 5.9(b) show the I_{IL} inflexion, albeit, of varying intensity, which appears as a corresponding differential conductance peak at $\Delta V_{IL} \sim \pm 0.5$ V. In the following, we refer to the differential conductance peak at $\Delta V_{IL} = 0$ as the primary resonance, and at $\Delta V_{IL} \sim \pm 0.5$ V as the secondary resonances. The main different between the figure 5.9(a, b) are using different tunnel barrier thickness of 4 and 5 layers as indicate in Table 5.2.

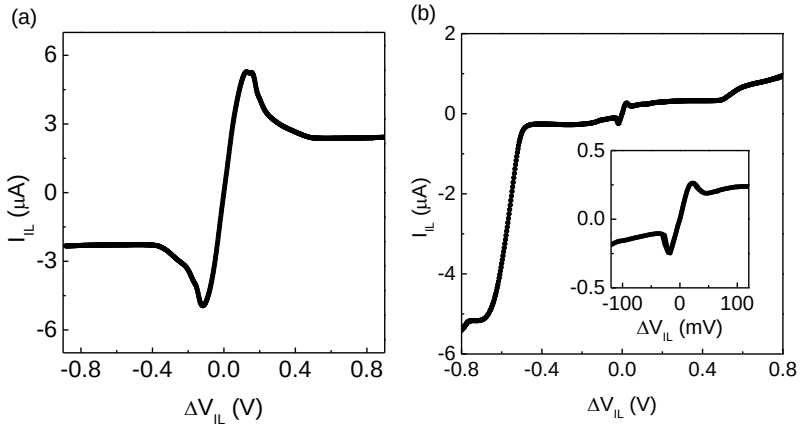

Figure 5.10 (a, b) are I_{IL} vs ΔV_{IL} for Device#3 and Device#4 at $T = 1.5$ K measured at equal layer density values of $p = 5.05\times10^{12}$ cm^{-2} and $p = 1.04\times10^{13}$ cm^{-2}, respectively. Inset: close-up of I_{IL} vs ΔV_{IL} near $\Delta V_{IL} = 0$.

Figure 5.10(a, b) are I_{IL} vs ΔV_{IL} plots of two additional samples with 0º twist that are listed in table 5.2 Device #3 and Device #4 which has similar device geometry of Device #1 and #2 described in figure 5.7(c, d) insets, respectively. Inset in figure 5.10(b) is the close-up view near zero interlayer bias. Both plots clearly show the NDR characteristics. For later analysis in this chapter, we focus more on Device #1 and #2.

5.3.2 Temperature dependence

To investigate the origin of the tunneling resonances, we perform temperature dependent measurements.

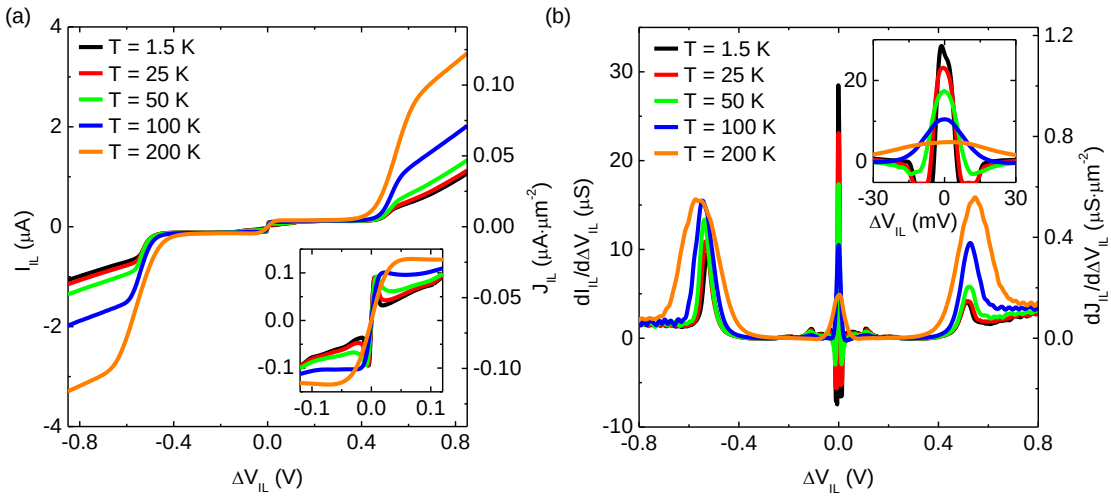

Figure 5.11 (a) I_{IL} vs ΔV_{IL} and (b) $dI_{IL}/d\Delta V_{IL}$ vs ΔV_{IL} as a function of varying temperature from $T = 1.5$ to 200 K. insets are close-up views of the corresponding panel data near $\Delta V_{IL} = 0$. The right axes of panels show I_{IL} and $dI_{IL}/d\Delta V_{IL}$ normalized to the TL and BL WSe_2 overlap area.

Figure 5.11(a, b) show I_{IL} vs ΔV_{IL} and the corresponding $dI_{IL}/d\Delta V_{IL}$ vs ΔV_{IL} data as a function of varying temperature at $p = 5.6\times10^{12}$ cm^{-2} in Device #2, and figure 5.12(a, b) shows I_{IL} vs ΔV_{IL} (top panel) and the corresponding $dI_{IL}/d\Delta V_{IL}$ vs ΔV_{IL} (bottom panel) data as a function of varying temperature at $p = 5.39\times10^{12}$ cm^{-2} in Device #1 in wide ΔV_{IL} range and near zero bias. Based on temperature dependence plots shown in both figures, two noteworthy observations of commonality are as follows. First, the NDR associated with the primary resonance becomes more prominent with decreasing temperature. Equivalently, the primary resonance peak becomes sharper and increases in conductance,

along with the neighboring dips which become deeper. Second, the inflexion associated with the secondary resonance and correspondingly, its amplitude decreases with decreasing temperature. The opposite temperature dependences of the primary resonance and secondary resonance suggest a difference in their mechanism of origin.

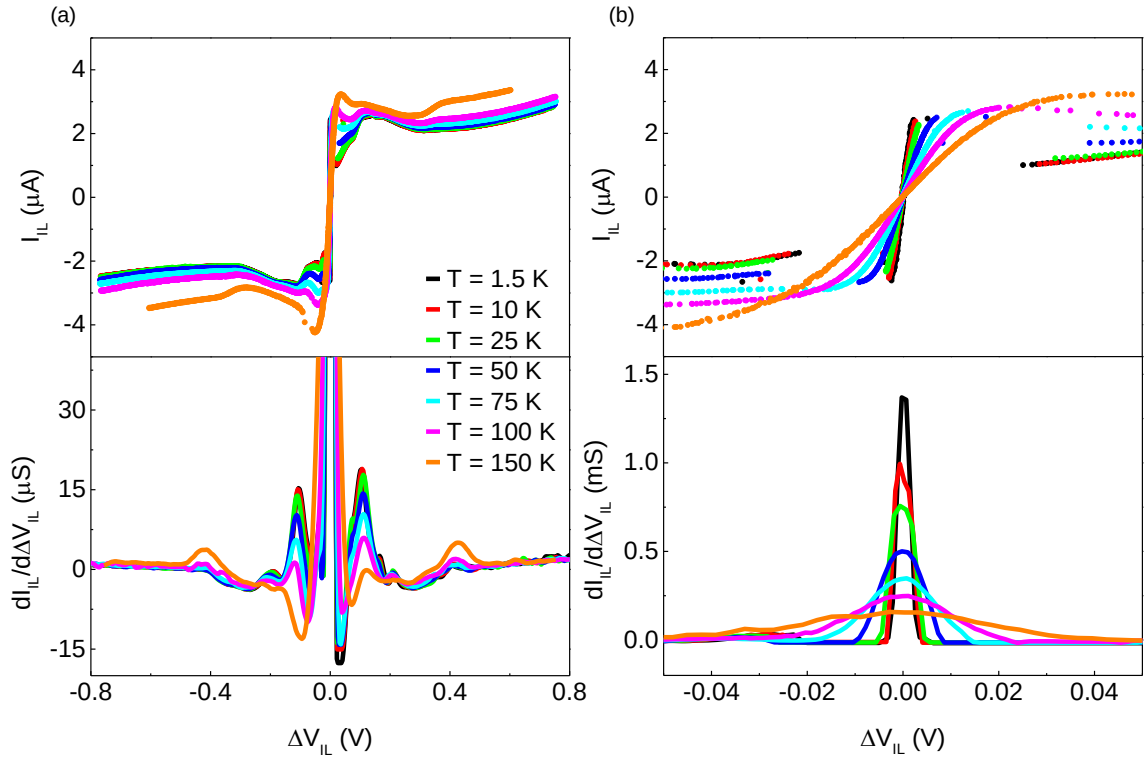

Figure 5.12 (a) I_{IL} vs ΔV_{IL} (top panel) and $dI_{IL}/d\Delta V_{IL}$ vs ΔV_{IL} (bottom panel) as a function of varying temperature from T = 1.5 to 150 K. (b) Close-up views of the corresponding panel (a) data near $\Delta V_{IL} = 0$.

5.3.3 Theoretical calculation of tunneling mechanism

In order to gain insight into the tunneling mechanisms at play in our devices, we model the interlayer current of the WSe_2-hBN-WSe_2 system using a perturbative

Hamiltonian approach. [11, 104, 105] The band structures of the top [$\epsilon_{\mathrm{T}}(\mathbf{k}, \sigma)$] and bottom [$\epsilon_{\mathrm{B}}(\mathbf{k}, \sigma)$] WSe_2 layers are computed using a tight-binding model [106] considering only the single nearest neighbor interactions and including spin-orbit coupling [106, 107]. The electrostatic potential and band alignment of each WSe_2 layer is self-consistently computed using the following set of charge-balance equations:

$$C_{\mathrm{IL}}\left(\frac{\phi_{\mathrm{B}}}{e}-\frac{\phi_{\mathrm{T}}}{e}\right)-C_{\mathrm{T}}\left(V_{\mathrm{TG}}+\frac{\phi_{\mathrm{T}}}{e}\right)=Q_{\mathrm{T}}(\epsilon_{\mathrm{T}},\mu_{\mathrm{T}},\phi_{\mathrm{T}}) \tag{5.1}$$

$$C_{\mathrm{IL}}\left(\frac{\phi_{\mathrm{T}}}{e}-\frac{\phi_{\mathrm{B}}}{e}\right)-C_{\mathrm{B}}\left(V_{\mathrm{BG}}+\frac{\phi_{\mathrm{B}}}{e}\right)=Q_{\mathrm{B}}(\epsilon_{\mathrm{B}},\mu_{\mathrm{B}},\phi_{\mathrm{B}}) \tag{5.2}$$

where C_{IL} is the interlayer capacitance per unit area, C_{T} (C_{B}) is the top-(bottom-) gate capacitance per unit area, μ_{T} (μ_{B}) is the chemical potential, ϕ_T (ϕ_B) is the electrostatic potential and Q_{T} (Q_{B}) is the excess charge density of the top (bottom) WSe_2 layer, and e is the electron charge. At zero gate biases and zero interlayer voltage, the chemical potentials of both the top and bottom layers are assumed to align with the WSe_2 monolayer mid-gap. The excess charge densities Q_{T} and Q_{B} are given by

$$Q_{T/B}=-e\sum_{\mathbf{k},\sigma}\left(f\left(\epsilon_{\mathrm{T/B}}(\mathbf{k},\sigma)+\phi_{T/B}-\mu_{T/B}\right)-f(E)\right) \tag{5.3}$$

where $f(E)$ is the Fermi distribution function. The single particle coherent tunneling current (I_{coh}) between the two WSe_2 layers is given by

$$I_{\mathrm{coh}}=-e\int_{-\infty}^{\infty}T(E)\big(f(E-\mu_{\mathrm{T}})-f(E-\mu_{\mathrm{B}})\big)dE \tag{5.4}$$

where $T(E)$ is the vertical transmission rate of an electron at energy E is given by

$$T(E)=\frac{2\pi}{\hbar}\sum_{\mathbf{k}_T\mathbf{k}_B\sigma_T\sigma_B}\left|t_{\mathbf{k}_T\mathbf{k}_B\sigma_{\mathrm{T}}\sigma_B}\right|^2A_{\mathrm{TL}}(\mathbf{k}_T,\sigma_{\mathrm{T}},E)A_{\mathrm{BL}}(\mathbf{k}_B,\sigma_{\mathrm{B}},E) \tag{5.5}$$

A_{TL} (A_{BL}) is the spectral density function of the energy states of the top (bottom) WSe_2 layer. The spectral densities are taken to be Lorentzian in form, i.e.

$$A(\mathbf{k}, \sigma, E) = \frac{1}{\pi} \frac{\Gamma}{\left(E - \epsilon(\mathbf{k},\sigma)\right)^2 + \Gamma^2} \tag{5.6}$$

where Γ represents the energy broadening of the quasi-particle states. We note that Γ may also contain contributions from the spatial variation in the electrostatic potential difference between layers due to disorder. For simplicity, the interlayer coupling $t_{\mathbf{k}_T \mathbf{k}_B \sigma_{\mathrm{T}} \sigma_B}$ is assumed to be $t_{\mathbf{k}_T \mathbf{k}_B \sigma_{\mathrm{T}} \sigma_B} = |t|\, \delta_{\mathbf{k}_T \mathbf{k}_B} \delta_{\sigma_T \sigma_B}$ to model the momentum and spin conserving tunneling and $t_{\mathbf{k}_T \mathbf{k}_B \sigma_{\mathrm{T}} \sigma_B} = |t|\, \delta_{\mathbf{k}_T \mathbf{k}_B}$ to model the momentum conserving but spin randomizing tunneling. The summation is performed over all momentum states in the BZ and over the first two valence sub-bands with opposite spins.

A separate, incoherent tunneling current component, where both momentum and spin are randomized is modeled as:

$$I_{\mathrm{rand}} = -eW \int_{-\infty}^{\infty} g_{\mathrm{T}}(E) g_{\mathrm{B}}(E) \big(f(E - \mu_{\mathrm{T}}) - f(E - \mu_{\mathrm{B}})\big) dE \tag{5.7}$$

where the W parameter describes the momentum randomizing strength, $g_{\mathrm{T}}(E)$ ($g_{\mathrm{B}}(E)$) is the TDOS of the top (bottom) layer at energy E. The total tunneling current, $I_{\mathrm{il}} = I_{\mathrm{coh}} + I_{\mathrm{rand}}$. The free parameters in the model are the interlayer coupling (t), the energy broadening parameter (Γ), and the strength of the randomizing potential (W).

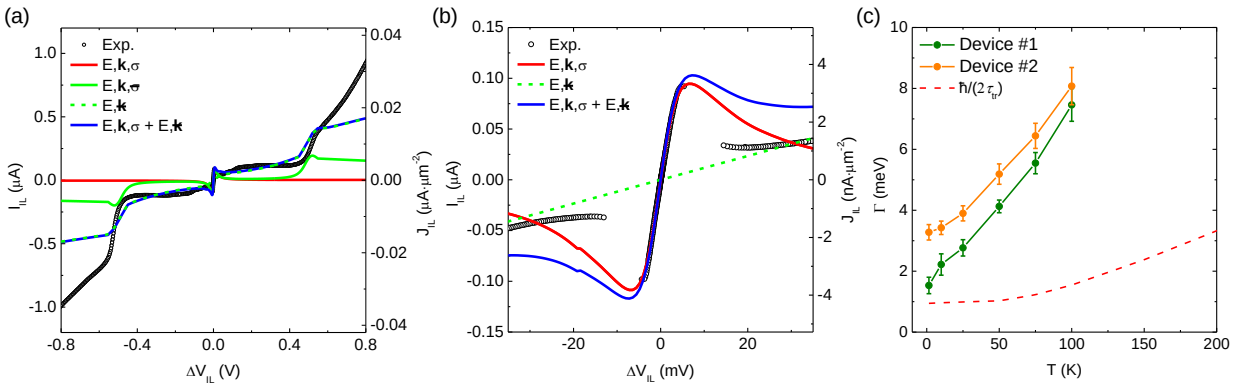

Figure 5.13 (a) I_{IL} vs ΔV_{IL} at $p = 5.6\times10^{12}$ cm^{-2} and $T = 1.5$ K (circles), and calculations under different combinations of energy conserving (E), momentum conserving (**k**) or randomizing (**k̄**), and spin conserving (σ) or randomizing (σ̄) tunneling processes contributing to I_{IL}. (b) Close-up view of panel (a) near $\Delta V_{IL} = 0$. (c) Γ vs T for Device #1 and Device #2 extracted from fits to the experimental I_{IL} vs ΔV_{IL} data (symbols), and from monolayer WSe_2 mobility (dashed line) corresponding to the transport lifetime. The right axes of panels (a, b) show I_{IL} normalized to the TL and BL WSe_2 overlap area.

Figure 5.13(a) shows a comparison of I_{IL} vs ΔV_{IL} calculated from theory and the experimental data of figure 5.9(b) at $p = 5.6\times10^{12}$ cm^{-2} and $T = 1.5$ K, and figure 5.13(b) shows a close-up of figure 5.13(a) data around $\Delta V_{IL} = 0$. To assess the contributions of the different tunneling mechanisms to the total experimentally measured I_{IL}, the current is calculated by successively relaxing the constraints on energy, momentum, and spin conservation. First, we consider the scenario when tunneling is assumed to occur only when all of the energy (E), momentum (**k**), and spin (σ) conservation are satisfied (labeled E, **k**, σ). The calculated I_{IL} vs ΔV_{IL} under these conditions are able to reproduce the experimental primary resonance NDR accurately. However, away from $\Delta V_{IL} = 0$, the experimental data diverge from calculations, which predict no tunneling current away from the primary resonance. This is in an agreement with our assumptions, since the secondary resonances

at $\Delta V_{IL} \sim \pm 0.5$ V require unlike-spin-band tunneling, which is suppressed if the spin is conserved in tunneling.

Given the presence of prominent secondary resonances in our experimental data, it is instructive to relax the spin conservation constraints in our calculations, and consider only the requirement of energy and momentum conservation (labeled E, $\mathbf{k}$, $\not{\sigma}$). In this case, the calculated tunneling current reproduces the NDR at $\Delta V_{IL} = 0$, and additionally shows NDR features at $\Delta V_{IL} \sim \pm 0.5$ V. This behavior, predicted by the model, is similar to observations in double bilayer graphene separated by hBN [10, 54] where the secondary resonance appears due to tunneling between the higher and lower sub-bands of bilayer graphene, in the absence of the requirement for spin conservation. We note that the model predicted current fall off with respect to interlayer voltage at the secondary NDR regions is weaker. Around the secondary resonance peak, the applied bias depletes one of the WSe_2 layers, thereby giving rise to a near zero quantum capacitance in one of the layers. When one of the layers is depleted, the relative alignments of the bandstructures of the two WSe_2 layers remains almost constant even as the applied bias is varied. This giving rise to a weak dependence of the interlayer current on the bias voltage and thereby a weak secondary NDR. The measurement data does not show NDR around $\Delta V_{IL} \sim \pm 0.5$ V. Therefore, we conclude that spin relaxing momentum conserving tunneling is not a dominant form of tunneling that causes the secondary conductance peaks.

Next, we consider the case when both momentum and spin conservation requirements are relaxed and the tunneling current is proportional to the product of TDOS in both the WSe_2 layers (labeled E, $\not{\mathbf{k}}$, $\not{\sigma}$). In this scenario, the calculated current does not

show the primary resonance, but reproduces the experimental data at high $|\Delta V_{IL}|$ reasonably well. Therefore, the interlayer current at high $|\Delta V_{IL}|$ can be attributed predominantly to the momentum relaxing tunneling mechanisms. Further, the current saturates with a weak increase after a particular ΔV_{IL}. This is, again, because one of the WSe_2 layers is depleted.

Finally, we consider a scenario where both momentum and spin conserving as well as momentum and spin relaxing tunneling processes are present (labeled $E,\mathbf{k},\sigma + E,\not{\mathbf{k}},\not{\sigma}$). The calculated tunneling current in this case reproduces both the primary and secondary resonance features of our experimental data, suggesting that both these mechanisms are at play in our samples. Figure 5.13(c) shows the value of Γ used to fit the experimental data of both Devices #1 and #2 as a function of temperature.

5.3.4 In-plane B-filed induced interlayer tunneling current voltage characteristics

In light of the role of several tunneling mechanisms in our samples, one question is whether the primary resonance at $\Delta V_{IL} = 0$ V is indeed due to momentum conserving tunneling. To answer this question, we perform measurements in the presence of an in-plane magnetic field ($B_{||}$), perpendicular to the direction of tunneling current.

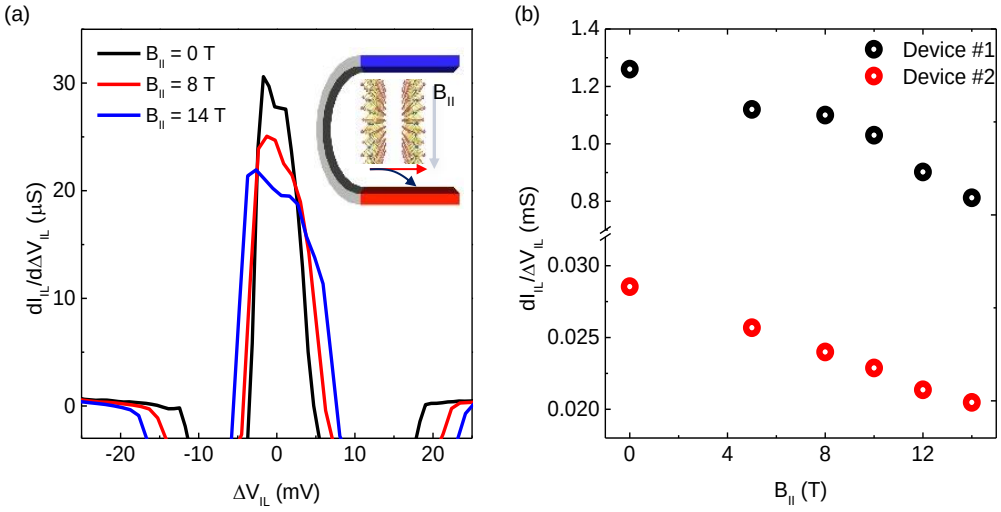

Figure 5.14 (a) $dI_{IL}/d\Delta V_{IL}$ vs ΔV_{IL} for Device #2 at $T = 1.5$ K near $\Delta V_{IL} = 0$ measured at $B_{||} = 0$, 8, and 14 T. Inset: schematic of the sample orientation with respect to $B_{||}$. (b) $dI_{IL}/d\Delta V_{IL}$ vs $B_{||}$ for Device #1 and Device #2.

Figure 5.14(a) shows $dI_{IL}/d\Delta V_{IL}$ vs ΔV_{IL} near the primary resonance for Device#2 at various magnetic field values, which shows the resonance peak conductance decreasing and the peak width increasing with increasing magnetic field. The effect of $B_{||}$ is to produce a momentum shift of the tunneling carriers due to the Lorentz force, which thereby causes a momentum mismatch, and consequently a suppression of the resonance peak. Figure 5.14(b) shows $dI_{IL}/d\Delta V_{IL}$ vs $B_{||}$ for both Devices #1 and #2, where $dI_{IL}/d\Delta V_{IL}$ decreases with $B_{||}$. This observation confirms that momentum conserving tunneling is responsible for the primary resonance at $\Delta V_{IL} = 0$.

5.4 Realization of 180° rotationally aligned WSe_2-hBN-WSe_2 van der Waals heterostructures

To further test the role of spin conservation in tunneling, we now turn our focus to interlayer tunneling in the case of a 180º twist between the two WSe_2 layers. The basic

understanding of energy band diagram is described in figure 5.8 (e-f). Figure 5.8(e) shows a schematic of the valence bands in the two WSe_2 layers at 180º twist and Figures 5.8(f-h) show the band alignments under application of $\Delta V_{IL} = 0, \pm 2\lambda$. In contrast to the figures 5.8(a-d), here the *K* and *K'* valleys in both layers are aligned in momentum space at $\Delta V_{IL} = \pm 0.5$ V, and the unlike spin bands in the opposite layers are aligned at $\Delta V_{IL} = 0$.

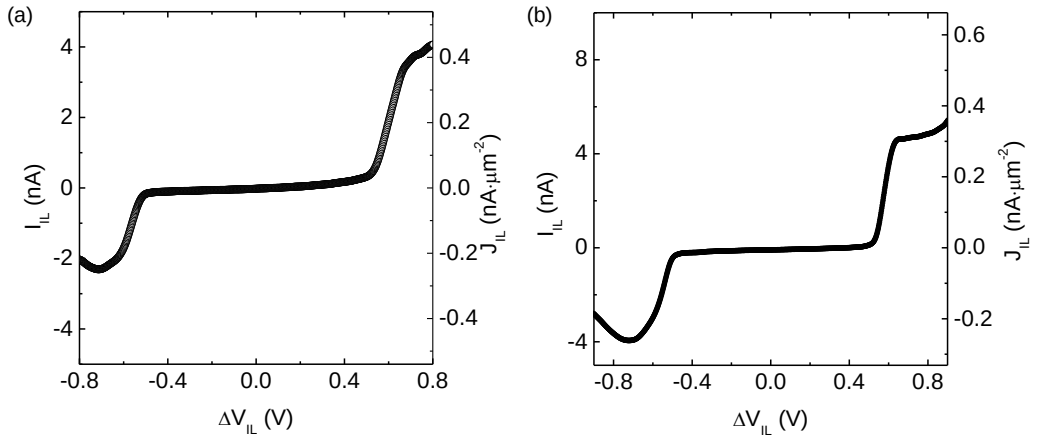

Figure 5.15 (a, b) are I_{IL} vs ΔV_{IL} for Device #5 and #6 at $T = 1.5$ K, respectively from Table 5.2. The right axes are I_{IL} normalized to the TL and BL WSe_2 overlap area.

Figure 5.15(a, b) show I_{IL} vs ΔV_{IL} for Device #5 and #6 with 180º twist between the WSe_2 layers, and seven and five atomic layers of IL hBN. In Device #5, $V_{TG} = -9$ V and $V_{BG} = -9.5$ V are applied with T hBN and B hBN thicknesses of 23.8 nm and 29.7 nm, in which approximate densities using $ep = C \times V$ are $p = 6.3\times10^{12}$ cm^{-2} and $p = 5.3\times10^{12}$ cm^{-2}, respectively. For Device #6, top and bottom layer densities are $p = 9.2\times10^{12}$ cm^{-2} and $p = 4.8\times10^{12}$ cm^{-2}. We note here that inducing carriers at the bottom layer WSe_2 was limited by B hBN leakage problem. As a result, in both samples, the data show negligible

conductance near $\Delta V_{IL} = 0$, i.e. no primary resonance and substantial I_{IL} for $|\Delta V_{IL}| > 0.4$ V, i.e. prominent secondary resonances, along with an NDR at $\Delta V_{IL} = -0.5$ V.

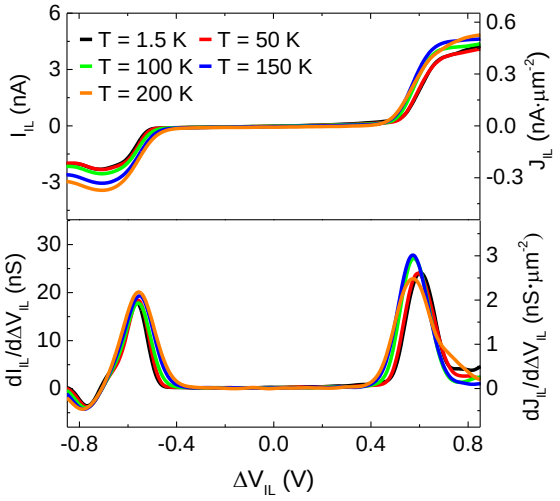

Figure 5.16 I_{IL} vs ΔV_{IL} (top panel) and $dI_{IL}/d\Delta V_{IL}$ vs ΔV_{IL} (bottom panel) for Device #5 as a function of varying temperature from $T = 1.5$ to 200 K. The right axes of panels show I_{IL} and $dI_{IL}/d\Delta V_{IL}$ normalized to the TL and BL WSe_2 overlap area.

In similar to 0º twist samples, to investigate the origin of the tunneling resonances, we perform temperature dependent measurements. Figure 5.16 show I_{IL} vs ΔV_{IL} and corresponding $dI_{IL}/d\Delta V_{IL}$ vs ΔV_{IL} data as a function of varying temperatures from 1.5 K to 200 K. We observe here secondary resonance is quite insensitive to the temperature changes.

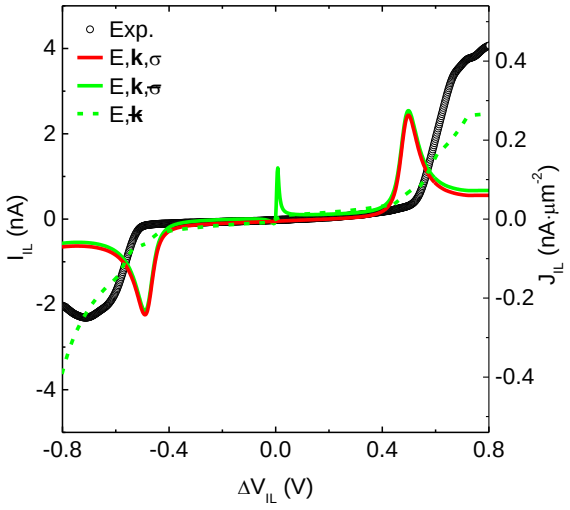

Figure 5.17 I_{IL} vs ΔV_{IL} of figure 5.14(a) data at T = 1.5 K (circles), and calculations under different combinations of tunneling mechanisms. The right axis shows I_{IL} normalized to the TL and BL WSe_2 overlap area.

Figure 5.17 shows a comparison of the experimental and calculated tunneling currents under the same set of constraints employed in the 0º twist case. In the case of energy, momentum, and spin conserving tunneling (E, **k**, σ), the calculated tunneling current shows prominent NDR characteristics at ΔV_{IL} = ±0.5 V, and zero current near ΔV_{IL} = 0. The tunneling current near ΔV_{IL} = 0 is strongly suppressed due to spin mismatch between the opposite layer bands, despite alignment in the momentum space. In the case when only energy and momentum conservation are enforced (E, **k**, σ̸), the calculated current shows a primary resonance at ΔV_{IL} =0 V, at variance with experimental data. Finally, in the case when both spin and momentum conservation are relaxed (E, **k̸**, σ̸), the calculation is able to reproduce the experimental features at high ΔV_{IL}. Comparing the calculations with experimental data, the absence of a primary resonance implies both spin

and momentum are conserved near $\Delta V_{IL} = 0$, but at high ΔV_{IL} momentum randomizing tunneling starts to contribute to I_{IL}.

5.5 SUMMARY

we demonstrate experimentally, and explain theoretically, the role of spin-valley conservation in addition to energy and momentum conservation in vertical transport in twist controlled WSe_2-hBN-WSe_2 heterostructures. Devices with 0^o twist between the two WSe_2 monolayers show a sharp resonance near zero interlayer bias and apparent secondary resonances near ±0.5 V stemming from unlike-spin-band tunneling. Devices with 180^o twist do not show a primary resonance, but show prominent secondary resonances, thanks to alignment of like-spin-bands of the two layers at an interlayer bias of ±0.5 V.

Appendix: List of publications

1. Stefano Larentis, Hema CP Movva, Babak Fallahazad, Kyounghwan Kim, Armand Behroozi, Takashi Taniguchi, Kenji Watanabe, Sanjay K Banerjee, and Emanuel Tutuc, "Large effective mass and interaction-enhanced Zeeman splitting of K-valley electrons in $MoSe_2$," *Physical Review B*, 97, 2018

2. G William Burg, Nitin Prasad, Kyounghwan Kim, Takashi Taniguchi, Kenji Watanabe, Allan H MacDonald, Leonard F Register, and Emanuel Tutuc, "Strongly Enhanced Tunneling at Total Charge Neutrality in Double-Bilayer Graphene-WSe_2 Heterostructures," *Physical Review Letter,* 120, 2018

3. Hema CP Movva, Timothy Lovorn, Babak Fallahazad, Stefano Larentis, Kyounghwan Kim, Takashi Taniguchi, Kenji Watanabe, Sanjay K Banerjee, Allan H MacDonald, and Emanuel Tutuc, "Tunable Γ− K Valley Populations in Hole-Doped Trilayer WSe_2," *Physical Review Letters*, 120, 2017

4. Sangwoo Kang, Xuehao Mou, Babak Fallahazad, Nitin Prasad, Xian Wu, Amithraj Valsaraj, Hema CP Movva, Kyounghwan Kim, Emanuel Tutuc, Leonard F. Register, and Sanjay K Banerjee, "Interlayer tunnel field-effect transistor (ITFET): physics, fabrication and applications." *Journal of Physics D: Applied Physics*, 50, 2017

5. Feng Wen, David C Dillen, Kyounghwan Kim, and Emanuel Tutuc, "Shell morphology and Raman spectra of epitaxial Ge−Si_xGe_{1-x} and Si− Si_xGe_{1-x} core-shell nanowires", *Journal of Applied Physics*, 121, 2017

6. Hema CP Movva, Babak Fallahazad, Kyounghwan Kim, Stefano Larentis, Takashi Taniguchi, Kenji Watanabe, Sanjay K Banerjee, and Emanuel Tutuc, "Density-Dependent Quantum Hall States and Zeeman Splitting in Monolayer and Bilayer WSe2," *Physical Review Letter,* 118, 2017

7. G William Burg, Nitin Prasad, Babak Fallahazad, Amithraj Valsaraj, Kyounghwan Kim, Takashi Taniguchi, Kenji Watanabe, Qingxiao Wang, Moon J Kim, Leonard F Register, and Emanuel Tutuc, "Coherent interlayer tunneling and negative differential resistance with high current density in double bilayer graphene–WSe_2 heterostructures," *Nano Lett,* 17, 3919-3925, 2017

8. Stefano Larentis, Babak Fallahazad, Hema CP Movva, Kyounghwan Kim, Amritesh Rai, Takashi Taniguchi, Kenji Watanabe, Sanjay K Banerjee, and Emanuel Tutuc, "Reconfigurable Complementary Monolayer $MoTe_2$ Field-Effect Transistors for Integrated Circuits," *ACS Nano*, 11, 4832-4839, 2017

9. Kyounghwan Kim, Ashley DaSilva, Shengqiang Huang, Babak Fallahazad, Stefano Larentis, Takashi Taniguchi, Kenji Watanabe, Brian J LeRoy, Allan H MacDonald, and Emanuel Tutuc, "Tunable moiré bands and strong correlations in small-twist-angle bilayer graphene," *Proceedings of the National Academy of Sciences*, 114, 3364-3369, 2017

10. Sangwoo Kang, Nitin Prasad, Hema CP Movva, Amritesh Rai, Kyounghwan Kim, Xuehao Mou, Takashi Taniguchi, Kenji Watanabe, Leonard F Register, Emanuel Tutuc, Sanjay K Banerjee, "Effects of Electrode Layer Band Structure on the Performance of Multilayer Graphene–hBN–Graphene Interlayer Tunnel Field Effect Transistors," *Nano Letters*, 16, 4975 - 4981, 2016

11. Anupam Roy, Hema CP Movva, Biswarup Satpati, Kyounghwan Kim, Rik Dey, Amritesh Rai, Tanmoy Pramanik, Samaresh Guchhait, Emanuel Tutuc, Sanjay K Banerjee, "Structural and Electrical Properties of MoTe2 and MoSe2 Grown by Molecular Beam Epitaxy," *ACS applied Material & interfaces 8*, 7396-7402, 2016

12. Babak Fallahazad, Hema CP Movva, Kyounghwan Kim, Stefano Larentis, Takashi Taniguchi, Kenji Watanabe, Sanjay K Banerjee, and Emanuel Tutuc, "Shubnikov–de Haas Oscillations of High-Mobility Holes in Monolayer and Bilayer WSe_2: Landau Level Degeneracy, Effective Mass, and Negative Compressibility," *Physical Review Letters*, 116, 086601, 2016

13. Kyounghwan Kim, Matthew Yankowitz, Babak Fallahazad, Sangwoo Kang, Hema C. P. Movva, Shengqiang Huang, Stefano Larentis, Chris M. Corbet, Takashi Taniguchi, Kenji Watanabe, Sanjay K. Banerjee, Brian J. LeRoy, and Emanuel Tutuc, "van dew Waals Heterostructures with High Accuracy Rotational Alignment," *Nano Letters*, 16, 1989-1995, 2015

14. David C. Dillen, Feng Wen, Kyounghwan Kim, and Emanuel Tutuc, "Coherently Strained Si–Si_x Ge_{1-x} Core–Shell Nanowire Heterostructures" *Nano Letters*, 16, 392-398, 2015

15. Hema C.P. Movva, Amritesh Rai, Sangwoo Kang, Kyounghwan Kim, Babak Fallahazad, Takashi Taniguchi, Kenji Watanabe, Emanuel Tutuc, and Sanjay K Banerjee, "High-Mobility Holes in Dual-Gated WSe_2 Field-Effect Transistors," *ACS nano 9*, 10402-10410, 2015

16. Sangwoo Kang, Babak Fallahazad, Kayoung Lee, Hema Movva, Kyounghwan Kim, Chris M Corbet, Takashi Taniguchi, Kenji Watanabe, Luigi Colombo, Leonard F Register, Emanuel Tutuc, and Sanjay K Banerjee, "Bilayer Graphene-Hexagonal Boron Nitride Heterostructure Negative Differential Resistance Interlayer Tunnel FET," *IEEE Electron Device Letters,* 36, 405-407, 2015

17. Kyounghwan Kim, Stefano Larentis, Babak Fallahazad, Kayoung Lee, Jiamin Xue, David C Dillen, Chris M Corbet, and Emanuel Tutuc, "Band Alignment in WSe_2–Graphene Heterostructures," *ACS nano*, 9, 4527-4532, 2015.

18. Matthew Yankowitz, Stefano Larentis, Kyounghwan Kim, Jiamin Xue, Devin McKenzie, Shengqiang Huang, Marina Paggen, Mazhar N Ali, Robert J Cava, Emanuel Tutuc, and Brian J LeRoy, "Intrinsic disorder in graphene on transition metal dichalcogenide heterostructures," *Nano Letters*, 15, 1925-1929, 2015

19. Babak Fallahazad, Kayoung Lee, Sangwoo Kang, Jiamin Xue, Stefano Larentis, Christopher Corbet, Kyounghwan Kim, Hema CP Movva, Takashi Taniguchi, Kenji Watanabe, Leonard F Register, Sanjay K Banerjee, Emanuel Tutuc, "Gate-Tunable Resonant Tunneling in Double Bilayer Graphene Heterostructures," *Nano Letters*, 15, 428-433, 2014

20. Chris M Corbet, Connor McClellan, Kyounghwan Kim, Sushant Sonde, Emanuel Tutuc, Sanjay K Banerjee, "Oxidized Titanium as a Gate Dielectric for Graphene Field Effect Transistors and Its Tunneling Mechanisms," *ACS nano*, 8, 10480-10485, 2014

21. Kayoung Lee, Babak Fallahazad, Jiamin Xue, David C Dillen, Kyounghwan Kim, Takashi Taniguchi, Kenji Watanabe, Emanuel Tutuc, "Chemical potential and quantum Hall ferromagnetism in bilayer graphene," *Science*, 345, 58-61, 2014

22. Stefano Larentis, John R Tolsma, Babak Fallahazad, David C Dillen, Kyounghwan Kim, Allan H MacDonald, Emanuel Tutuc, "Band offset and negative compressibility in graphene-MoS_2 heterostructures," *Nano Letters*, 14, 2039-2045, 2014

23. David C Dillen, Kyounghwan Kim, En-Shao Liu, and Emanuel Tutuc, "Radial modulation doping in core-shell nanowires" *Nature Nanotechnology*, 9, 116-120, 2014

24. En-Shao Liu, David C Dillen, Junghyo Nah, Babak Fallahazad, Kyounghwan Kim, and Emanuel Tutuc, "Realization and Scaling of Core-Shell Nanowire-FETs," *IEEE Transactions on Electron Devices,* 60, 4027-4033, 2013

References

[1] A. K. Geim and I. V. Grigorieva, "Van der Waals heterostructures," *Nature,* vol. 499, p. 419, 2013.

[2] S. Mohan, P. Mazumder, G. I. Haddad, R. K. Mains, and J. P. Sun, "Logic design based on negative differential resistance characteristics of quantum electronic devices," *IEE Proceedings G - Circuits, Devices and Systems,* vol. 140, pp. 383-391, 1993.

[3] J. A. Simmons, M. A. Blount, J. S. Moon, W. E. Baca, J. L. Reno, and M. J. Hafich, "Unipolar complementary bistable memories using gate-controlled negative differential resistance in a 2D-2D quantum tunneling transistor," in *International Electron Devices Meeting. IEDM Technical Digest*, 1997, pp. 755-758.

[4] S. K. Banerjee, L. F. Register, E. Tutuc, D. Reddy, and A. H. MacDonald, "Bilayer PseudoSpin Field-Effect Transistor (BiSFET): A Proposed New Logic Device," *IEEE Electron Device Letters,* vol. 30, pp. 158-160, 2009.

[5] P. Zhao, R. M. Feenstra, G. Gu, and D. Jena, "SymFET: A Proposed Symmetric Graphene Tunneling Field-Effect Transistor," *IEEE Transactions on Electron Devices,* vol. 60, pp. 951-957, 2013.

[6] C. Lee, I. Meric, S. Sorgenfrei, K. L. Shepard, C. R. Dean, A. F. Young*, et al.*, "Boron nitride substrates for high-quality graphene electronics," *Nature Nanotechnology,* vol. 5, pp. 722-726, 2010.

[7] L. Wang, I. Meric, P. Y. Huang, Q. Gao, Y. Gao, H. Tran*, et al.*, "One-Dimensional Electrical Contact to a Two-Dimensional Material," *Science,* vol. 342, pp. 614-617, 2013.

[8] A. Mishchenko, J. S. Tu, Y. Cao, R. V. Gorbachev, J. R. Wallbank, M. T. Greenaway*, et al.*, "Twist-controlled resonant tunnelling in graphene/boron nitride/graphene heterostructures," *Nature Nanotechnology,* vol. 9, pp. 808-813, 2014.

[9] B. Fallahazad, K. Lee, S. Kang, J. Xue, S. Larentis, C. Corbet*, et al.*, "Gate-tunable resonant tunneling in double bilayer graphene heterostructures," *Nano letters* vol. 15, p. 428, 2015.

[10] S. Kang, B. Fallahazad, K. Lee, H. Movva, K. Kim, C. M. Corbet*, et al.*, "Bilayer Graphene-Hexagonal Boron Nitride Heterostructure Negative Differential

Resistance Interlayer Tunnel FET," *Ieee Electron Device Letters,* vol. 36, pp. 405-407, 2015.

[11] G. W. Burg, N. Prasad, B. Fallahazad, A. Valsaraj, K. Kim, T. Taniguchi*, et al.*, "Coherent Interlayer Tunneling and Negative Differential Resistance with High Current Density in Double Bilayer Graphene-WSe2 Heterostructures," *Nano Letters,* vol. 17, pp. 3919-3925, 2017.

[12] C. R. Dean, L. Wang, P. Maher, C. Forsythe, F. Ghahari, Y. Gao*, et al.*, "Hofstadter's butterfly and the fractal quantum Hall effect in moire superlattices," *Nature,* vol. 497, pp. 598-602, 2013.

[13] L. A. Ponomarenko, R. V. Gorbachev, G. L. Yu, D. C. Elias, R. Jalil, A. A. Patel*, et al.*, "Cloning of Dirac fermions in graphene superlattices," *Nature,* vol. 497, pp. 594-597, 2013.

[14] B. Hunt, J. D. Sanchez-Yamagishi, A. F. Young, M. Yankowitz, B. J. LeRoy, K. Watanabe*, et al.*, "Massive Dirac Fermions and Hofstadter Butterfly in a van der Waals Heterostructure," *Science,* vol. 340, pp. 1427-1430, 2013.

[15] K. Kim, A. DaSilva, S. Huang, B. Fallahazad, S. Larentis, T. Taniguchi*, et al.*, "Tunable moire bands and strong correlations in small-twist-angle bilayer graphene," *Proceedings of the National Academy of Sciences of the United States of America,* vol. 114, pp. 3364-3369, 2017.

[16] Y. Kim, P. Herlinger, P. Moon, M. Koshino, T. Taniguchi, K. Watanabe*, et al.*, "Charge Inversion and Topological Phase Transition at a Twist Angle Induced van Hove Singularity of Bilayer Graphene," *Nano Letters,* vol. 16, pp. 5053-5059, 2016.

[17] Y. Cao, J. Y. Luo, V. Fatemi, S. Fang, J. D. Sanchez-Yamagishi, K. Watanabe*, et al.*, "Superlattice-Induced Insulating States and Valley-Protected Orbits in Twisted Bilayer Graphene," *Physical Review Letters,* vol. 117, 2016.

[18] W. Yan, M. X. Liu, R. F. Dou, L. Meng, L. Feng, Z. D. Chu*, et al.*, "Angle-Dependent van Hove Singularities in a Slightly Twisted Graphene Bilayer," *Physical Review Letters,* vol. 109, 2012.

[19] M. Yankowitz, J. M. Xue, D. Cormode, J. D. Sanchez-Yamagishi, K. Watanabe, T. Taniguchi*, et al.*, "Emergence of superlattice Dirac points in graphene on hexagonal boron nitride," *Nature Physics,* vol. 8, pp. 382-386, 2012.

[20] T. Ohta, A. Bostwick, T. Seyller, K. Horn, and E. Rotenberg, "Controlling the Electronic Structure of Bilayer Graphene," *Science,* vol. 313, pp. 951-954, 2006.

[21] E. McCann and V. I. Fal'ko, "Landau-Level Degeneracy and Quantum Hall Effect in a Graphite Bilayer," *Physical Review Letters,* vol. 96, p. 086805, 2006.

[22] M. Kindermann and E. J. Mele, "Landau quantization in twisted bilayer graphene: The Dirac comb," *Physical Review B,* vol. 84, p. 161406, 2011.

[23] M. I. Katsnelson, K. S. Novoselov, and A. K. Geim, "Chiral tunnelling and the Klein paradox in graphene," *Nature Physics,* vol. 2, pp. 620-625, 2006.

[24] K. Lee, B. Fallahazad, J. M. Xue, D. C. Dillen, K. Kim, T. Taniguchi*, et al.*, "Chemical potential and quantum Hall ferromagnetism in bilayer graphene," *Science,* vol. 345, pp. 58-61, 2014.

[25] J. Nilsson, A. H. Castro Neto, N. M. R. Peres, and F. Guinea, "Electron-electron interactions and the phase diagram of a graphene bilayer," *Physical Review B,* vol. 73, p. 214418, 2006.

[26] G. T. de Laissardiere, D. Mayou, and L. Magaud, "Localization of Dirac Electrons in Rotated Graphene Bilayers," *Nano Letters,* vol. 10, pp. 804-808, 2010.

[27] R. Bistritzer and A. H. MacDonald, "Moire bands in twisted double-layer graphene," *Proceedings of the National Academy of Sciences of the United States of America,* vol. 108, pp. 12233-12237, 2011.

[28] Y. Cao, V. Fatemi, S. Fang, K. Watanabe, T. Taniguchi, E. Kaxiras*, et al.*, "Unconventional superconductivity in magic-angle graphene superlattices," *Nature,* vol. 556, p. 43, 2018.

[29] Y. Cao, V. Fatemi, A. Demir, S. Fang, S. L. Tomarken, J. Y. Luo*, et al.*, "Correlated insulator behaviour at half-filling in magic-angle graphene superlattices," *Nature,* vol. 556, p. 80, 2018.

[30] K. Kim, S. Larentis, B. Fallahazad, K. Lee, J. Xue, D. C. Dillen*, et al.*, "Band Alignment in WSe2–Graphene Heterostructures," *ACS Nano,* vol. 9, pp. 4527-4532, 2015.

[31] W. J. S. L. D. BoerF.Jellinek, "Crystal structures of tungsten disulfide and diselenide," *Journal of Solid State Chemistry,* vol. 70, pp. 207-209, 1987.

[32] Q. H. Wang, K. Kalantar-Zadeh, A. Kis, J. N. Coleman, and M. S. Strano, "Electronics and optoelectronics of two-dimensional transition metal dichalcogenides," *Nature nanotechnology,* vol. 7, p. 699, 2012.

[33] H. Jiang, "Electronic Band Structures of Molybdenum and Tungsten Dichalcogenides by the GW Approach," *The Journal of Physical Chemistry C,* vol. 116, pp. 7664-7671, 2012.

[34] H. Zeng, G.-B. Liu, J. Dai, Y. Yan, B. Zhu, R. He*, et al.*, "Optical signature of symmetry variations and spin-valley coupling in atomically thin tungsten dichalcogenides," *Scientific reports,* vol. 3, p. 1608, 2013.

[35] D. Wickramaratne, F. Zahid, and R. K. Lake, "Electronic and thermoelectric properties of few-layer transition metal dichalcogenides," *The Journal of chemical physics* vol. 140, p. 124710, 2014.

[36] H. L. Zeng, G. B. Liu, J. F. Dai, Y. J. Yan, B. R. Zhu, R. C. He*, et al.*, "Optical signature of symmetry variations and spin-valley coupling in atomically thin tungsten dichalcogenides," *SCIENTIFIC REPORTS,* vol. 3, p. 1608, 2013.

[37] W. Zhao, R. M. Ribeiro, M. Toh, A. Carvalho, C. Kloc, A. H. Castro Neto*, et al.*, "Origin of indirect optical transitions in few-layer MoS2, WS2, and WSe2," *Nano letters* vol. 13, p. 5627, 2013.

[38] V. Podzorov, M. E. Gershenson, C. Kloc, R. Zeis, and E. Bucher, "High-mobility field-effect transistors based on transition metal dichalcogenides," *Applied Physics Letters,* vol. 84, pp. 3301-3303, 2004.

[39] H. Fang, S. Chuang, T. C. Chang, K. Takei, T. Takahashi, and A. Javey, "High-performance single layered WSe_2 p-FETs with chemically doped contacts," *Nano letters* vol. 12, p. 3788, 2012.

[40] W. Liu, J. Kang, D. Sarkar, Y. Khatami, D. Jena, and K. Banerjee, "Role of metal contacts in designing high-performance monolayer n-type WSe2 field effect transistors," *Nano letters* vol. 13, p. 1983, 2013.

[41] G. Prasad and O. N. Srivastava, "The high-efficiency (17.1%) WSe2 photo-electrochemical solar cell," *Journal of Physics D: Applied Physics,* vol. 21, p. 1028, 1988.

[42] A. Pospischil, M. M. Furchi, and T. Mueller, "Solar-energy conversion and light emission in an atomic monolayer p-n diode," *Nature nanotechnology,* vol. 9, pp. 257-261, 2014.

[43] J. S. Ross, P. Klement, A. M. Jones, N. J. Ghimire, J. Yan, D. G. Mandrus, *et al.*, "Electrically tunable excitonic light-emitting diodes based on monolayer WSe2 p–n junctions," *Nature Nanotechnology,* vol. 9, p. 268, 2014.

[44] B. W. H. Baugher, H. O. H. Churchill, Y. Yang, and P. Jarillo-Herrero, "Optoelectronic devices based on electrically tunable p-n diodes in a monolayer dichalcogenide," *Nature nanotechnology,* vol. 9, pp. 262-267, 2014.

[45] Y. J. Zhang, T. Oka, R. Suzuki, J. T. Ye, and Y. Iwasa, "Electrically Switchable Chiral Light-Emitting Transistor," *Science,* vol. 344, pp. 725-728, 2014.

[46] S. Larentis, J. R. Tolsma, B. Fallahazad, D. C. Dillen, K. Kim, A. H. MacDonald, *et al.*, "Band Offset and Negative Compressibility in Graphene-MoS2 Heterostructures," *Nano Letters,* vol. 14, pp. 2039-2045, 2014.

[47] S. L. Matthew Yankowitz, Kyounghwan Kim, Jiamin Xue, Devin McKenzie, Shengqiang Huang, Marina Paggen, Mazhar N. Ali, Robert J. Cava, Emanuel Tutuc, Brian J. LeRoy, "Intrinsic disorder in graphene on transition metal dichalcogenide heterostructures," *arXiv:1411.6597,* 2015.

[48] S. Kim, I. Jo, D. C. Dillen, D. A. Ferrer, B. Fallahazad, Z. Yao, *et al.*, "Direct Measurement of the Fermi Energy in Graphene Using a Double-Layer Heterostructure," *Physical Review Letters,* vol. 108, 2012.

[49] R. S. Yan, Q. Zhang, W. Li, I. Calizo, T. Shen, C. A. Richter, *et al.*, "Determination of graphene work function and graphene-insulator-semiconductor band alignment by internal photoemission spectroscopy," *Applied Physics Letters,* vol. 101, 2012.

[50] Y. J. Yu, Y. Zhao, S. Ryu, L. E. Brus, K. S. Kim, and P. Kim, "Tuning the Graphene Work Function by Electric Field Effect," *Nano Letters,* vol. 9, pp. 3430-3434, 2009.

[51] L. Britnell, R. V. Gorbachev, R. Jalil, B. D. Belle, F. Schedin, A. Mishchenko, *et al.*, "Field-Effect Tunneling Transistor Based on Vertical Graphene Heterostructures," *Science,* vol. 335, pp. 947-950, 2012.

[52] T. Georgiou, R. Jalil, B. D. Belle, L. Britnell, R. V. Gorbachev, S. V. Morozov, *et al.*, "Vertical field-effect transistor based on graphene-WS2 heterostructures for flexible and transparent electronics," *Nature Nanotechnology,* vol. 8, pp. 100-103, 2013.

[53] B. L. Fallahazad, Kayoung; Kang, Sangwoo; Xue, Jiamin; Larentis, Stefano; Corbet, Christopher; Kim, Kyounghwan; Movva, Hema C P; Taniguchi, Takashi;

Watanabe, Kenji; Register, Leonard F; Banerjee, Sanjay K; Tutuc, Emanuel, "Gate-tunable resonant tunneling in double bilayer graphene heterostructures.," *Nano Letters,* vol. 15, pp. 428-33, 2015.

[54] K. Kim, M. Yankowitz, B. Fallahazad, S. Kang, H. C. P. Movva, S. Q. Huang*, et al.*, "van der Waals Heterostructures with High Accuracy Rotational Alignment," *Nano Letters,* vol. 16, pp. 1989-1995, 2016.

[55] Y. M. You, Z. H. Ni, T. Yu, and Z. X. Shen, "Edge chirality determination of graphene by Raman spectroscopy," *Applied Physics Letters,* vol. 93, 2008.

[56] A. C. Ferrari, J. C. Meyer, V. Scardaci, C. Casiraghi, M. Lazzeri, F. Mauri*, et al.*, "Raman spectrum of graphene and graphene layers," *Physical Review Letters,* vol. 97, 2006.

[57] K. Kim, S. Coh, L. Z. Tan, W. Regan, J. M. Yuk, E. Chatterjee*, et al.*, "Raman Spectroscopy Study of Rotated Double-Layer Graphene: Misorientation-Angle Dependence of Electronic Structure," *Physical Review Letters,* vol. 108, 2012.

[58] E. Stolyarova, K. T. Rim, S. M. Ryu, J. Maultzsch, P. Kim, L. E. Brus*, et al.*, "High-resolution scanning tunneling microscopy imaging of mesoscopic graphene sheets on an insulating surface," *Proceedings of the National Academy of Sciences of the United States of America,* vol. 104, pp. 9209-9212, 2007.

[59] Y. B. Zhang, V. W. Brar, F. Wang, C. Girit, Y. Yayon, M. Panlasigui*, et al.*, "Giant phonon-induced conductance in scanning tunnelling spectroscopy of gate-tunable graphene," *Nature Physics,* vol. 4, pp. 627-630, 2008.

[60] A. Deshpande, W. Bao, Z. Zhao, C. N. Lau, and B. J. LeRoy, "Mapping the Dirac point in gated bilayer graphene," *Applied Physics Letters,* vol. 95, 2009.

[61] G. M. Rutter, S. Y. Jung, N. N. Klimov, D. B. Newell, N. B. Zhitenev, and J. A. Stroscio, "Microscopic polarization in bilayer graphene," *Nature Physics,* vol. 7, pp. 649-655, 2011.

[62] M. Yankowitz, J. I. J. Wang, S. C. Li, A. G. Birdwell, Y. A. Chen, K. Watanabe*, et al.*, "Band structure mapping of bilayer graphene via quasiparticle scattering," *Apl Materials,* vol. 2, 2014.

[63] K. Zou and J. Zhu, "Transport in gapped bilayer graphene: The role of potential fluctuations," *Physical Review B,* vol. 82, 2010.

[64] T. Taychatanapat and P. Jarillo-Herrero, "Electronic Transport in Dual-Gated Bilayer Graphene at Large Displacement Fields," *Physical Review Letters,* vol. 105, 2010.

[65] K. Lee, B. Fallahazad, H. Min, and E. Tutuc, "Transport Gap in Dual-Gated Graphene Bilayers Using Oxides as Dielectrics," *Ieee Transactions on Electron Devices,* vol. 60, pp. 103-108, 2013.

[66] J. M. B. L. dos Santos, N. M. R. Peres, and A. H. Castro, "Graphene bilayer with a twist: Electronic structure," *Physical Review Letters,* vol. 99, 2007.

[67] J. D. Sanchez-Yamagishi, T. Taychatanapat, K. Watanabe, T. Taniguchi, A. Yacoby, and P. Jarillo-Herrero, "Quantum Hall Effect, Screening, and Layer-Polarized Insulating States in Twisted Bilayer Graphene," *Physical Review Letters,* vol. 108, 2012.

[68] A. N. Kolmogorov and V. H. Crespi, "Registry-dependent interlayer potential for graphitic systems," *Physical Review B,* vol. 71, 2005.

[69] B. Fallahazad, K. Lee, S. Kang, J. M. Xue, S. Larentis, C. Corbet*, et al.*, "Gate-Tunable Resonant Tunneling in Double Bilayer Graphene Heterostructures," *Nano Letters,* vol. 15, pp. 428-433, 2015.

[70] L. Britnell, R. V. Gorbachev, R. Jalil, B. D. Belle, F. Schedin, M. I. Katsnelson*, et al.*, "Electron Tunneling through Ultrathin Boron Nitride Crystalline Barriers," *Nano Letters,* vol. 12, pp. 1707-1710, 2012.

[71] E. McCann, D. S. L. Abergel, and V. I. Fal'ko, "Electrons in bilayer graphene," *Solid State Communications,* vol. 143, pp. 110-115, 2007.

[72] Y. F. Hao, M. S. Bharathi, L. Wang, Y. Y. Liu, H. Chen, S. Nie*, et al.*, "The Role of Surface Oxygen in the Growth of Large Single-Crystal Graphene on Copper," *Science,* vol. 342, pp. 720-723, 2013.

[73] K. Kim, A. DaSilva, S. Huang, B. Fallahazad, S. Larentis, T. Taniguchi*, et al.*, "Tunable moiré bands and strong correlations in small-twist-angle bilayer graphene," *Proceedings of the National Academy of Sciences,* vol. 114, pp. 3364-3369, 2017.

[74] J. M. Xue, J. Sanchez-Yamagishi, D. Bulmash, P. Jacquod, A. Deshpande, K. Watanabe*, et al.*, "Scanning tunnelling microscopy and spectroscopy of ultra-flat graphene on hexagonal boron nitride," *Nature Materials,* vol. 10, pp. 282-285, 2011.

[75] E. J. Mele, "Commensuration and interlayer coherence in twisted bilayer graphene," *Physical Review B,* vol. 81, 2010.

[76] S. Shallcross, S. Sharma, E. Kandelaki, and O. A. Pankratov, "Electronic structure of turbostratic graphene," *Physical Review B,* vol. 81, 2010.

[77] J. M. B. L. dos Santos, N. M. R. Peres, and A. H. Castro Neto, "Continuum model of the twisted graphene bilayer," *Physical Review B,* vol. 86, 2012.

[78] T. Ohta, J. T. Robinson, P. J. Feibelman, A. Bostwick, E. Rotenberg, and T. E. Beechem, "Evidence for Interlayer Coupling and Moire Periodic Potentials in Twisted Bilayer Graphene," *Physical Review Letters,* vol. 109, 2012.

[79] I. Brihuega, P. Mallet, H. Gonzalez-Herrero, G. T. de Laissardiere, M. M. Ugeda, L. Magaud*, et al.*, "Unraveling the Intrinsic and Robust Nature of van Hove Singularities in Twisted Bilayer Graphene by Scanning Tunneling Microscopy and Theoretical Analysis (vol 109, 196802, 2012)," *Physical Review Letters,* vol. 109, 2012.

[80] C. R. Woods, L. Britnell, A. Eckmann, R. S. Ma, J. C. Lu, H. M. Guo*, et al.*, "Commensurate-incommensurate transition in graphene on hexagonal boron nitride," *Nature Physics,* vol. 10, pp. 451-456, 2014.

[81] P. Moon and M. Koshino, "Energy spectrum and quantum Hall effect in twisted bilayer graphene," *Physical Review B,* vol. 85, 2012.

[82] Y. B. Zhang, T. T. Tang, C. Girit, Z. Hao, M. C. Martin, A. Zettl*, et al.*, "Direct observation of a widely tunable bandgap in bilayer graphene," *Nature,* vol. 459, pp. 820-823, 2009.

[83] R. T. Weitz, M. T. Allen, B. E. Feldman, J. Martin, and A. Yacoby, "Broken-Symmetry States in Doubly Gated Suspended Bilayer Graphene," *Science,* vol. 330, pp. 812-816, 2010.

[84] P. Maher, L. Wang, Y. D. Gao, C. Forsythe, T. Taniguchi, K. Watanabe*, et al.*, "Tunable fractional quantum Hall phases in bilayer graphene," *Science,* vol. 345, pp. 61-64, 2014.

[85] G. H. Li, A. Luican, J. M. B. L. dos Santos, A. H. Castro Neto, A. Reina, J. Kong*, et al.*, "Observation of Van Hove singularities in twisted graphene layers," *Nature Physics,* vol. 6, pp. 109-113, 2010.

[86] A. Luican, G. H. Li, A. Reina, J. Kong, R. R. Nair, K. S. Novoselov*, et al.*, "Single-Layer Behavior and Its Breakdown in Twisted Graphene Layers," *Physical Review Letters,* vol. 106, 2011.

[87] D. Wong, Y. Wang, J. Jung, S. Pezzini, A. M. DaSilva, H. Z. Tsai*, et al.*, "Local spectroscopy of moire-induced electronic structure in gate-tunable twisted bilayer graphene," *Physical Review B,* vol. 92, 2015.

[88] D. R. Hofstadter, "Energy-Levels and Wave-Functions of Bloch Electrons in Rational and Irrational Magnetic-Fields," *Physical Review B,* vol. 14, pp. 2239-2249, 1976.

[89] F. H. Claro and G. H. Wannier, "Magnetic Subband Structure of Electrons in Hexagonal Lattices," *Physical Review B,* vol. 19, pp. 6068-6074, 1979.

[90] A. H. Macdonald, "Landau-Level Subband Structure of Electrons on a Square Lattice," *Physical Review B,* vol. 28, pp. 6713-6717, 1983.

[91] R. Bistritzer and A. H. MacDonald, "Moire butterflies in twisted bilayer graphene," *Physical Review B,* vol. 84, 2011.

[92] R. V. Gorbachev, J. C. W. Song, G. L. Yu, A. V. Kretinin, F. Withers, Y. Cao*, et al.*, "Detecting topological currents in graphene superlattices," *Science,* vol. 346, pp. 448-451, 2014.

[93] J. P. Eisenstein, D. Syphers, L. N. Pfeiffer, and K. W. West, "Quantum lifetime of two-dimensional holes," *Solid State Communications,* vol. 143, pp. 365-368, 2007.

[94] L. Britnell, R. V. Gorbachev, A. K. Geim, L. A. Ponomarenko, A. Mishchenko, M. T. Greenaway*, et al.*, "Resonant tunnelling and negative differential conductance in graphene transistors," *Nature Communications,* vol. 4, 2013.

[95] P. M. Campbell, A. Tarasov, C. A. Joiner, W. J. Ready, and E. M. Vogel, "Enhanced Resonant Tunneling in Symmetric 2D Semiconductor Vertical Heterostructure Transistors," *ACS Nano,* vol. 9, pp. 5000-5008, 2015.

[96] B. Fallahazad, H. C. P. Movva, K. Kim, S. Larentis, T. Taniguchi, K. Watanabe*, et al.*, "Shubnikov-de Haas Oscillations of High-Mobility Holes in Monolayer and Bilayer WSe2: Landau Level Degeneracy, Effective Mass, and Negative Compressibility," *Physical Review Letters,* vol. 116, 2016.

[97] C. Zhang, Y. Chen, A. Johnson, M.-Y. Li, L.-J. Li, P. C. Mende*, et al.*, "Probing Critical Point Energies of Transition Metal Dichalcogenides: Surprising Indirect Gap of Single Layer WSe2," *Nano letters,* vol. 15, pp. 6494-6500, 2015.

[98] M. Yankowitz, D. McKenzie, and B. J. LeRoy, "Local Spectroscopic Characterization of Spin and Layer Polarization in WSe2," *Physical Review Letters,* vol. 115, 2015.

[99] D. Xiao, G.-B. Liu, W. Feng, X. Xu, and W. Yao, "Coupled spin and valley physics in monolayers of MoS2 and other group-VI dichalcogenides," *Physical review letters* vol. 108, p. 196802, 2012.

[100] Z. Y. Zhu, Y. C. Cheng, and U. Schwingenschlögl, "Giant spin-orbit-induced spin splitting in two-dimensional transition-metal dichalcogenide semiconductors," *Physical Review B,* vol. 84, 2011.

[101] L. Wang, I. Meric, P. Y. Huang, Q. Gao, Y. Gao, H. Tran*, et al.*, "One-dimensional electrical contact to a two-dimensional material," *Science (New York, N.Y.),* vol. 342, pp. 614-617, 2013.

[102] H. C. P. Movva, A. Rai, S. Kang, K. Kim, B. Fallahazad, T. Taniguchi*, et al.*, "High-Mobility Holes in Dual-Gated WSe2 Field-Effect Transistors," *Acs Nano,* vol. 9, pp. 10402-10410, 2015.

[103] S. B. Desai, S. R. Madhvapathy, M. Amani, D. Kiriya, M. Hettick, M. Tosun*, et al.*, "Gold-Mediated Exfoliation of Ultralarge Optoelectronically-Perfect Monolayers," *Advanced Materials,* vol. 28, pp. 4053-4058, 2016.

[104] L. Zheng and A. MacDonald, "Tunneling conductance between parallel two-dimensional electron systems," *Physical Review B,* vol. 47, pp. 10619-10624, 1993.

[105] N. Turner, J. Nicholls, E. Linfield, K. Brown, G. Jones, and D. Ritchie, "Tunneling between parallel two-dimensional electron gases," *Physical Review B,* vol. 54, pp. 10614-10624, 1996.

[106] G.-B. Liu, W.-Y. Shan, Y. Yao, W. Yao, and D. Xiao, "Three-band tight-binding model for monolayers of group-VIB transition metal dichalcogenides," *Physical Review B,* vol. 88, 2013.

[107] D. Le, A. Barinov, E. Preciado, M. Isarraraz, I. Tanabe, T. Komesu*, et al.*, "Spin-orbit coupling in the band structure of monolayer WSe2," *Journal of Physics-Condensed Matter,* vol. 27, 2015.